NATIONAL TECHNICAL UNIVERSITY OF ATHENS
SCHOOL OF ELECTRICAL AND COMPUTER ENGINEERING
DIVISION OF INFORMATION TRANSMISSION
SYSTEMS AND MATERIAL TECHNOLOGY

The Method of Auxiliary Sources in electromagnetic problems of scattering, mode analysis, and shielding: Theory and Applications

Doctoral Thesis

Minas Kouroumplakis

Three-member Advisory Committee:	G. Fikioris, Professor NTUA (Supervisor) N. Tsitsas, Assoc. Professor A.U.Th. (Co-Supervisor) E. Glytsis, Professor,NTUA

Athens, July 2022

ΕΘΝΙΚΟ ΜΕΤΣΟΒΙΟ ΠΟΛΥΤΕΧΝΕΙΟ
ΣΧΟΛΗ ΗΛΕΚΤΡΟΛΟΓΩΝ ΜΗΧΑΝΙΚΩΝ
ΚΑΙ ΜΗΧΑΝΙΚΩΝ ΥΠΟΛΟΓΙΣΤΩΝ
ΤΟΜΕΑΣ ΣΥΣΤΗΜΑΤΩΝ ΜΕΤΑΔΟΣΗΣ ΠΛΗΡΟΦΟΡΙΑΣ
ΚΑΙ ΤΕΧΝΟΛΟΓΙΑΣ ΥΛΙΚΩΝ

Η Μέθοδος Βοηθητικών Πηγών σε ηλεκτρομαγνητικά προβλήματα σκέδασης, ανάλυσης ρυθμών κυματοδήγησης και θωράκισης: Θεωρία και Εφαρμογές

ΔΙΔΑΚΤΟΡΙΚΗ ΔΙΑΤΡΙΒΗ

Μηνάς Κουρουμπλάκης

Τριμελής Συμβουλευτική Επιτροπή:
Γεώργιος Φικώρης, Καθηγητής Ε.Μ.Π. (Επιβλέπων)
Νικόλαος Τσίτσας, Αν. Καθηγητής Α.Π.Θ. (Συνεπιβλέπων)
Ηλίας Γλύτσης, Καθηγητής Ε.Μ.Π.

Αθήνα, Ιουλιος 2022

ΕΘΝΙΚΟ ΜΕΤΣΟΒΙΟ ΠΟΛΥΤΕΧΝΕΙΟ
ΣΧΟΛΗ ΗΛΕΚΤΡΟΛΟΓΩΝ ΜΗΧΑΝΙΚΩΝ
ΚΑΙ ΜΗΧΑΝΙΚΩΝ ΥΠΟΛΟΓΙΣΤΩΝ
ΤΟΜΕΑΣ ΣΥΣΤΗΜΑΤΩΝ ΜΕΤΑΔΟΣΗΣ ΠΛΗΡΟΦΟΡΙΑΣ
ΚΑΙ ΤΕΧΝΟΛΟΓΙΑΣ ΥΛΙΚΩΝ

Η Μέθοδος Βοηθητικών Πηγών σε ηλεκτρομαγνητικά προβλήματα σκέδασης, ανάλυσης ρυθμών κυματοδήγησης και θωράκισης: Θεωρία και Εφαρμογές

ΔΙΔΑΚΤΟΡΙΚΗ ΔΙΑΤΡΙΒΗ

Μηνάς Κουρουμπλάκης

Τριμελής Συμβουλευτική Επιτροπή:
Γεώργιος Φικώρης, Καθηγητής Ε.Μ.Π. (Επιβλέπων)
Νικόλαος Τσίτσας, Αν. Καθηγητής Α.Π.Θ. (Συνεπιβλέπων)
Ηλίας Γλύτσης, Καθηγητής Ε.Μ.Π.

Η επιτροπή εξέτασης:

.....	.....	.....
Γ. Φικιώρης Καθηγητής Ε.Μ.Π.	Νικόλαος Τσίτσας Αν. Καθηγητής Α.Π.Θ.	Ηλίας Γλύτσης Καθηγητής Ε.Μ.Π.
.....	.....	.....
Χ. Καψάλης Καθηγητής Ε.Μ.Π.	Π. Παπακανέλλος Επικ. Καθηγητής Σχ. Ικάρων	Ν. Κανταρτζής Καθηγητής Α.Π.Θ.

.....

Κ. Βαλαγιαννόπουλος
Αν. Καθηγητής Nazarbayev University, Kazakhstan

Αθήνα, 13 Ιουλίου 2022

.....
Μηνάς Κουρουμπλάκης

Περίληψη.

Η συνήθης επιλογή για την αριθμητική επίλυση ολοκληρωτικών εξισώσεων είναι η Μέθοδος των Ροπών. Κατά την εφαρμογή της όμως, και συγκεκριμένα, κατά την συμπλήρωση του πίνακα εμπέδησης, είναι απαραίτητος ο υπολογισμός ιδιόμορφων ολοκληρωμάτων λόγω της ολοκλήρωσης πάνω στην συνοριακή επιφάνεια ή καμπύλη. Αυτό έχει σαν αποτέλεσμα την εξαγωγή μιας προσεγγιστικής λύσης των πεδίων του χώρου η οποία σε ορισμένες περιπτώσεις ενδέχεται να εμφανίσει φαινόμενα αριθμητικών ασταθειών

Για τον παραπάνω αλλά και για άλλους λόγους, έχουν αναπτυχθεί μια ομάδα από μεθόδους γνωστές ως "Γενικευμένες Πολυπολικές Τεχνικές" (ΓΠΤ). Μια από τις μεθόδους των ΓΠΤ είναι η Μέθοδος των Βοηθητικών Πηγών (ΜΒΠ). Γενικά η ΜΒΠ αποτελεί μια ιδιαιτέρως αποτελεσματική μέθοδο για την επίλυση συνοριακών προβλημάτων με κύρια πλεονεκτήματα την απλότητα στην υλοποίηση και την ταχύτατη εξαγωγή αποτελεσμάτων. Από την άλλη όμως, η εφαρμογή της ΜΒΠ χρειάζεται προσοχή ιδιαίτερα σε περιπτώσεις που έχουμε απόκλιση των ρευμάτων των βοηθητικών πηγών (divergence of current amplitudes), την εμφάνιση εσφαλμένων ιδιοτιμών σε προβλήματα ανάλυσης κυματοδηγών, ή και όταν απαιτείται υπολογισμός πεδίων σε περιοχές με υψηλή αγωγιμότητα. Η διατριβή πραγματεύεται την εφαρμογή της ΜΒΠ σε προβλήματα που υφίστανται οι προαναφερθείσες συνθήκες.

Συγκεκριμένα, εφαρμόζουμε τη ΜΒΠ σε προβλήματα Η/Μ σκέδασης από κυλίνδρους τέλειων αγωγών (Perfect Electric Conductor-PEC), με κύριο σκοπό τη μελέτη της επίδρασης της απόκλισης (divergence) του πλάτους των βοηθητικών πηγών στον αριθμητικό υπολογισμό των Η/Μ πεδίων.

Στην συνέχεια εφαρμόζεται η ΜΒΠ για την εύρεση των ιδιοτιμών (eigenvalues) μεταλλικών κυματοδηγων με αυθαίρετη διατομή. Για την αντιμετώπιση του προβλήματος των εσφαλμένων ιδιοτιμών, ακολουθείται μια διαφορετική από την συνηθισμένη προσέγγιση κατά την οποία, ο κυματοδηγός διεγείρεται από κάποια πηγή (excitation source) όπως π.χ. σημειακή πηγή ή επίπεδο κύμα. Έτσι προκύπτει η ΜΒΠ με Πηγή Διέγερσης (ΜΒΠ-ΠΔ). Οι ιδιοτιμές σε αυτή την περίπτωση υπολογίζονται εντοπίζοντας τους κυματάριθμους εκείνους για τους οποίους έχουμε συντονισμό στην διατομή του κυματοδηγού.

Έπειτα επεκτείνουμε την ΜΒΠ-ΠΔ αποδεικνύοντας ότι οι συντονισμοί εντοπίζονται και από την μεγιστοποίηση της απόλυτης τιμής του διανύσματος των βοηθητικών πηγών. Το πλεονέκτημα αυτής της προσέγγισης σε σχέση με την αντίστοιχη της συνάρτησης απόκρισης, είναι η απλότητα του αλγορίθμου, η σαφήνεια της καμπύλης απόκρισης, καθώς και η ταχύτητα εξαγωγής των αποτελεσμάτων. Επιπλέον, παρουσιάζεται και ένας αλγόριθμος με τον οποίο επιτυγχάνεται ταχύτατος υπολογισμός του πίνακα εμπέδησης.

Η ΜΒΠ-ΠΔ εφαρμόζεται και στην περίπτωση των διηλεκτρικών κυματοδηγών. Δεδομένου ότι στους διηλεκτρικούς κυματοδηγούς διαδίδονται γενικά υβριδικοί ρυθμοί, απαιτούνται δύο πηγές διέγερσης ταυτόχρονα, μια ηλεκτρική και μία μαγνητική, ώστε να προκύπτουν ορθά αποτελέσματα. Έτσι προκύπτει η ΜΒΠ με Δύο Πηγές Διέγερσης. Αποδεικνύεται αριθμητικά ότι αν οι πηγές διέγερσης τοποθετούνται εντός μιας περιοχής που περικλείεται από μια βέλτιστη καμπύλη, δεν εμφανίζονται εσφαλμένες ιδιοτιμές στο διάγραμμα απόκρισης.

Τέλος, διερευνάται η αποτελεσματικότητα του μονοστρωματικού γραφενίου ως υλικού κατάλληλου για ηλεκτρομαγνητική θωράκιση. Διερευνώνται αριθμητικά περιπτώσεις κυλινδρικών δομών που έχουν ως θωράκιση γραφένιο το οποίο έχει αποτεθεί σε διοξείδιο του πυριτίου. Δεδομένου ότι η συνήθης ΜΒΠ εμφανίζει δυσκολίες στην εύρεση πεδίων σε υλικά με μεγάλη αγωγιμότητα, προτείνεται τροποποιημένη ΜΒΠ σύμφωνα με την οποία αντικαθίσταται το γραφένιο με μία Συνοριακή Συνθήκη Πίνακα Εμπέδησης. Με αυτό τον τρόπο αποφεύγουμε τον υπολογισμό των πεδίων στο εσωτερικό του γραφενίου.

Λέξεις κλειδιά: Μέθοδος Βοηθητικων Πηγών, Σύγκλιση και Απόκλιση, ρυθμοί κυματοδήγησης, συνάρτηση απόκρισης, Μέτρο του Διανύσματος Βοηθητικών Πηγών, Υβριδικοί ρυθμοί, Γραφένιο, Ηλεκτρομαγνητική θωράκιση, Ηλεκτρομαγνητική Σκέδαση.

Abstract

The most common choice for the numerical solution of integral equations is the Method of Moments (MoM). However, during its implementation, and in particular, when filling the impedance matrix, it is necessary to calculate singular integrals due to the integration on the boundary surface or curve. This sometimes results in an approximate solution of the EM fields in a specified domain, which might be unacceptable.

For the above and other reasons, a group of methods known as *Generalized Multipole Techniques (GMT's)* have been developed over many years. One of the methods of GMT's is the Method of Auxiliary Sources (MAS). In general MAS is a very effective method for solving boundary value problems with the main advantages being the simplicity of implementation, low memory usage, and fast computation of the results. On the other hand, the application of MAS might be problematic in cases where we have divergence of current amplitudes, or might need modification in order to deal with the appearance of spurious solutions in mode analysis, and when field calculation is required in areas with high conductivity, such as shielding materials. The dissertation deals with the application of MAS in geometries in which problems of this nature arise.

Specifically, we apply MAS to EM scattering problems from Perfect Electric Conductor (PEC) cylinders, with the main purpose of studying the effect of divergence of auxiliary current amplitudes on the numerical results for the EM fields.

The MAS is then applied to calculate the eigenvalues of simply and multiply connected PEC waveguides with an arbitrary cross section. To address the problem of spurious eigenvalues, a modified version of standard MAS is applied in which the waveguide is driven by an excitation source such as a point source or a plane wave. This modified method is termed as MAS with an Excitation Source (MAS-ES). The eigenvalues are calculated by detecting the wavenumbers for which the waveguide cross section resonates with the excitation source. Resonance is detected by the values of a properly defined response-function.

Then we extend the MAS-ES by proving that the resonances of the waveguide are also detected by observing the peak values of the Auxiliary Current Vector Norm (ACVN). The advantages of this approach over the response-function approach are the simplicity of the algorithm, the clarity of the response curve, and the computation time. In addition, an algorithm is presented with which a very fast calculation of the impedance matrix is achieved.

Additionally we show that MAS-ES applies in the case of dielectric waveguides. Since dielectric waveguides support hybrid modes, two excitation sources are required simultaneously, an electric and magnetic, in order to obtain correct eigenvalues. This results to what we call MAS with Two Excitation Sources (MAS-TES). It is numerically demonstrated that if the excitation sources are placed inside an optimum curve within the core, no spurious solutions appear in the response curve.

Lastly, the evaluation of monolayer graphene (MLG) as a material suitable for EM shielding in the RF/microwave region is investigated. The high conductivity of graphene at RF frequencies in combination with other properties such as transparency in the optical spectrum, mechanical strength, elasticity, thermal conductivity, etc. make it an ideal material for EM shielding. Numerical experiments on cylindrical configurations shielded by graphene which is deposited on silicon dioxide are performed. Since standard MAS encounters difficulties when computing the fields in highly conductive regions, a modified MAS is proposed according to which graphene is replaced by an Impedance Matrix Boundary Condition (MAS with IMBC). This way, we avoid calculating the fields inside graphene.

Index: Method of Auxiliary Sources, Convergence and Divergence, mode analysis, response function, Auxiliary Current Vector Norm, Hybrid Modes, Graphene, Electromagnetic Shielding, Electromagnetic Scattering.

ΕΥΧΑΡΙΣΤΙΕΣ

Θέλω να εκφράσω την ειλικρινή ευγνωμοσύνη και εκτίμηση στον επιβλέποντα μου, Δρ. Γεώργιο Φικιώρη και τον συνεπιβλέποντα μου, Δρ. Νικόλαο Τσίτσα, για την καθοδήγηση τους, τον χρόνο τους, και την υπομονή τους καθ' όλη την διάρκεια της διδακτορικής διατριβής. Η ζωή με έχει διδάξει ότι σπάνια σου δίνεται η δυνατότητα να συνεργαστείς με ανθρώπους που έχουν τέτοιο επιστημονικό επίπεδο και ήθος. Νιώθω τυχερός που είχα αυτή την ευκαιρία και επιθυμία μου είναι να συνεχίσουμε να συνεργαζόμαστε για πολλά χρόνια ακόμα.

Θα ήθελα να ευχαριστήσω θερμά το τρίτο μέλος της Τριμελούς Επιτροπής, τον Δρ. Ηλία Γλύτση, για την βοήθεια που μου πρόσφερε κατά την παρακολούθηση των μεταπτυχιακών μαθημάτων της ευθύνης του, καθώς και για την ευκαιρία που μου έδωσε να υποστηρίξω, έναντι αμοιβης, το εκπαιδευτικό του εργο.

Τέλος, ένα μεγάλο ευχαριστώ στους γονείς μου για την συνεχή συμπαράσταση, κατανοήση και υποστήριξη τους στην προσπάθεια επίτευξης των στόχων μου.

Στους γονείς μου

Εκτενής Ελληνική Περίληψη

Τα προβλήματα συνοριακών τιμών που αφορούν τη σκέδαση και τη διάδοση ηλεκτρομαγνητικών (Η/Μ) κυμάτων διέπονται από διαφορικές και ολοκληρωτικές εξισώσεις. Η επιλογή της επίλυσης μέσω ολοκληρωτικών ή διαφορικών εξισώσεων σχετίζεται με τα χαρακτηριστικά του κάθε συγκεκριμένου ηλεκτρομαγνητικού προβλήματος. Η επίλυση μπορεί να γίνει αναλυτικά μόνο για απλές γεωμετρίες όπως κυκλικές, ελλειπτικές, σφαιρικές και ελλειψοειδείς. Σε άλλες περιπτώσεις απαιτείται η χρήση αριθμητικών μεθόδων.

Η συνήθης επιλογή για την αριθμητική επίλυση ολοκληρωτικών εξισώσεων είναι η *Μέθοδος των Ροπών* (ΜτΡ). Κατά την εφαρμογή της όμως, και συγκεκριμένα, κατά την συμπλήρωση του πίνακα εμπέδησης, είναι απαραίτητος ο υπολογισμός ιδιόμορφων ολοκληρωμάτων λόγω της ολοκλήρωσης πάνω στην συνοριακή επιφάνεια ή καμπύλη. Αυτό έχει σαν αποτέλεσμα την εξαγωγή μιας προσεγγιστικής λύσης των πεδίων του χώρου η οποία σε ορισμένες περιπτώσεις ενδέχεται να εμφανίσει φαινόμενα αριθμητικών ασταθειών.

Για τον παραπάνω αλλά και για άλλους λόγους, έχει αναπτυχθεί μια ομάδα από μεθόδους γνωστές ως *Γενικευμένες Πολυπολικές Τεχνικές* (ΓΠΤ). Η βασική αρχή των μεθόδων αυτών είναι ότι κατά την εφαρμογή τους ορίζεται ένα ισοδύναμο με το αρχικό πρόβλημα, στο οποίο το ζητούμενο ηλεκτρομαγνητικό πεδίο είναι ίσο με την επαλληλία των πεδίων που εκπέμπονται από ένα σύνολο *διακριτών πηγών* οι οποίες είναι απομακρυσμένες από την συνοριακή καμπύλη ή επιφάνεια. Ως εκ τούτου, κατά την συμπλήρωση του πίνακα εμπέδησης δεν είναι απαραίτητος ο υπολογισμός ιδιόμορφων ολοκληρωμάτων.

Η Μέθοδος των Βοηθητικών Πηγών

Μια από τις μεθόδους των ΓΠΤ είναι η *Μέθοδος των Βοηθητικών Πηγών* (ΜΒΠ). Οι περισσότερες μελέτες αποδίδουν την θεμελίωση της ΜΒΠ στον Kupradze και της ερευνητικής του ομάδας, ενώ άλλες στον Mathon και Johnston. Η ΜΒΠ διακρίνεται από τις άλλες ΓΠΤ στο ότι οι εκφράσεις των πεδίων των διακριτών πηγών είναι συναρτήσεις Green μηδενικής τάξης, δηλαδή δεν υπάρχουν άλλοι πόλοι στη γειτονιά της διακριτής πηγής (εκτός από αυτόν στη θέση ης πηγής). Αυτό σημαίνει ότι οι διακριτές πηγές της ΜΒΠ, οι οποίες ονομάζονται *Βοηθητικές Πηγές* (ΒΠ), έχουν φυσική σημασία και χαρακτηρίζονται από σχετικά απλές μαθηματικές εκφράσεις.

Ο τύπος της πηγής που θα επιλεγεί εξαρτάται από τις διαστάσεις του προβλήματος. Για διδιάστατες γεωμετρίες επιλέγονται συνήθως νημάτια ρευμάτων (current filaments) απείρου μήκους που εκπέμπουν διδιάστατα (2Δ) κυλινδρικά κύματα, οι εκφράσεις των οποίων είναι ανάλογες της συναρτήσης Hankel. Στα τρισδιάστατα προβλήματα (3Δ) χρησιμοποιούνται ευρύτατα ζεύγη στοιχειώδων διπόλων, ηλεκτρικών και μαγντικών, που είναι κάθετα μεταξύ τους. Όσον αφορά την θέση των πηγών, αυτές τοποθετούνται ομοιογενώς πάνω σε επιφάνειες (ή καμπύλες σε 2Δ προβλήματα) οι οποίες ονομάζονται *βοηθητικές επιφάνειες* (ή καμπύλες), το σχήμα των οποίων επιλέγεται να είναι ίδιο με το φυσικό σύνορο του προβλήματος.

Τα ηλεκτρομαγντικά πεδία σε κάθε περιοχή ισούνται με την επαλληλία των πεδίων που εκπέμπονται από τις ΒΠ. Οι άγνωστες ποσότητες είναι οι συντελεστές των συναρτήσεων Green στις πεδιακές εκφράσεις των σημειακών πηγών, και αντιπροσωπεύουν τα μιγαδικά πλάτη των ρευμάτων των νηματίων ή τις διπολικές ροπές των στοιχειωδών διπόλων. Στη συνέχεια εφαρμόζεται η οριακή συνθήκη σε έναν διακριτό αριθμό *Συνοριακών Σημείων* (ΣΣ) πάνω στο

φυσικό σύνορο. Εάν ο αριθμός των ΣΣ ισούται με τον αριθμό των ΒΠ τότε προκύπτει γραμμικό σύστημα με τετραγωνικό πίνακα εμπέδησης Z και τα πλάτη των βοηθητικών ρευμάτων προκύπτουν με την μέθοδο της απαλοιφής Gauss. Εναλλακτικά, τα ΣΣ μπορεί να υπερβάινουν τον αριθμό των ΒΠ οπότε τότε το σύστημα είναι υπερκαθορισμένο και έτσι μπορούν να ληφθούν πιο ακριβή αποτελέσματα μέσω μιας ψευδοαντίστροφης λύσης.

Σύνοψη Κεφαλαίων της Διατριβής

Η διατρίβη αυτή πραγματεύεται την ανάδειξη άγνωστων θεωρητικών πτυχών καθώς και πρακτικές εφαρμογές της Μεθόδου των Βοηθητικών Πηγών (ΜΒΠ) σε προβλήματα σκέδασης, ανάλυσης ρυθμών κυματοδήγησης και θωράκισης.

Κεφάλαιο 1

Το Κεφάλαιο 1 είναι εισαγωγικό και σκοπό έχει να θέσει τα θεμέλια ώστε να μπορεί να γίνει κατανοητό, από οποιονδήποτε που έχει ασχοληθεί με αριθμητική επίλυση ηλεκτρομαγνητικών προβλημάτων, το περιεχόμενο των επόμενων κεφαλάιων.

Τονίζονται τα πλεονεκτήματα που έχει η επίλυση ολοκληρωτικών εξισώσεων έναντι διαφορικών εξισώσεων. Στην συνέχεια, μέσω της μελέτης μιας απλής περίπτωσης σκέδασης, παρουσιάζουμε τις πτυχές της ΜτΡ η οποία αποτελεί την κύρια αριθμητική μέθοδο επίλυσης ολοκληρωτικών εξισώσεων. Αναδεικνύουμε τις αδυναμίες τις ΜτΡ οι οποίες οδήγησαν στην ανάπτυξη των ΓΠΤ. Μία από αυτές τις τεχνικές είναι η ΜΒΠ της οποίας οι πτυχές παρουσιάζονται στα πλαίσια του απλού προβλήματος σκέδασης. Παρουσιάζουμε τα πλεονεκτήματα και τα μειονεκτήματα της ΜΒΠ.

Κεφάλαιο 2

Στο Κεφάλαιο 2 μελετάμε προβλήματα σκέδασης ΤΕ πόλωσης από τέλεια αγώγιμους κυλίνδρους, απείρου μήκούς, με κυκλική και μη κυκλική διατομή. Πηγή του προσπίπτοντος κύματος είναι ένα νημάτιο μαγνητικού ρεύματος απείρου μήκους, παράλληλο με τον κύλινδρο και τοποθετημένο έξω από αυτόν.

Σε πρώτη φάση μελετάμε το κυκλικό πρόβλημα το οποίο λύνεται με αναλυτικές μεθόδους και δίνουμε την λύση για το μαγνητικό πεδίο. Διαπιστώνουμε ότι η λύση αυτή είναι συγκλίνουσα έξω από τον κυλινδρο (όπως είναι αναμενόμενο) αλλά και σε μια περιοχή εντός του κυλίνδρου. Η συγκλίνουσα λύση εντός του κυλίνδρου συνιστά την *αναλυτική συνέχεια* του πεδίου. Η λύση είναι αποκλίνουσα όταν τα σημεία παρατήρησης βρίσκονται εντός μιας *κρίσιμης επιφάνειας* εντός του κυλίνδρου.

Έπειτα ορίζουμε ένα ισοδύναμο με το αρχικό κυκλικό πρόβλημα, θεωρώντας ότι το σκεδαζόμενο πεδίο εκπέμπεται από μια συνεχή κατανομή μαγνητικού ρεύματος που βρίσκεται πάνω σε μια βοηθητική επιφάνεια εντός του κυκλικού κυλίνδρου. Εφαρμόζοντας την οριακή συνθήκη, προκύπτει μια ολοκληρώτική εξίσωση Fredholm $1^{ου}$ τύπου με άγνωστη ποσότητα την συνεχή βοηθητική ρευματική πυκνότητα. Η εξίσωση λύνεται με θεωρία σειρών Fourier και καταλήγουμε σε μια έκφραση για την συνεχή βοηθητική μαγνητική πυκνότητα. Αποδεικνύουμε ότι η λύση αυτή συγκλίνει όταν η βοηθητική επιφάνεια είναι έξω από την κρίσιμη επιφάνεια και συνεπώς το ΜΒΠ σκεδαζόμενο πεδίο εξουδετερώνει το προσπίπτον πεδίο πάνω στην επιφάνεια

του κυλίνδρου. Η λύση αποκλίνει όταν η βοηθητική επιφάνεια βρίσκεται εντός της κρίσιμης επιφάνειας.

Ακολουθεί το διακριτό ΜΒΠ κυκλικό πρόβλημα, όπου η συνεχής ΜΒΠ ρευματική κατανομή, αντικαθίσταται από διακριτές ΒΠ (νημάτια μαγνητικών ρευμάτων απείρου μήκους) τοποθετημένες στη βοηθητική επιφάνεια. Σε αυτή την περίπτωση, το σκεδαζόμενο πεδίο είναι επαλληλία των πεδίων που εκπέμπουν οι ΒΠ. Εφαρμόζοντας την οριακή συνθήκη μηδενισμού του αζιμουθιακού ηλεκτρικού πεδίου στην επιφάνεια του κυλίνδρου σε έναν αριθμό ΣΣ ίσο με τον αριθμό των ΒΠ, προκύπτει ένα τετραγωνικό σύστημα το οποίο λόγω της κυκλικής γεωμετρίας, είναι κυκλοφορικό (circulant). Αυτό λύνεται με τη χρήση Διακριτού Μετασχηματισμού Fourier, με τελικό αποτέλεσμα αναλυτική έκφραση για τα πλάτη των μαγνητικών ρευμάτων των ΒΠ.

Στην συνέχεια, βλέπουμε πως συμπεριφέρεται η λύση των μαγνητικών πλατών, όταν ο αριθός των ΒΠ τείνει στο άπειρο. Αποδεικνύουμε ότι τα ΜΒΠ ρεύματα συγκλίνουν στην συνεχή ΜΒΠ ρευματική κατανομή. Επίσης, εξετάζουμε την συμπεριφορά του διακριτου ΜΒΠ πεδίου όταν ο αριθμός των ΒΠ τείνει στο άπειρο. Διαπιστώνουμε ότι συμπεριφέρεται όπως την ακριβή λύση που προκύπτει αναλυτικά. Το βασικό συμπέρασμα εδώ είναι ότι το ΜΒΠ πεδίο συγκλίνει ακόμα και όταν τα πλάτη των μαγνητικών ΒΠ αποκλίνουν.

Ολοκληρώνοντας το θεωρητικό κομμάτι για το κυκλικό πρόβλημα, δίνουμε μια ασυμπτωτική φόρμουλα που δείχνει τη συμπεριφορά των πλατών των ΒΠ όταν αποκλίνουν. Συγκεκριμένα φαίνεται ότι αποκλίνει μόνο το πραγατικό μέρος των πλατών με την απόκλιση να εκδηλώνεται ως ταλάντωση μεταξύ μεγάλων θετικών και αρνητικών τιμών. Τέλος δείχνουμε την εφαρμογή της μεθόδου σε μη κυκλικά σχήματα.

Η τελευταία ενότητα του Κεφαλαίου 2 είναι αφιερωμένη σε αριθμητικά αποτελέσματα τα οποία αποδεικνύουν πλήρως τα θεωρητικά αποτελέσματα για τον κύκλικό πρόβλημα. Επίσης δίνουμε και αριθμητικά αποτελέσματα για δύο μη κυκλικά προβλήματα αποδεικνύοντας ότι τα συμπεράσματα για το κυκλικό πρόβλημα ισχύουν και στην περίπτωση μη κυκλικών γεωμετριών.

Κεφάλαιο 3

Στο Κεφάλαιο 3 εφαρμόζουμε την ΜΒΠ για την εύρεση των ιδιοτιμών κυματοδηγών με ιδανικά αγώγιμα τοιχώματα, τυχαίας διατομής. Εξετάζουμε απλούς και πολλαπλούς συνεκτικούς χώρους.

Στην πρώτη ενότητα παρουσιάζουμε βασικά στοιχεία θεωρίας ανάλυσης ρυθμών κυματοδήγησης μεταλλικών κυματοδηγών. Στην συνέχεια αναλύουμε τον τρόπο με τον οποίο εφαρμόζεται συμβατικά η ΜΒΠ για την εύρεση των ιδιοτιμών. Συγκεκριμένα, θεωρούμε ότι το πεδίο εντός του κυματοδηγού είναι αποτέλεσμα επαλληλίας των πεδίων που εκπέμπουν ΒΠ που βρίσκονται εκτός του κυματοδηγού. Εφαρμόζοντας την οριακή συνθήκη σε έναν αριθμό από ΣΣ στο αγώγιμο σύνορο του κυματοδηγού, καταλήγουμε σε ένα ομογενές γραμμικό σύστημα. Αν το σύστημα είναι τετραγωνικό, έχει μη συνήθεις λύσεις όταν η ορίζουσα του συστήματος είναι μηδέν οπότε κατασκευάζοντας το διάγραμμα της ορίζουσας συναρτήση του κυματάριθμου k προκύπτει ένα διάγραμμα τα τοπικά ελάχιστα του οποίου αντιστοιχούν σε ιδιοτιμές του κυματοδηγού. Αν το σύστημα είναι υπερκαθορισμένο, τότε οι ιδιοτιμές προκύπτουν από τα μέγιστα του *αριθμού κατάστασης* του πίνακα εμπέδησης. Το πρόβλημα με συμβατική αυτή προσέγγιση είναι η εμφάνιση εσφαλμένων διακριτών και συνεχών ιδιοτιμών.

Το πρόβλημα των εσφαλμένων ιδιοτιμών λύνεται αν προσθέσουμε μια πηγή διέγερσης στο αρχικό πρόβλημα. Η πηγή διέγερσης μπορεί να είναι εσωτερική (νημάτιο ρεύματος) ή εξωτερική

(νημάτιο ρεύματος ή επίπεδο κύμα). Τώρα το πρόβλημα χαρακτηρίζεται από μια μη ομογενή οριακή συνθήκη δεδομένου ότι έχουμε προσπίπτον πεδίο. Εφαρμόζοντας την ΜΒΠ προκύπτει ένα μη ομογενές γραμμικό σύστημα με άγνωστές ποσότητες τα πλάτη των ρευμάτων των νηματίων. Λύνοντας το σύστημά, υπολογίζουμε τα πλάτη και στη συνέχεια το πεδίο στον εσωτερικό χώρο του κυματοδηγού. Ο εντοπισμός των ιδιότιμών βασίζεται στον εντοπισμό των συντονισμών της κοιλότητας του κυματοδηγού με την πηγή διέγερσης. Αυτό επιτυγχάνεται με τον ορισμό μιας *συνάρτησης απόκρισης* η οποία ουσιαστικά υπολογίζει τη μέση τιμή του τετραγώνου του πλάτους του ολικού πεδίου σε έναν αριθμό σημείων εντός του κυματοδηγού, τα οποία έχουν επιλεγεί τυχαία. Φτιάχνοντας το διάγραμμα της συνάρτησης απόκρισης συναρτήση του κυματάριθμου k προκύπτουν καμπύλες συντονισμού οι κορυφές των οποίων αντιστοιχούν στις ιδιοτιμές του κυματοδηγού. Η μέθοδος εφαρμόζεται κατά τον ίδιο τρόπο σε κυματοδηγούς με πολλαπλά συνεκτικούς χώρους με την διαφορά ότι πολλαπλές οριακές συνθήκες

Μέσω του κυκλικού προβλήματος το οποίο μπορει να λυθεί αναλυτικά, αποδεικνύουμε ότι για την χρήση της εξωτερικής πηγής διέγερσης είναι απαράιτητο να χρησιμοποιηθεί κάποια μέθοδος κανονικοποίησης ώστε το πεδίο εντός της κοιλότητας του κυματοδηγού να μην είναι μηδέν, και να μπορούν να εντοπισθούν συντονισμοί. Δείχνουμε επίσης ότι για την περίπτωση εσωτερικής διέγερσης δεν χρειάζεται κάποια μέθοδος κανονικοποίησης. Τέλειώνοντας το θεωρητικό μέρος, τονίζουμε την επίδραση της απόκλισης των πλατών των βοηθητικών ρευμάτων στον υπολογισμό των ιδιοτιμών.

Στην τελευταία ενότητα παρουσιάζουμε αριθμητικά αποτελέσματα εύρεσης ιδιοτιμών για πλήθος από γεωμετριές, απλά και πολλαπλά συνεκτικές. Συγκρίνουμε τα αποτελέσματα μας με την *Μέθοδο Πεπερασμένων Στοιχείων* (ΜΠΣ) και παρατηρούμε ταύτιση στα εξαγόμενα αποτελέσματα. Επίσης εξετάζουμε αριθμητικά και την περίπτωση που το διηλεκτρικό του κυματοδηγού εμφανίζει απώλειες.

Κεφάλαιο 4

Το Κεφάλαιο 4 αποτελεί συνέχεια του Κεφαλαίου 3 με την έννοια ότι παρουσιάζουμε έναν εναλλακτικό τρόπο προσδιορισμού των ιδιοτιμών εκτός από την συνάρτηση απόκρισης. Συγκεκριμένα, αποδεικνύουμε ότι είναι δυνατός ο προσδιρισμός των ιδιοτιμών από τις τιμές των πλατών των βοηθητικών ρευμάτων.

Ξεκινώντας από το κυκλικό πρόβλημα, και συγκεκριμένα από τις εκφράσεις των οριακών τιμών των ΜΒΠ ρευμάτων, διαπιστώνουμε ότι όταν ο κυματάριθμος προσεγγίζει μια ιδιοτιμή ο ν-οστός όρος της σειράς της οριακής τιμής του ΜΒΠ ρεύματος τείνει στο άπειρο. Για ένα πεπερασμένο αριθμό ΒΠ αυτό σημαίνει ότι τα πλάτη τους παίρνουν μεγάλες τιμές, άρα και η απόλυτη τιμή ενός διανύσματος με στοιχεία τα πλάτη των ΒΠ. Το διάνυσμα αυτό ονομάζεται *Διάνυσμα Βοηθητικών Πηγών* (ΔΒΠ) και στο διάγραμμα της απόλυτης τιμής του συναρτήση του κυματάριθμου k θα υπάρχουν μέγιστα τα οποία αντιστοιχούν στις ιδιοτιμές του κυματοδηγού.

Η μέθοδος αυτή υπέρτερει έναντι της συνάρτησης απόκρισης, στο ότι είναι πιο απλή αλγοριθμικά άρα και πιο γρήγορη στον υπολογισμό των ιδιοτιμών. Επίσης, τα διαγράμματα που προκύπτουν με τη ΔΒΠ προσέγγιση, έιναι πιο ομαλά από αυτά της συνάρτησης απόκρισης. Ως εκ τούτου, είναι πιο εύκολο να εντοπιστούν με αυτοματοποιημένο τρόπο οι ιδιοτιμές.

Η μέθοδος λειτουργεί και σε μη κυκλικές γεωμετρίες όπως αποδεικνύεται από τα αριθμητικά αποτελέσματα για δύο κυματοδηγούς. Στην συνέχεια μελετάμε την επίδραση της απόκλισης των

βοηθητικών ρευμάτων στην εύρεση των ιδιοτιμών μέσω του ΔΒΠ. Αποδεικνύουμε για την περίπτωση μιας σύνθετης γεωμετρίας ότι, αν οι ταλατώσεις δεν είναι έντονες υπολογίζονται οι σωστές ιδιοτιμές.

Τέλος, προτείνουμε έναν αλγόριθμο μέσω του οποίου επιταχύνεται ο υπολογισμός των ιδιοτιμών. Ο αλγόριθμός βασίζεται στο ότι είναι πιο γρήγορο να βρίσκεις την τιμή της Hankel συνάρτησης από έναν προκαθορισμένο πίνακα τιμών, παρά να την υπολογίζεις κατά την συμπλήρωση του πίνακα εμπέδησης. Τα αριθμητικά αποτελέσματα δείχνουν μια πολύ μεγάλη πτώση των χρόνων υπολογισμού με τη χρήση αυτής της τεχνικής.

Κεφάλαιο 5

Στο Κεφάλαιο 5 συνεχίζουμε με την εφαρμογή της ΜΒΠ σε προβλήματα ιδιοτιμών, αυτή τη φορά διηλεκτρικών κυματοδηγών μονού και πολλαπλών ρυθμών.

Αρχικά, παρουσιάζουμε βασικά σημεία της θεωρίας των διηλεκτρικών κυματοδηγών. Εξετάζουμε δύο περιπτώσεις: i) το πρόβλημα να μην περιέχει πηγή διέγερσης ii) να περιέχει πηγή διέγερσης. Σε σχέση με την δεύτερη περίπτωση, δεδομένου ότι οι διηλεκτρικοί κυματοδηγοί υποστηρίζουν την μετάδοση υβριδικών ρυθμών, απαιτούνται δύο πηγές διέγερσης, ένα νημάτιο ηλεκτρικού και ένα νημάτιο μαγνητικού ρεύματος.

Το ζητούμενο είναι: για συγκεκριμένη συχνότητα k_0, ποιες είναι οι επιτρεπτές τιμές της σταθεράς μετάδοσης(ιδιοτιμές) β, για τις οποίες έχουμε μετάδοση ρυθμού με την ηλεκτρομαγνητική ενέργεια κοντά στον πυρήνα του διηλεκτρικού κυματοδηγού. Στην περίπτωση αυτή, στην διατομή του πυρήνα θα υπάρχει στάσιμο κύμα ενώ στην διατομή του περιβλήματος/επένδυσης, λανθάνον κύμα.

Η συμβατική εφαρμογή της ΜΒΠ αντιστοιχεί στην περίπτωση της μη ύπαρξης πηγής διέγερσης. Το πεδίο στην περιοχή του πυρήνα είναι η επαλληλία των πεδίων που εκπέμπουν ζευγάρια ηλεκτρικών και μαγνητικών νηματίων που βρίσκονται πάνω σε βοηθητική επιφάνεια μέσα στο περίβλημα/επένδυση. Το πεδίο στην περιοχή του περιβλήματος είναι η επαλληλία των πεδίων που εκπέμπουν ζευγάρια ηλεκτρικών και μαγνητικών νηματίων που βρίσκονται πάνω σε βοηθητική επιφάνεια μέσα στον πυρήνα. Εφαρμόζοντας την οριακή συνθήκη στο φυσικό σύνορο, προκύπτει ομογενές γραμμικό σύστημα το οποίο αν είναι τετραγωνικό, οι ιδιοτιμές προκύπτουν από τα τοπικά ελάχιστα της ορίζουσας, σε ένα διάγραμμα της συναρτήση του β. Το πρόβλημα με αυτή την προσέγγιση είναι ότι πάντα προκύπτουν διακριτές εσφαλμένες ιδιοτιμές.

Εναλλακτικά, προσθέτουμε στην ΜΒΠ δύο βοηθητικές πηγές (νημάτια ηλεκτρικού και μαγνητικού ρεύματος) τοποθετημένες εντός του πυρήνα. Τώρα ζητάμε τις τιμές του β για τις οποίες ο πυρήνας του διηλεκτρικού κυματοδηγού συντονίζεται με τις πηγές διέγερσης. Το σκεδαζόμενο πεδίο σε κάθε περιοχή είναι η επαλληλία των πεδίων που εκπέμπουν οι αντίστοιχες βοηθητικές πηγές, όπως ακριβώς και στην συμβατική εφαρμογή της MAS. Εφαρμόζοντας την οριακή συνθήκη σε έναν αριθμό από σημεία του φυσικού συνόρου, προκύπτει ένα γραμμικό σύστημα με αγνώστους, τα πλάτη των βοηθητικών ρευμάτων. Η εύρεση τους οδηγεί στον υπολογισμό των πεδίων σε κάθε περιοχή (πυρήνας και περίβλημα). Ο εντοπισμός των ιδιοτιμών βασίζεται σε μια συνάρτηση απόκρισης η οποία λαμβάνει υπόψη τις τιμές του ηλεκτρικού και του μαγνητικού πεδίου εντός του πυρήνα. Όταν μεγιστοποιείται αυτή η συνάρτηση έχουμε στάσιμο κύμα στον πυρήνα και λανθάνον κύμα στο περίβλημα και η τιμή του β αποτελεί ιδιοτιμή του κυαμτοδηγού. Με ένα διάγραμμα της συνάρτησης απόκρισης συναρτήση του β μπορούμε να

εντοπίσουμε όλες τις ιδιοτιμές του διηλεκτρικού κυματοδηγού. Η μέθοδος εφαρμόζεται και στην περίπτωση διηλεκτρικών κυματοδηγών πολλαπλών ρυθμών με τη διαφορά ότι έχουμε δύο φυσικά σύνορα στα οποία πρέπει να εφαρμοστεί η οριακή συνθήκη.

Στην τελευταία ενότητα παρουσιάζουμε αριθμητικά αποτελέσματα τα οποία προέκυψαν με την εφαρμογή της ΜΒΠ με δύο πηγές διέγερσης (ΜΒΠ-ΔΠΔ). Εξετάζονται πολλές γεωμετρίες, μονού και πολλαπλών ρυθμών. Τα αποτελέσματα συγκρίνονται με την ΜΠΣ και υπάρχει πολύ καλή συμφωνία. Τονίζουμε ότι με την ΜΒΠ-ΔΠΔ, δεν εμφανίζονται διακριτές εσφαλμένες ιδιοτιμές αν οι πηγές διέγερσης είναι τοποθετημένες εντός μιας *βελτιστης καμπύλης*.

Κεφάλαιο 6

Στο Κεφάλαιο 6 εφαρμόζουμε την ΜΒΠ για τον υπολογισμό της ηλεκτρομαγνητικής θωράκισης του μονοστρωματικού και πολυστρωματικού γραφενίου σε θωρακίσεις με κυλινδρική γεωμετρία.

Αρχικά τονίζουμε την σημασία της ηλεκτρομαγνητικής θωράκισης για την προστασία ηλεκτρονικών συστημάτων και βιολογικών οργανισμών από ηλεκτρομαγνητικές παρεμβολές. Τα πιο συνηθισμένα υλικά για θωράκιση είναι τα μέταλλα, τα οποία όμως εμφανίζουνε διάφορα μειονεκτήματα όπως μεγάλο βάρος, ανελαστικότητα, αδιαφάνεια, οξείδωση κ.α. Για τον λόγο αυτό τα τελευταία χρόνια χρησιμοποιούνται εναλλακτικά υλικά με βάση τον άνθρακα. Ένα από αυτά τα υλικά είναι το γραφένιο, το πρώτο διδιάστατο υλικό που κατασκευάστηκε από τον άνθρωπο δεδομένου ότι έχει πάχος 0.36 nm.

Στην συνέχεια παρουσιάζουμε τις ηλεκτρονικές ιδιότητες του γραφενίου. Ο λόγος για τον οποίο το γραφένιο εμφανίζει υψηλή αγωγιμότητα είναι ο τρόπος με τον οποίο συνδέονται μεταξύ τους τα άτομα του άνθρακα. Η αγωγιμότητα του γραφενίου δίνεται από την σχέση του Kubo, και στο ραδιοφωνικο/μικροκυματικό φάσμα, ξεπερνάει την αγωγιμότητα του χαλκού. Η αγωγιμότητα του γραφενίου μπορεί να ρυθμιστεί μεταβάλλοντας το επίπεδο Fermi του γραφενίου.

Κατά την εφαρμογή της συμβατικής MAS σε περιπτώσεις διατάξεων με ηλεκτρομαγνητική θωράκιση, υπάρχει αδυναμία υπολογισμού του πεδίου εντός της περιοχής υψηλής αγωγιμότητας. Στην περίπτιωση του γραφενίου υπάρχει και το πρόβλημα του πολύ μικορύ πάχους. Αν' αυτού προσμοιώνουμε το γραφένιο ως οριακή συνθήκη μέσω της οποίας υπολογίζουμε το πεδίο εντός της θωρακισμένης περιοχής αν γνωρίζουμε την τιμή του πεδίου στην εξωτερική περιοχή χωρίς όμως να υπολογίζουμε το πεδίο εντος του γραφενίου. Το αποτέλεσμα είναι ένα γραμμικό σύστημα με άγνωστες ποσότητες τα πλάτη των ΒΠ. Με την λύση του συστήματος προκύπτουν και οι τιμές των πεδίων σε κάθε περιοχή άρα και της ηλεκτρομαγνητικής θωράκισης του γραφενίου.

Στην τελευταία ενότητα παρουσιάζουμε αριθμητικά αποτελέσματα για ποικίλες κυλινδρικές γεωμετρίες με το μονοστρωματικό γραφένιο ως υλικό θωράκισης. Συγκεκριμένα προτείνουμε θωράκιση με γραφένιο πάνω σε γυαλί καθότι το γραφένιο επικάθεται αποτελεσματικά (χωρίς να χάνει τις ιδιότητες του) πάνω σε διοξείδιο του πυριτίου. Τα αριθμητικά αποτελέσματα δείχνουν ότι το γραφένιο μπορεί να προσφέρει θωράκιση έως και 40 dB στο ραδιοφωνικο/μικροκυμματικό φάσμα. Διερευνάται και η περίτπωση τριστρωματικού (Α'ΑΑ) γραφενίου πάνω σε γυαλί με ηλεκτρομαγνητική θωράκιση της τάξης των 45 dB. Επίσης αποδεικνύεται και η επίδραση του επιπέδου Fermi στην θωράκιση του γραφενίου.

Κεφάλαιο 7

Στο τελευταίο Κεφάλαιο της διατριβής κάνουμε μια σύνοψη των προηγούμενων κεφαλαίων και παρουσιάζουμε μελλοντικά σχέδια συνέχισης της έρευνας

Contents

List of Figures

List of Tables

Chapter 1

Introduction

In many electromagnetic problems, such as scattering analysis, antenna modelling, waveguiding systems design, electromagnetic shielding and others, researchers often deal with boundary value problems. In all these situations, a crucial factor that is taken into consideration is the geometry of the problem. If the geometry is simple, as it is for example in the case of wave scattering from a spherically or elliptically shaped body, then a solution is possible by using Maxwell's equations and analytical mathematical techniques. For more complex geometries on the other hand, numerical methods should be utilized to obtain a solution. The choice of a numerical technique depends on whether the problem under consideration is linear or non-linear, with the latter being considerably more difficult to handle.

Generally, the electromagnetic system under consideration is described by a *governing equation* of the form

$$L[\phi] = s \tag{1.1}$$

where L is a differential or integral operator (linear or non-linear) describing the problem, ϕ is the unknown scalar or vector field quantity, and s is the scalar or vector *source function* which generates the field ϕ. This equation has to be solved for ϕ in a domain D. Fortunately in most of the cases, L is a *linear* differential or integral operator, a fact that stems from the linearity of the Maxwell's equations for linear media. As for the boundary conditions, they range from Dirichlet or Neumann conditions to more sophisticated impedance, radiation, and higher order conditions.

It is not rare for the same problem to have two linear governing equations, a differential and an integral (with the second usually derived from the first). It is up to the researcher to decide which of these equations suits better the solution of the problem. Each approach has its advantages and disadvantages which are discussed in the next section through a simple scalar wave propagation problem.

1.1 Differential versus Integral Equations

Let us consider the case of a wave propagating in an unbounded, linear, homogenous, and isotropic medium. The wave may be elastic (such as an acoustic wave) or electromagnetic [1]. In the time domain this physical process is described by the well known wave equation

$$\nabla^2 \varphi(\mathbf{r},\ t) - \frac{1}{c^2}\frac{\partial^2 \phi(\mathbf{r},t)}{\partial t^2} = s(\mathbf{r},t) \tag{1.2}$$

where $\phi(\mathbf{r},t)$ is the scalar field which may represent the pressure of an acoustic wave or a electric/magnetic field component of an electromagnetic wave, $s(\mathbf{r},t)$ represents the source of the field, c is the speed of the wave in the medium, $\mathbf{r}$ is the position

vector of the observation point, and t is the time of observation. Assuming that ϕ is a harmonic wave (thus s is a harmonic source) with a depedence of the form $e^{i\omega t}$, (1.2) becomes a Helmhotz equation in the frequency domain i.e.,

$$\nabla^2\varphi(\mathbf{r},\omega) + k^2\varphi(\mathbf{r},\omega) = s(\mathbf{r},\omega), \;\; k = \frac{\omega}{c} \tag{1.3}$$

where ω is the angular frequency, and k is the wavenumber of the harmonic wave. With the derivation of (1.3) we've arrived at a governing equation of the problem which has a differential form. By comparing (1.3) with (1.1) it is seen that $L = \nabla^2 + k^2$ which is a *linear operator*. The linearity of the operator implies that the *principle of superposition* holds for this system. Thus, assuming that the source $s(\mathbf{r},\omega)$ is generated by a number of *point sources*, the field $\phi(\mathbf{r},\omega)$ is equal to the superposition of the point sources fields.

In mathematical physics, the point source field functions are classified by different names such as *Green's functions*, *fundamental solutions*, or *analytic solutions* and are solutions of the Helmhotz equation with the right hand side replaced by a unit amplitude point source i.e.,

$$\nabla^2 g(\mathbf{r},\mathbf{r}') + k^2 g(\mathbf{r},\mathbf{r}') = -\delta(\mathbf{r}-\mathbf{r}') \tag{1.4}$$

with the ω dependence being supressed from now on for every quantity. Here $g(\mathbf{r},\mathbf{r}')$ is the Green's function, $\mathbf{r}$ is the position vector of the observation point, $\mathbf{r}'$ is the position vector of the point source, and $\delta(\mathbf{r}-\mathbf{r}')$ is the Dirac delta function which is suitable to represent a point source at $\mathbf{r}'$. The solutions of (1.4) depend on the geometry of the problem and can be one of the following,

$$g(\mathbf{r},\mathbf{r}') = \begin{cases} \frac{e^{-ik|\mathbf{r}-\mathbf{r}'|}}{4\pi|\mathbf{r}-\mathbf{r}'|}, \; for\ 3D\ problems \\ \\ \frac{i}{4}H_0^{(2)}(k|\mathbf{r}-\mathbf{r}'|), \; for\ 2D\ problems \end{cases} \tag{1.5}$$

with the first Green's fucntion representing a spherical wave suitable for 3D problems, and $H_0^{(2)}(k|\mathbf{r}-\mathbf{r}'|)$ is a Hankel function of the zeroth order and the second kind, that is suitable to represent 2D cylindrical waves. With the aid of the Green's functions and applying the principle of superposition we can arrive at an integral expression (superposition of *infinite* number of point sources) for the field $\phi(\mathbf{r})$ which is given by,

$$\varphi(\mathbf{r}) = \int_V g(\mathbf{r},\mathbf{r}')s(\mathbf{r}')\mathbf{dr}' \tag{1.6}$$

where V is the volume where the source $s(\mathbf{r}')$ extends.

Energy conservation reasoning requires that the source $s(\mathbf{r}')$ is induced by an impressed field. In the context of a scattering problem this can be an *incident field* wave $\phi_{\text{inc}}(\mathbf{r})$, that impinges on the body of volume V as illustrated in Fig. (1.1). In this case, $\phi(\mathbf{r})$ is the *scattered field* which is radiated by the induced source $s(\mathbf{r}')$. For the sake of simplicity, let us assume that the scattering object is impenetrable, such as perfect electric conductor (PEC) in electromagnetics, or a hard elastic object in acoustics. By definition, the total field on the surface S and inside the body is zero, thus the induced source $s(\mathbf{r}')$ exists only on S i.e., it is a *surface source*. The boundary condition on S is expressed mathematically by the following *integral equation*

$$\int_S g(\mathbf{r},\mathbf{r}')s(\mathbf{r}')dS' = -\phi_{\text{inc}}(\mathbf{r}), \;\; \mathbf{r}\in S \tag{1.7}$$

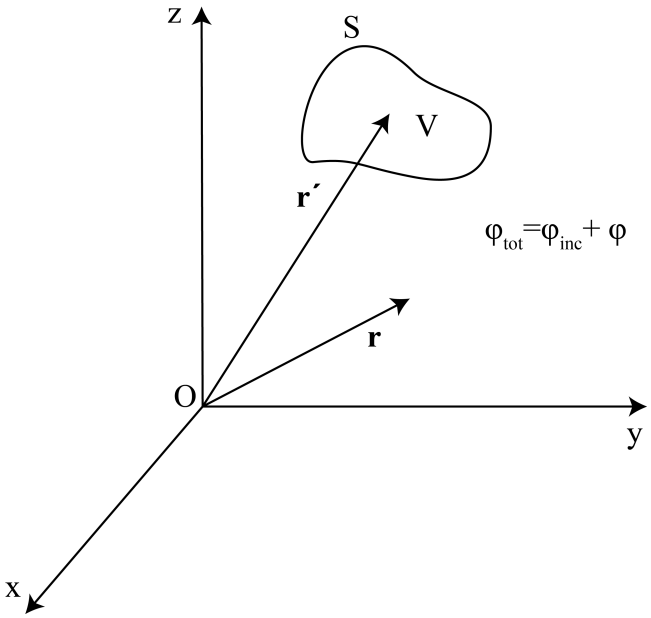

FIGURE 1.1: Geometry of a general 3D scattering problem

with only unknown the source function $s(\mathbf{r}')$. This is the second governing equation of the problem because when it is solved for $s(\mathbf{r}')$, we can find the scattered field $\phi(\mathbf{r})$ from (1.6), which is the required quantity.

It should be noted that in case of a penetrable object, a volume current is induced since, by definition, the field inside the body is not zero. We can, however, apply the equivalence principle [2] in order to obtain an equivalent problem where the scattered field is generated by surface sources on the boundary thus, arriving in a surface integral equation similar to the impenetrable case. In principle, we can arrive at a surface integral equation for any boundary value problem.

We are at a point where we have two governing equations available, the differential (1.3), and the integral (1.7), so the question arises on which one to choose to solve numerically. For the differential equation, the unknown quantity is the scattered field function $\phi(\mathbf{r})$ which must be calculated in the whole 3D space of the domain. In the case of the integral equation, the unknown quantity is the source function $s(\mathbf{r}')$ which must be computed on a 2D manifold or surface. In the context of numerical methods, this means that the differential equations require more unknowns than the surface integral equations. This is an important advantage of integral equation solvers over differential equation solvers, since it translates to lower computational time especially when the problem size is very large. Another advantage of solving an integral equation is that the Green's function is an exact propagator that propagates a field from point A to point B. Hence, there is no grid dispersion error of the kind that exists in numerical differential equation solvers where the field is propagated from point A to point B via a numerical grid [3].

On the other hand, integral-equation solvers must calculate integrals with a singular integrand during the filling of the impedance matrix (see 1.2). Another disadvantage of the integral equation numerical techniques, is that their matrix system is much more dense i.e., their impedance matrix has many more non-zero elements than their differential solver counterparts. As a result they may require more storing capacity and central processing unit (CPU) time to solve. However, modern integral equation solver codes have mitigated significantly these requirements [4].

1.2 Integral equations and the Method of Moments

The numerical method that is ordinarily used to solve surface integral equations is the Method of Moments (MoM). In order to get a firm understanding of the differerent aspects of MoM, it will be applied in a simple two dimensional electromagnetic scattering problem [5].

1.2.1 Description of the problem

A PEC cylinder, with an arbitrarily shaped cross section, is infinitely extended along the z-axis. The cylinder is surrounded by a region R which is filled with a homogeneous, isotropic, and non-magnetic material with permitivity ε, and vacuum permeability μ_0. A TM_z harmonic plane wave (a wave with an electric field along the z axis), propagating in R illuminates the PEC cylinder inducing a z-directed current density J_z on its surface which will be the source of a z-directed scattered electric field E_{sc}. Although this is a three dimensional problem, translational invariance dictates that all the quantities in this configuration must be independent of the z coordinate. This means we can study the scattering problem in two dimensions, and specifically in the cross section of the configuration (xy-plane) which is depicted in Fig. (1.2).

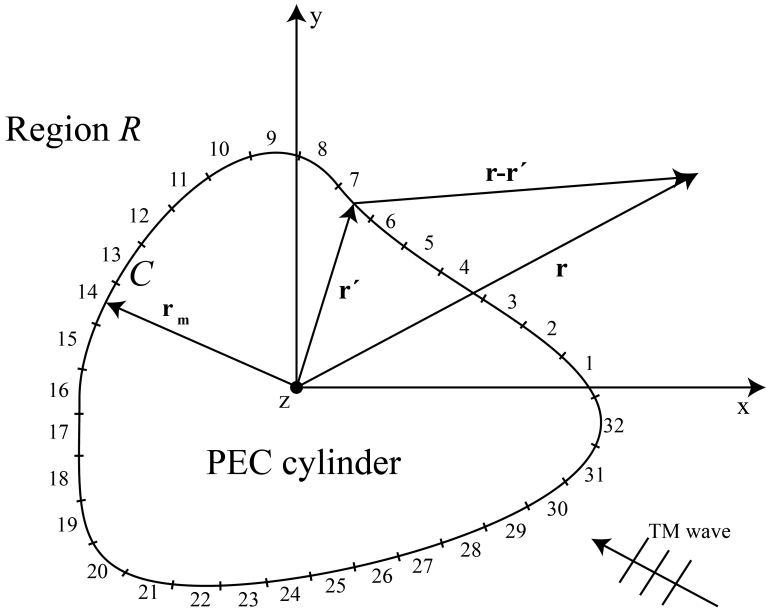

FIGURE 1.2: MoM configuration of the 2D scattering problem of a TM wave from a PEC cylinder with an arbitrary cross section. The boundary C is meshed into segments ΔC_n with n=1,.....,32.

1.2.2 Formulating the Governing Integral Equation

The relationship between the scattered field E_{sc} and its source J_z is found by applying the Maxwell equations, leading to the following Helmhotz equation

$$\nabla^2 E_{sc}(\mathbf{r}) + k^2 E_{sc}(\mathbf{r}) = \mathrm{i}\omega\mu_0 J_z \tag{1.8}$$

with $\mathbf{r}$ the observation point, and k the wavenumber. (1.8), is the governing differential equation of the problem, analogous to (1.3). Due to the PEC boundary the

total tangential field on C is zero which is mathematically stated by the following boundary condition,

$$E_{inc} + E_{sc} = 0 \tag{1.9}$$

The linearity of (1.8) permits us to express E_{sc} as a linear combination of the two dimensional cylindrical wave fields radiated by the infinite number of line sources, pertaining to J_z on the PEC boundary C. This results to the following integral,

$$E_{sc} = -\frac{\omega\mu_0}{4}\int_C J_z(\mathbf{r}')H_0^{(2)}(k|\mathbf{r}-\mathbf{r}'|)dl', \tag{1.10}$$

where $\mathbf{r}$ is the position vector of the observation point, $\mathbf{r}'$ is the position vector of a point source, $H_0^{(2)}(k|\mathbf{r}-\mathbf{r}'|)$ is the two dimensional Green's function. The integral of (1.10) is analogous to that of (1.6) with the integration implemented on the boundary curve C instead on surface S, due to the fact that the considered problem is two dimensional. Next we apply the boundary condition (1.9) to arrive at the following integral equation

$$E_{inc}(\mathbf{r}) = \frac{\omega\mu_0}{4}\int_C J_z(\mathbf{r}')H_0^{(2)}(k|\mathbf{r}-\mathbf{r}'|)dl', \quad \mathbf{r} \text{ and } \mathbf{r}' \in C \tag{1.11}$$

This is the integral equation that governs the problem, analogous to (1.7), with unknown the current density $J_z(\mathbf{r}')$.

1.2.3 Discretization of the Integral Equation

The next step in the MoM analysis is the discretization of the governing equation (1.11) i.e., transforming it to a *matrix equation* that can be solved in a computer resulting in an approximation of J_z. The discretization process consists of three steps: meshing the boundary, expanding the surface current function J_z in a function basis, and point matching the boundary condition.

Meshing the boundary With the meshing procedure, the boundary contour C is divided into N segments ΔC_n. Very small segments will yield a better approximation of J_z but will increase the number of the unknowns in the matrix equation. The segementation of C is illustrated in Fig. (1.2).

Expanding the surface current function In this step we expand J_z in a basis of N functions $f_n(\mathbf{r}')$, each one being matched with a segment ΔC_n. This means that J_z is approximated by the summation

$$J_z(\mathbf{r}') = \sum_{n=1}^{N} J_n f_n(\mathbf{r}') \tag{1.12}$$

with I_n being the expansion coefficients. Thus, the computation of J_z now relies on the determination of the N unknown expansion coefficients I_n. A frequent choice for f_n are the pulse functions which are defined as

$$f_n(\mathbf{r}') = \begin{cases} 1 & on\ \Delta C_n \\ 0 & on\ \Delta C_m \end{cases} . \tag{1.13}$$

By applying (1.12) and (1.13) in (1.11) the following equation is derived,

$$E_{inc}(\mathbf{r}) = \frac{\omega\mu_0}{4}\sum_{n=1}^{N} J_n \int_{\Delta C_n} f_n(\mathbf{r}')H_0^{(2)}(k|\mathbf{r}-\mathbf{r}'|)dl'. \tag{1.14}$$

The equation above is not a matrix equation yet since it depends on the continuous variable $\mathbf{r}$.

Point matching the boundary condition To remove the $\mathbf{r}$ dependence from (1.14) we apply the boundary condition on N discrete points of C which we will refer to as *collocation points* (CP's), with position vectors $\mathbf{r}_m$ usually pointing in the middle of the segments as seen in Fig. (1.2). This is carried out by multiplying each side of (1.14) with $\delta(\mathbf{r}-\mathbf{r}_m)$ and then integrating all over C. By doing so we have

$$\int_C \delta(\mathbf{r}-\mathbf{r}_m)E_{inc}(\mathbf{r})dl = \frac{\omega\mu_0}{4}\sum_{n=1}^{N} J_n \int_C \delta(\mathbf{r}-\mathbf{r}_m)\int_{\Delta C_n} H_0^{(2)}(k|\mathbf{r}-\mathbf{r}'|)f_n(\mathbf{r}')dl'dl,$$
$$m = 1, ..., N \tag{1.15}$$

Now the left-hand side is only dependent in m and the double integral on the right hand side is only dependent on m, n. Thus, (1.15) is a set of linear equations that can be written in a more concise form as

$$[V] = [Z][I] \tag{1.16}$$

where $[V]$ is a $N \times 1$ column vector with elements the values of E_{inc} on the collocation points, $[I]$ is an $N \times 1$ column vector with elements the unknown coefficients J_n, and [Z] is the $N \times N$ impedance matrix with elements the integrals

$$Z_{mn} = \frac{\omega\mu_0}{4}\int_{\Delta C_n} H_0^{(2)}(k|\mathbf{r}_m-\mathbf{r}_n|)dl' \tag{1.17}$$

where $\mathbf{r}_n$ is the position vector of a point in the segment ΔC_n. For the diagonal elements of [Z] ($m = n$) we have $\mathbf{r}_m = \mathbf{r}_n$ thus, the integrand of (1.17) is singular (the Hankel function is not defined at zero). The integral in this case can be evaluated approximately, but analytically. Assuming large N the segments ΔC_n can be approximated by a straight line and (1.17) is written as

$$Z_{mn} = \frac{\omega\mu_o}{4}\Delta C_n H_0^{(2)}(k|\mathbf{r}_m-\mathbf{r}_n|) \tag{1.18}$$

Then we use the following small argument approximation for the Hankel function (since the argument goes to zero for the diagonal elelments),

$$H_0^{(2)}(x) \sim 1 - \mathrm{i}\frac{2}{\pi}\log(\frac{\gamma x}{2}) \tag{1.19}$$

which is then used to (1.18) to obtain

$$Z_{mn} \sim \frac{\omega\mu_0\Delta C_n}{4}\left\{1 - \mathrm{i}\frac{2}{\pi}\log\left(\frac{\gamma k\Delta C_n}{4e}\right)\right\}, \quad for \;\; m = n \tag{1.20}$$

where $\gamma = 1.781$. After inverting $[Z]$ with the Gaussian elimination process, we can solve (1.15) for $[I]$ yielding

$$[I] = [Z]^{-1}[V] \tag{1.21}$$

and use the obtained elements J_n to evaluate the current density J_z via (1.12) and finally the scattered field from (1.10).

1.2.4 Conclusions for MoM

A very important aspect of MoM is the choice of basis functions. Although the pulse functions (1.13) are a convenient choice, they give a step approximation of J_z and a large number of segments are necessary to obtain an acceptable result. Alternatively, other function basis can be used such as the *triangle functions*, which give a piecewise approximation of J_z. Another noteworthy issue is that the choice of the expansion function affects the meshing of the boundary. For example in 3D problems, one popular choice of expansion function is the Rao-Wilton-Glisson (RWG) function. To use this function, the surface of the scatterer has to be discretized into small elements each of which is a triangle [6].

Finally in MoM, evaluations of integrals with singular integrands are required in order to fill the diagonal elements of the impedance matrix [Z]. To treat this, approximations can be used (as indicatively illustrated above) which however affect the accuracy of the surface current determination.

1.3 Generalized Multipole Techniques

The drawback of evaluating singular integrals when applying MoM in order to fill the impedance matrix, led to the development of alternative methods classified as *Generalized Multipole Techniques* (GMT's) [7], [8].

The central principle of these methods is that when applied, an equivalent situation of the original problem is formulated in which the fields in the domain of interest are generated by fictitious *discrete* sources (instead of continuous) which are *displaced from the physical boundary*. The sources are chosen so that their fields are Green's functions of the governing differential equation. The principle of superposition allows us to express the fields in each domain as an expansion of these Green's functions i.e., a weighted superposition of the fields from each discrete source. The unknowns are the expansion coefficients which are determined by point matching the relevant boundary conditions.

Historically, the first published work that applied the concept of field approximation by linear combination of Green's functions is the classic Mie scattering solution for a sphere. In this case the point sources are collocated at the center of the sphere radiating spherical multipole fields. However, this solution is suitable only for spherical geometries. Attempts were made to extend spherical multipole solutions to non spherical geometries, again with a single origin, but with acceptable results limited only for elliptically shaped bodies with low aspect ratios not larger than 2 [9].

The factor that enabled the application to more complex geometries is to place the discrete sources on *multiple positions* resulting to the numerous GMT methods. Although based on the same principle, these methods differ on the type of point sources utilized and their positioning. Some of the established GMT methods are the Discrete Sources Method (DSM), the Yasuura method, the Null field method, and the Method of Auxiliary Sources (MAS) which is the main focus on this dissertation.

1.4 The Fundamentals of the Method of Auxiliary Sources

Most studies attribute the origin of the MAS to Kupradze and his coworkers, some to Mathon and Johnston[10]–[15]. The MAS is distinguished from the other GMT's in that it utilizes Green's functions with poles of zero order (singularities only at the position of the source) i.e., there are no other poles in the neighborhood of the discrete source. This means that the discrete sources of MAS, which are labeled as *Auxiliary Sources* (AS's), are physically interpretable (they have physical significance) and their functions are analytically simpler than others.

The source type used depends on the dimensions of the problem. For two dimensional geometries, infinitely long current filaments which radiate two dimensional cylindrical waves that are proportional to a Hankel function as in (1.5) are the standard choice. In 3D problems, widely used are pairs of Hertzian dipoles, electric and magnetic, that are perpendicular to each other. As for the positoning, conventially the sources are homogeneously placed upon surfaces (or curves in 2D problems) which are labeled as *auxiliary surfaces*, the shapes of which are usually chosen to be similar to the physical boundary.

The electromagnetic fields in each domain are the weighted superpositon of the fields radiated by the AS's. The unknowns are the expansion coefficients which physically represent the current amplitudes of the infinite filaments, or the dipole moments of the Hertzian dipoles. Then the point matching procedure is applied where the boundary condition is enforced on a discrete number of CP's on the boundary. If the number of CP's are equal to the number of AS's then the obtained impedance matrix is square, and the coefficients are found by Gaussian elimination. Alternatively, the linear system may be overdetermined (more CP's than AS's) in order to obtain the most accurate results possible via a pseudo-inverse solution.

1.4.1 2D scattering problem revisited-MAS solution

For a more in depth view on the MAS fundamentals, we revisit the scattering problem of section 1.2. This will permit us to make a direct comparison between MoM and MAS.

According to MAS, an equivalent problem is formulated in which the *PEC cylinder is absent* and the scattered field in region R is the superposition of the fields radiated by a set of N auxiliary sources, in an unbounded region filled with the material of R. The appropriate type of AS's for this case, are electric current filaments of infinite length which are parallel to the axis of the cylinder. These are placed on an auxiliary surface which has a similar shape with the physical boundary, and is inside the PEC in order to avoid singularities in R at the positions of the point sources.

Since this is a 2D problem, it is solved in the cross section of the geometry thus, the auxiliary surface becomes an auxiliary curve C_{aux}, and the current filaments behave as point sources radiating two dimensional cylindrical waves. The 2-D MAS configuration is illustrated in Fig. (1.3). The scattered field is expressed as the superposition of the 2-D cylindrical waves as,

$$E_{sc} = -\frac{\omega\mu_0}{4}\sum_{n=1}^{N} I_n H_0^{(2)}(k|\mathbf{r}-\mathbf{r}_n|) \tag{1.22}$$

where $\mathbf{r}$ is the position vector of a boundary point, $\mathbf{r}_n$ is the position vector of the n-th auxilary point source, and I_n is the current amplitude of the n-th point source (expansion coefficient). Next we apply the point matching technique on N points of

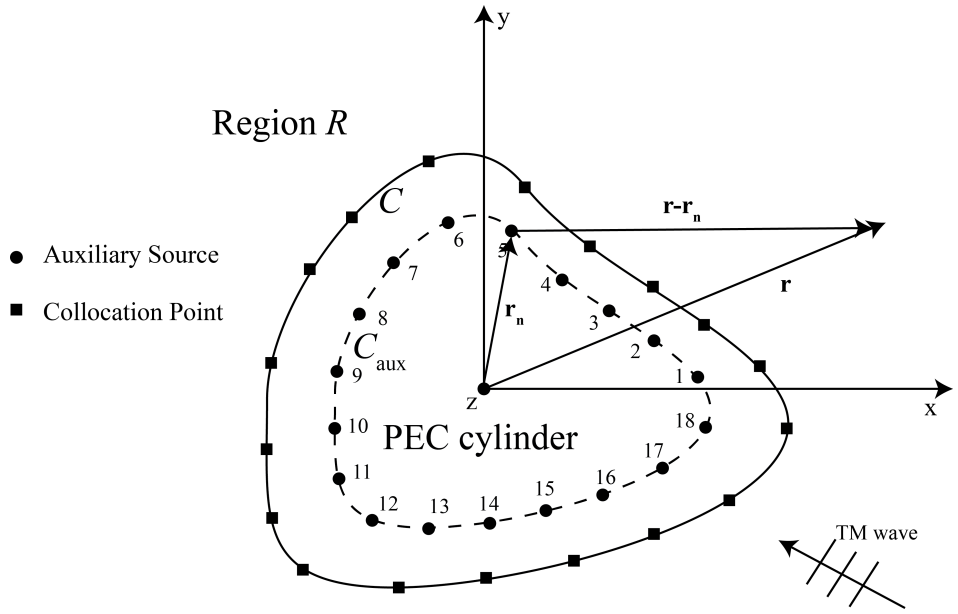

FIGURE 1.3: MAS configuration of the TM wave 2D scattering problem from a PEC cylinder with an arbitrary cross section, where $N = 18$ auxiliary point sources and an equal number of collocation points are defined.

the boundary curve C with position vectros $\mathbf{r}_m$ by following the same procedure as MoM yielding,

$$E_{inc}(\mathbf{r}_m) = \frac{\omega\mu_0}{4}\sum_{n=1}^{N} I_n H_0^{(2)}(k|\mathbf{r}_m - \mathbf{r}_n|),\ m = 1, ..., N \tag{1.23}$$

which is an $N \times N$ linear system. This can be expressed in a form like (1.16) with $[V]$ the $N \times 1$ column vector with elements the values of E_{inc} on the collocation points $\mathbf{r}_m$, [I] is the $N \times 1$ column vector with elements the unknown current amplitudes I_n, and [Z] the $N \times N$ impedance matrix with elements given by $Z_{mn} = H_0^{(2)}(k|\mathbf{r}_m - \mathbf{r}_n|)$ where it is obvious that no integration is involved.

The solution of the system yields the unknown coefficients I_n, and consequently, the scattered field from (1.22).

1.4.2 Comparison between MAS and MoM

The study of the 2D scattering problem allows us the comparison between MAS and MoM.

The first primary feature of MAS is that the sources are postulated as discrete thus, there is no need to mesh the surface in which the sources exist hence, MAS is a *meshless* method. The second important feature of MAS is that the sources are displaced with respect to the physical boundary, eliminating the Green's functions singularity. As a result, the implementation of a MAS code solver is easy since we only need to define a discrete number of sources, the shape and the position of the auxiliary surface (or curve), and finally apply the point matching procedure on a discrete number of collocation points to arrive at the matrix equation. The absense of integral calculations allows the rapid filling of the impedance matrix which means low computational cost in terms of CPU time.

Due to all these factors, and especially in cases where number of the discrete sources required for a convergent solution is similar to the mesh elements used to obtain the same result in MoM, MAS is usually much more efficient. But even in cases where the MAS discretization is denser there exists, in general, a threshold in geometry size under which MAS is computationally less costly than MoM [16].

There are, however, several difficulties that arise when applying the MAS which are related to the location, distribution, and number of the auxiliary sources as well as the collocation points. These are discussed in Section 1.4.3.

1.4.3 Particular Aspects in the Method of Auxiliary Sources

In the previous section we've analyzed the aspects of a conventional MAS application. However, there are boundary value problems that require various approaches with respect the number, type and positioning of auxiliary sources. In much of the standard literature, MAS does not impose any limitations regarding these factors, but numerical and analytical results show that this is not always true, as will be discussed in detail in this thesis. The same applies for the number and positioning of the collocation points.

Alternative source types Instead of current filaments or Hertzian dipoles, other source types may be employed depending on the geometry, or the type of excitation. Auxiliary sources such as the periodic strip model, or the cylindrical-current elements have been used for certain 2D and 3D problems.

Location, distribution, and number of the Auxiliary Sources The choice of location, distribution, and number of the auxiliary sources affect significantly the efficieny of MAS [17], [18]. Unfortunately, these factors are interrelated and at the same time, dependent on the geometry, auxiliary source type, and excitation source type. As a result, it is difficult to establish specific global rules for their definition and for this, many researches rely on empirical rules for each case of study.

For geometries with smooth boundaries, a homogeneous distribution of the auxiliary sources on an auxiliary surface conformal to the physical boundary (same shape) is a convenient and effective choise. However, non-uniform distributions, as well as non-conformal auxilary surfaces have proven to be useful. For example, in a geometry that includes edges (point regions), a denser and non-conformal distribution of the auxiliary sources is proven to be more effective to compute the fields near the edge.

Another important fact is that the distance between the auxiliary surface and the physical boundary -especially in conjuction with how dense is the distribution of the sources- significantly affects the efficiency of the MAS solution.

Also, the convergence rate (how fast the MAS solution approaches the true solution with respect ot the number of auxiliary sources) depends on the relative location of the auxiliary sources with respect to the singularities of the analytic continuation of the field function computed by MAS. Specifically, a convergent solution is guaranteed if there are no singularities between the physical boundary and the auxiliary surface. Otherwise, the MAS solution is not convergent and thus not acceptable however, it may be sufficiently accurate under certain conditions [19], [20]. It must be noted though, that the locations of the field singularities are known a priori only for very special shapes such as circles and ellipses.

Collocation Points In regard to the collocation points, their number is usually taken equal to the number of auxiliary sources and a square impedance matrix is obtained. However, in some cases it is preferable to over-determine the derived matrix equation, and solve it provide a least-squares fit to the boundary condition. In any case, what is checked is the error on the boundary condition. This is done by increasing the number of auxiliary sources and/or collocation points, because between the matching points, the mismatching might be quite significant.

1.5 Outline of the thesis

The scope of this thesis is to highlight theoretical and practical aspects of MAS with the chapters being organized as follows. In Chapter 2, we show that for the problem of transverse electric illumination of a perfect electric conducting cylinder by a magnetic current filament, it is possible for large numbers N of auxiliary sources that the MAS currents diverge and oscillate, while the generated MAS field converges to the exact solution. We demonstrate analytically the occurrence of convergence/divergence phenomena of the currents and fields in this problem and then study the nature of this divergence in detail. In particular, we derive a large-N asymptotic formula for the divergent MAS currents, which captures accurately the important characteristics of the associated inherent oscillations. Numerical results for non circular shapes are also presented.

In Chapter 3, the application of MAS in mode analysis of PEC waveguides is discussed. According to the conventional scheme of MAS, the eigenvalues are obtained by requiring the square impedance matrix to be singular and therefore its determinant to be zero (or its condition number to be large). For large matrices, such computations are complicated and time-consuming. Additionally, these schemes are frequently contaminated with spurious eigenvalues. To overcome the difficulties, an efficient method based on MAS along with an excitation source is proposed. The eigenvalues are obtained by measuring the physical response of the waveguide's domain to this source; thus, an interior problem is always solved. Chapter 3 is a comprehensive presentation of this method and its variants and aims to emphasize fundamental and often unfamiliar attributes. One of the main objectives is to show analytically and numerically that when an internal source is used, the eigenvalues are accurately computed without employing a regularization procedure. The method is applied to hollow simply and multiply connected waveguides with circular, elliptical, and rounded-triangular cross sections. The results are compared with those obtained from COMSOL Multiphysics. Moreover, the phenomenon of divergent and oscillating MAS currents—which may or may not occur depending on the relative position between the auxiliary curve and the excitation source—is discussed. It is emphasized that, with proper care, the phenomenon does not affect the accurate computation of the eigenvalues.

Chapter 4 is a continuation of the previous one where it is shown that the eigenvalues can be determined, more simply, by means of the auxiliary currents vector norm (ACVN). We explain our method analytically for the simple problem of the circular waveguide, apply it numerically to more complicated geometries, and compare our results to those of a finite element method (FEM)-based commercial software. We introduce a Hankel-function lookup procedure, which greatly reduces computational times, and discuss the once again the effect of divergence/oscillations of the auxiliary currents.

The contents of Chapter 5 demonstrate that the MAS-ES is also effective in computing the propagation constants (eigenvalues) β of a cylindrical dielectric waveguide with core of arbitrary cross section. It is emphasized that two excitation sources (an electric and a magnetic current filament lying within the core) are required to excite hybrid modes of the dielectric waveguide; a hollow PEC waveguide requires only one source. The modified method, thus obtained, is named MAS with Two Excitation Sources (MAS-TES). The fact that the propagating modes are localized in the vicinity of the core allows us to determine the eigenvalues by measuring the response of the core to the excitation sources. This is performed by employing a response function $F(\beta)$ which is maximized when a standing wave is formed in the core. Plotting $F(\beta)$ for a dense set of β results in a response curve the peaks of which correspond to the waveguide's eigenvalues. The method is tested for several dielectric waveguides' geometries, including two multimode cases, and it is shown that it is free from discrete and continuous spurious solutions. All the MAS-TES results are compared with those obtained by an FEM-based commercial software and an excellent agreement is exhibited.

Moreover, in Chapter 6 the main objective is to evaluate ideal monolayer graphene as a shielding material for cylindrical configurations in the RF/microwave region. The numerical modeling of the involved structures is performed by the Method of Auxiliary Sources. Particularly, since the standard MAS suffers from numerical difficulties when applied in highly-conductive regions, a modified version of MAS is employed in which the graphene layer is replaced by an Impedance Matrix Boundary Condition (IMBC). The same condition is also applied for the case of a Few Layer Graphene (FLG) shield. The derived numerical results are found to be in excellent agreement with those obtained by FEM-based commercial software.

Lastly, Chapter 7 concludes the thesis by presenting the main coclusions for each chapter, and outlines plans for future work.

Chapter 2

Convergence Analysis Involved in the Method of Auxiliary Sources Applied to Scattering by PEC Cylinders

2.1 Introduction

In [20], MAS was applied to the transverse-magnetic (TM) problem, consisting a perfect electric conductor (PEC) circular cylinder illuminated by an infinitely-long electric current filament. For this problem, MAS involves N electric current filaments, located at an auxiliary radius inside the PEC surface, and radiating electric fields whose sum is required to cancel the incident tangential electric field at N collocation points on the PEC. This leads to a $N \times N$ system with unknowns the MAS currents. Then, the corresponding MAS electric field is obtained by means of the computed MAS currents. It is shown that, if the auxiliary radius is larger than a certain critical radius, the large-N limit of the normalized MAS currents exists and is equal to a continuous surface current, while the MAS field coincides with the true field outside and its analytic continuation inside the scatterer up to the auxiliary surface. However, for an auxiliary radius smaller than the critical one, the normalized MAS currents diverge and oscillate, as $N \to \infty$. Still, the MAS electric field due to the divergent MAS currents converges to the true field. Other works that followed, investigated corresponding phenomena for different boundary-value problems [21]–[23].

In this chapter we extend the results of [20] toward a different direction, specifically to the transverse-electric (TE) case of a PEC cylinder excited externally by a magnetic current filament. Investigating the convergence of MAS for different incident wave polarizations is also important in implementations, like in [24], where a so-called multifilament doublet current method is employed requiring both TE and TM components. First, we consider a continuous version of MAS, in which an auxiliary surface inside the PEC carries an unknown continuous magnetic current density. The scattered magnetic field, generated by this current density, is required to cancel the tangential (azimuth-directed) electric field on the PEC surface. In this way, a first-kind Fredholm integral equation for the current density is obtained. By using analytical arguments, we show that, if the auxiliary radius is greater than a critical radius, the series expressing the magnetic density converges and the generated electric field cancels exactly the tangential electric field on the PEC. However, for auxiliary radii smaller than the critical one, no convergent solution for the magnetic density exists.

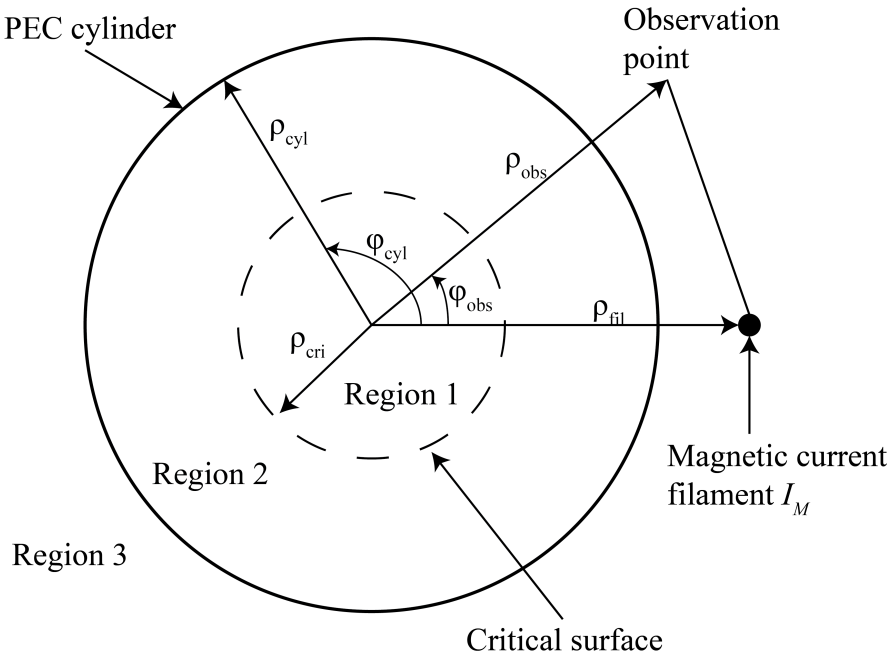

FIGURE 2.1: Geometry of the 2-D scattering problem and regions of the analytic continuation of its exact solution.

Then, we turn to the discrete version of MAS, where the continuous current is replaced by N magnetic current filaments canceling the tangential incident electric field at N collocation points on the PEC surface. A $N \times N$ circulant system thus results, which is solved in closed form by Discrete Fourier Transforms (DFTs). We demonstrate analytically that, as $N \to \infty$, the normalized MAS currents converge to the true continuous surface density if the auxiliary radius is larger than the critical one, while the currents diverge and oscillate if it is smaller. Importantly, the computed MAS fields converge to the exact solution of the boundary-value problem (and to its analytic continuation inside the scatterer) even if the auxiliary radius is smaller than the critical one. These theoretical findings are also supplemented by numerical results for circular and non-circular shapes. Finally, we prove a large-N asymptotic formula for the divergent MAS currents, which predicts accurately the characteristics of the appearing oscillations.

An $e^{-\mathrm{i}\omega t}$ time dependence is assumed and suppressed throughout this chapter with $k = \omega/c \ = 2\pi f/c \ = \omega\sqrt{\mu_0\varepsilon_0}$.

2.2 Exact Solution for the Magnetic Field

The geometrical configuration of the scattering problem is shown in Fig. 2.1. An infinitely-long circular PEC cylinder of radius ρ_{cyl}, with axis along the z-axis, is illuminated by an external z-directed magnetic current filament I_M lying on $(\rho_{\text{fil}}, 0)$ of the x-axis. A point on the PEC surface has polar coordinates $(\rho_{\text{cyl}}, \phi_{\text{cyl}})$, with $\rho_{\text{fil}} > \rho_{\text{cyl}}$. The observation point has coordinates $(\rho_{\text{obs}}, \phi_{\text{obs}})$. The exact expression for the total magnetic field $\mathbf{H} = H_z\hat{\mathbf{z}}$ for $\rho_{\text{obs}} > \rho_{\text{cyl}}$ is given by [2]

$$H_z = -\frac{\omega\epsilon_0}{4} I_M \Big[H_0^{(1)}\left(kR_{\text{obs,fil}}\right) - \sum_{n=-\infty}^{\infty} \frac{J_n'\left(k\rho_{\text{cyl}}\right) H_n^{(1)}\left(k\rho_{\text{obs}}\right) H_n^{(1)}\left(k\rho_{\text{fil}}\right)}{H_n'^{(1)}(k\rho_{\text{cyl}})} e^{\mathrm{i}n\phi_{\text{obs}}} \Big],$$

where

$$R_{\text{obs,fil}} = \sqrt{\rho_{\text{obs}}^2 + \rho_{\text{fil}}^2 - 2\rho_{\text{obs}}\rho_{\text{fil}}\cos\phi_{\text{obs}}} \tag{2.1}$$

is the distance between $(\rho_{\text{obs}}, \phi_{\text{obs}})$ and $(\rho_{\text{fil}}, 0)$; hereafter, we will use $R_{A,B}$ to denote the distance from (ρ_A, ϕ_A) to (ρ_B, ϕ_B).

In (2.1) the total field consists of two terms, the first one is the incident field (due to the magnetic filament), and the second one is the scattered field, expressed as a Fourier series.

By employing the large-n approximations of the Bessel and Hankel functions

$$J_n(x) \sim \frac{1}{\sqrt{2\pi n}}\left(\frac{ex}{2n}\right)^n, \quad n \to +\infty \tag{2.2}$$

$$H_n(x) \sim -\mathrm{i}\sqrt{\frac{2}{\pi n}}\left(\frac{ex}{2n}\right)^{-n}, \quad n \to +\infty \tag{2.3}$$

and the corresponding approximations of their derivatives, we find that for large-$|n|$, the n-th term of the scattered magnetic field's series in (2.1) behaves as

$$\frac{1}{\pi \mathrm{i}|n|}\left(\frac{\rho_{\text{cri}}}{\rho_{\text{obs}}}\right)^{|n|} e^{\mathrm{i}|n|\phi_{\text{obs}}},$$

where the critical radius ρ_{cri} is defined by

$$\rho_{\text{cri}} = \rho_{\text{cyl}}^2/\rho_{\text{fil}}. \tag{2.4}$$

This means that the series in (2.1), and hence also the total magnetic field, converge for all $\rho_{\text{obs}} > \rho_{\text{cri}}$ (Region 3 in Fig. 2.1), and diverge for all $\rho_{\text{obs}} < \rho_{\text{cri}}$ (Region 1 in Fig. 2.1). From $\rho_{\text{fil}} > \rho_{\text{cyl}}$, it follows that $\rho_{\text{cri}} < \rho_{\text{cyl}}$, so the solution (2.1) is also convergent inside the PEC until the critical radius $(\rho_{\text{obs}} > \rho_{\text{cri}})$, i.e. Region 2 in Fig. 2.1. Since the derivative of (2.1) can be shown to be also well-defined until the critical radius, we conclude that the extended solution (2.1) for $\rho_{\text{obs}} > \rho_{\text{cri}}$ is the analytic continuation of the exact field inside the PEC.

The total tangential (to the PEC surface) electric-field component is readily derived by means of Ampère's law

$$E_\phi = -\frac{\mathrm{i}}{\omega\epsilon_0}\frac{\partial H_z}{\partial \rho_{\text{obs}}}. \tag{2.5}$$

2.3 Continuous Auxiliary Magnetic Current Density

First, we apply a "Continuous-MAS" approach and consider that the scattered magnetic field is generated by a continuous z-directed magnetic surface current with density $M^s(\phi_{\text{aux}})$, lying on a cylindrical auxiliary surface of radius $\rho_{\text{aux}} < \rho_{\text{cyl}}$. Then, the total magnetic field for $\rho_{\text{obs}} > \rho_{\text{cyl}}$ is expressed by

$$\begin{aligned} H_z = -\frac{\omega\epsilon_0}{4}\Big[& I_M H_0^{(1)}\left(kR_{\text{fil,obs}}\right) \\ & + \rho_{\text{aux}} \int_{-\pi}^{\pi} H_0^{(1)}\left(kR_{\text{aux,obs}}\right) M^s\left(\phi_{\text{aux}}\right) \mathrm{d}\phi_{\text{aux}}\Big], \end{aligned} \tag{2.6}$$

where the first term is the incident and the second the scattered field. Hence, from (2.5), we find

$$E_\phi = -\frac{ik}{4}\Big[I_M \frac{(\rho_{obs} - \rho_{fil}\cos\phi_{obs})H_1^{(1)}(kR_{fil,obs})}{\sqrt{\rho_{obs}^2 + \rho_{fil}^2 - 2\rho_{obs}\rho_{fil}\cos\phi_{obs}}} + \rho_{aux}\int_{-\pi}^{\pi} \frac{\rho_{obs} - \rho_{aux}\cos(\phi_{aux} - \phi_{obs})}{\sqrt{\rho_{obs}^2 + \rho_{aux}^2 - 2\rho_{obs}\rho_{aux}\cos(\phi_{aux} - \phi_{obs})}} \times H_1^{(1)}(kR_{aux,obs})\, M^s(\phi_{aux})\, d\phi_{aux}\Big]. \tag{2.7}$$

Now, by enforcing the boundary condition $E_\phi = 0$ for $(\rho_{obs}, \phi_{obs}) = (\rho_{cyl}, \phi_{cyl})$, we obtain, for $-\pi < \phi_{cyl} < \pi$, the following Fredholm integral equation of the first kind with respect to the unknown density $M^s(\phi_{aux})$

$$\int_{-\pi}^{\pi} K(\phi_{aux} - \phi_{cyl})\, M^s(\phi_{aux})\, d\phi_{aux} = I_M g(\phi_{cyl}), \tag{2.8}$$

where

$$K(\phi_{aux} - \phi_{cyl}) = \frac{(\rho_{cyl} - \rho_{aux}\cos(\phi_{aux} - \phi_{cyl}))H_1^{(1)}(kR_{aux,cyl})}{\sqrt{\rho_{cyl}^2 + \rho_{aux}^2 - 2\rho_{cyl}\rho_{aux}\cos(\phi_{aux} - \phi_{cyl})}} \tag{2.9}$$

is a "periodic difference" kernel, since it is a 2π-periodic function depending only on the angles' difference $\phi_{aux} - \phi_{cyl}$; to see this, recall that

$$R_{aux,cyl} = \sqrt{\rho_{aux}^2 + \rho_{cyl}^2 - 2\rho_{aux}\rho_{cyl}\cos(\phi_{aux} - \phi_{cyl})}.$$

Besides, the RHS of the integral equation (2.8) is given by

$$g(\phi_{cyl}) = -\frac{1}{\rho_{aux}} \frac{(\rho_{cyl} - \rho_{fil}\cos\phi_{cyl})\, H_1^{(1)}(kR_{fil,cyl})}{\sqrt{\rho_{cyl}^2 + \rho_{fil}^2 - 2\rho_{cyl}\rho_{fil}\cos\phi_{cyl}}}, \tag{2.10}$$

which is also a periodic function of ϕ_{cyl}. Equations of this type are solved by using the Fourier series of the kernel and the RHS [20]. Specifically, by expressing $H_0^{(1)}(kR_{aux,cyl})$ and $H_0^{(1)}(kR_{fil,cyl})$ according to the general addition theorem

$$H_0^{(1)}\left(\sqrt{x_1^2 + x_2^2 - 2x_1x_2\cos\theta}\right) = \sum_{n=-\infty}^{\infty} J_n(x_1)\, H_n^{(1)}(x_2)\, e^{in\theta},\ x_1 < x_2, \tag{2.11}$$

and differentiating both sides with respect to ρ_{cyl}, we obtain the solution of the Fredholm equation (2.8) for the continuous auxiliary surface-current density

$$M^s(\phi_{aux}) = -\frac{I_M}{2\pi\rho_{aux}} \sum_{n=-\infty}^{\infty} \frac{J_n'(k\rho_{cyl})\, H_n^{(1)}(k\rho_{fil})}{H_n'^{(1)}(k\rho_{cyl})\, J_n(k\rho_{aux})} e^{in\phi_{aux}}. \tag{2.12}$$

By the large-$|n|$ approximations (2.2) and (2.3), we see that the n-th term of the latter series behaves as $-\left(\frac{\rho_{\text{cri}}}{\rho_{\text{aux}}}\right)^{|n|} e^{\mathrm{i}|n|\phi_{\text{aux}}}$. Hence, the series (2.12) converges for $\rho_{\text{aux}} > \rho_{\text{cri}}$ (i.e. for ρ_{aux} in Region 2 of Fig. 2.1, since $\rho_{\text{aux}} < \rho_{\text{cyl}}$ must also hold) and diverges for $\rho_{\text{aux}} < \rho_{\text{cri}}$ (i.e. for ρ_{aux} in Region 1 of Fig. 2.1). This means that an electric field due to a continuous surface magnetic current density can cancel the incident field only if this density lies *outside* the critical surface; otherwise, there is no convergent density to speak of. This conclusion remains the same for the respective TM problem [20] and is consistent with general theorems stating that the auxiliary surface must enclose all singularities of the analytic continuation of the scattered field in the scatterer's interior for the associated integral equation to be solvable [19], [25]. These singularities are known for many shapes, however not in–general–for any arbitrary shape [26].

It is also worth noting that $M^s(\phi_{\text{aux}})$, given by (2.12), is not well-defined if $J_n(k\rho_{\text{aux}})$ equals to zero for some integer n. These *discrete* values of $k\rho_{\text{aux}}$ correspond to the internal resonances of the auxiliary surface and are discussed in [27]. The phenomenon of internal resonances is different from the one analyzed above concerning the non-solvability of the integral equation (2.8), which occurs for *all* $\rho_{\text{aux}} < \rho_{\text{cri}}$, and is intimately connected to the oscillations of the discrete magnetic currents, which are discussed in the next section.

2.4 Discrete Auxiliary Magnetic Current Filaments

2.4.1 Discrete MAS Linear System

The discrete MAS scheme consists of N magnetic current filaments K_l lying at $(\rho_{\text{aux}}, 2\pi l/N)$, with $l = 0, \ldots, N-1$ and $\rho_{\text{aux}} < \rho_{\text{cyl}}$, as shown in Fig. 2.2. The total magnetic field is expressed as

$$H_z = -\frac{\omega\epsilon_0}{4}\left[I_M H_0^{(1)}(kR_{\text{fil,obs}}) + \sum_{l=0}^{N-1} K_l H_0^{(1)}(kR_{l,\text{obs}})\right], \tag{2.13}$$

where $R_{l,\text{obs}}$ the distance between the l-th filament and the observation point, and the first term is the incident field, (similar to (2.1) and (2.6)), while the second term, approximating the scattered field, is given by a finite sum of cylindrical TE fields due to the magnetic current filaments. The N discrete MAS magnetic currents K_l are determined by approximately satisfying the boundary condition $E_\phi = 0$ at N equispaced collocation points on the PEC surface at $(\rho_{\text{obs}}, \phi_{\text{obs}}) = (\rho_{\text{cyl}}, 2\pi p/N)$, for $p = 0, \ldots, N-1$. The resulting $N \times N$ MAS linear system with respect to the unknown currents K_l is written as

$$\sum_{l=0}^{N-1} B_{p,l} K_l = I_M D_p, \quad p = 0, 1, \ldots, N-1, \tag{2.14}$$

where

$$B_{p,l} = \frac{\rho_{\text{cyl}} - \rho_{\text{aux}} \cos\frac{2\pi(p-l)}{N}}{b_{p,l}} H_1^{(1)}(kb_{p,l}), \tag{2.15}$$

$$D_p = -\frac{\rho_{\text{cyl}} - \rho_{\text{fil}} \cos\frac{2\pi p}{N}}{d_p} H_1^{(1)}(kd_p), \tag{2.16}$$

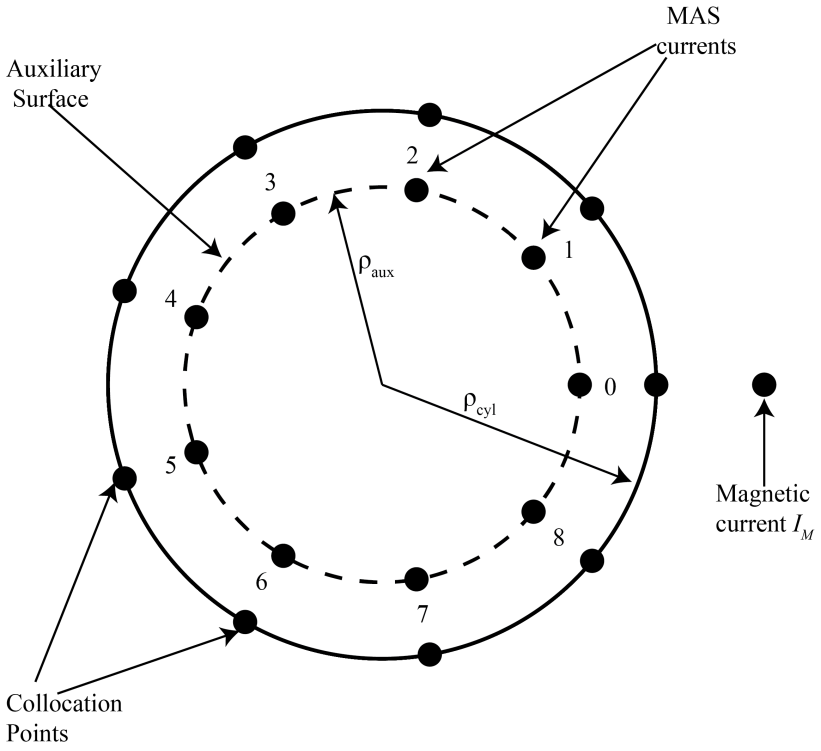

FIGURE 2.2: The discrete MAS scheme for the considered scattering problem with $N = 9$ auxiliary magnetic filaments.

with

$$b_{p,l} = \sqrt{\rho_{\text{aux}}^2 + \rho_{\text{cyl}}^2 - 2\rho_{\text{aux}}\rho_{\text{cyl}} \cos \frac{2\pi(p-l)}{N}} \tag{2.17}$$

the distance between filament l and collocation point p, and

$$d_p = \sqrt{\rho_{\text{fil}}^2 + \rho_{\text{cyl}}^2 - 2\rho_{\text{fil}}\rho_{\text{cyl}} \cos \frac{2\pi p}{N}}. \tag{2.18}$$

the distance between filament I_M and collocation point p.

The MAS system (2.14) is circulant and, hence, it can be solved in closed form by DFTs [20], [28]-[29], yielding

$$K_l = \sum_{m=0}^{N-1} \hat{K}_m e^{\text{i}2\pi lm/N}, \quad l = 0, 1, \ldots, N-1, \tag{2.19}$$

where

$$\hat{K}_m = \frac{I_M}{N} \sum_{p=0}^{N-1} D_p e^{-\frac{\text{i}2\pi pm}{N}} \left[\sum_{l=0}^{N-1} B_l e^{-\frac{\text{i}2\pi l(N-m)}{N}} \right]^{-1}. \tag{2.20}$$

Expressing $H_0^{(1)}(kb_{0,l})$ and $H_0^{(1)}(kd_p)$ by means of (3.21), differentiating with respect to ρ_{cyl}, and using (2.19) and (2.20), we obtain the explicit expression for the N

discrete MAS magnetic currents (for $l = 0, \ldots, N-1$)

$$K_l = \begin{cases} \hat{K}_0 + 2\sum_{m=1}^{\frac{N-1}{2}} \hat{K}_m \cos\frac{2\pi l m}{N}, & N \text{ odd} \\ \hat{K}_0 + (-1)^l \hat{K}_{N/2} + 2\sum_{m=1}^{\frac{N}{2}-1} \hat{K}_m \cos\frac{2\pi l m}{N}, & N \text{ even} \end{cases} \tag{2.21}$$

2.4.2 Large-N Behavior of MAS Currents

For $N \to \infty$, when the angular distance between the large number of MAS filaments becomes vanishingly small, these filaments approximate a continuous surface current density $M^s_{\text{limit}}(\phi_{\text{aux}})$, given by

$$M^s_{\text{limit}}(\phi_{\text{aux}}) = \lim_{N\to\infty} \left(\frac{N K_l}{2\pi\rho_{\text{aux}}} \right), \tag{2.22}$$

where $\phi_{\text{aux}} = 2\pi l/N$. The quantities $NK_l/(2\pi\rho_{\text{aux}})$ will be referred to as *normalized MAS currents*.

The limit in (2.22) can be calculated analytically. For both odd end even N, by (2.20) and (2.21), we find

$$\hat{K}_m \sim -\frac{I_M}{N} \frac{J'_m(k\rho_{\text{cyl}})\, H^{(1)}_m(k\rho_{\text{fil}})}{H'^{(1)}_m(k\rho_{\text{cyl}})\, J_m(k\rho_{\text{aux}})}, \quad N \to \infty. \tag{2.23}$$

By (2.21) and (2.23), we find the limit in (2.22) as

$$M^s_{\text{limit}}(\phi_{\text{aux}}) = -\frac{I_M}{2\pi\rho_{\text{aux}}} \Bigg[\frac{J'_0(k\rho_{\text{cyl}})\, H^{(1)}_0(k\rho_{\text{fil}})}{H'^{(1)}_0(k\rho_{\text{cyl}})\, J_0(k\rho_{\text{aux}})} + 2\sum_{m=1}^{\infty} \frac{J'_m(k\rho_{\text{cyl}})\, H^{(1)}_m(k\rho_{\text{fil}})}{H'^{(1)}_m(k\rho_{\text{cyl}})\, J_m(k\rho_{\text{aux}})} \cos(m\phi_{\text{aux}}) \Bigg]. \tag{2.24}$$

We conclude that $M^s_{\text{limit}}(\phi_{\text{aux}})$ is equal to $M^s(\phi_{\text{aux}})$, given by (2.12); this stems from the fact that the coefficients in the above series are even in m. Thus, $M^s_{\text{limit}}(\phi_{\text{aux}})$ behaves in the same way as the continuous auxiliary surface-current $M^s(\phi_{\text{aux}})$, namely

1. $M^s_{\text{limit}}(\phi_{\text{aux}})$ exists if $\rho_{\text{aux}} > \rho_{\text{cri}}$ (Regions 2 and 3) giving $M^s_{\text{limit}}(\phi_{\text{aux}}) = M^s(\phi_{\text{aux}})$, which cancels the incident electric field on the actual PEC surface, and
2. $M^s_{\text{limit}}(\phi_{\text{aux}})$ diverges if $\rho_{\text{aux}} < \rho_{\text{cri}}$ (Region 1)

2.4.3 Large-N Behavior of MAS Field

Now, we turn our attention to the MAS field, given by (2.13), and investigate it in the limit $N \to \infty$. Employing the addition theorem (3.21) in (2.13), yields

$$H_z^{\text{MAS}} = -\frac{\omega\epsilon_0}{4} \Bigg[I_M H^{(1)}_0(kR_{\text{fil,obs}}) + \sum_{l=0}^{N-1} K_l \sum_{n=-\infty}^{\infty} H^{(1)}_n(k\rho_{\text{obs}})\, J_n(k\rho_{\text{aux}})\, e^{in(\phi_{\text{obs}} - 2\pi l/N)} \Bigg].$$

By using the DFT of K_l, and (2.23), we obtain

$$H_z^{\mathrm{MAS}} \sim -\frac{\omega\epsilon_0 I_M}{4}\Big[H_0^{(1)}\left(kR_{\mathrm{fil,obs}}\right) - \sum_{n=-\infty}^{\infty}\frac{J_n'\left(k\rho_{\mathrm{cyl}}\right)H_n^{(1)}\left(k\rho_{\mathrm{fil}}\right)}{H_n'^{(1)}\left(k\rho_{\mathrm{cyl}}\right)}H_n^{(1)}\left(k\rho_{\mathrm{obs}}\right)e^{in\phi_{\mathrm{obs}}}\Big],\ N\to\infty. \tag{2.25}$$

The approximation in (2.25) is independent of ρ_{aux} and coincides with the exact magnetic field (2.1), which, as elaborated in Section 2.3, converges (diverges) for $\rho_{\mathrm{obs}} > \rho_{\mathrm{cri}}$ $(\rho_{\mathrm{obs}} < \rho_{\mathrm{cri}})$.

Thus, we reach the following conclusions:

1. For $\rho_{\mathrm{cri}} < \rho_{\mathrm{aux}} < \rho_{\mathrm{cyl}}$, the large-$N$ limit of the MAS field H_z^{MAS} gives the exact field solution of the problem in Region 3 ($\rho_{\mathrm{obs}} > \rho_{\mathrm{cyl}}$) as well as its analytic continuation in the part of Region 2 between the auxiliary and the physical surface (namely $\rho_{\mathrm{aux}} < \rho_{\mathrm{obs}} < \rho_{\mathrm{cyl}}$)

2. For $\rho_{\mathrm{aux}} < \rho_{\mathrm{cri}}$, where it was shown in Section 2.4.2 that the MAS currents $NK_l/2\pi\rho_{\mathrm{aux}}$ diverge, the MAS field H_z^{MAS} converges, as $N\to\infty$, to the exact field in Region 3 ($\rho_{\mathrm{obs}} > \rho_{\mathrm{cyl}}$) and its analytic continuation in Region 2 ($\rho_{\mathrm{cri}} < \rho_{\mathrm{obs}} < \rho_{\mathrm{cyl}}$). The limit of H_z^{MAS} does not exist in the part $\rho_{\mathrm{aux}} < \rho_{\mathrm{obs}} < \rho_{\mathrm{cri}}$ of Region 1.

The fact that it is possible for MAS to recover for large-N the exact magnetic field, even when the normalized currents do not converge to a surface current density, is a main result from the above analysis on the discrete MAS and is in accordance with previous works [27], [20] pertaining to the TM case.

2.4.4 Divergent Case: Asymptotic Formula for the MAS Currents

For $\rho_{\mathrm{aux}} < \rho_{\mathrm{cri}}$, we have shown above that the MAS currents diverge as $N\to\infty$. Here, we prove an asymptotic formula for the diverging K_l and show that the divergence appears in the form of oscillations in the real parts of K_l.

By (2.2), (2.3), and (2.23) we obtain $\hat{K}_m \sim \frac{I_M}{N}t^m$, $m\to\infty$, where $t = \frac{\rho_{\mathrm{cri}}}{\rho_{\mathrm{aux}}} > 1$. Thus, since $t > 1$, in the finite sum (2.21) contribute significantly only the large m terms. In this way, we may neglect in (2.21) the terms $m = 0, 1, \ldots, n-1$ and retain only the remaining terms for $m \geq n$, yielding

$$K_l \sim \frac{I_M}{N}\begin{cases} 2\sum\limits_{m=n}^{\frac{N-1}{2}} t^m\cos\frac{2\pi lm}{N},\ N \text{ odd} \\ (-1)^l t^{N/2} + 2\sum\limits_{m=n}^{\frac{N}{2}-1} t^m\cos\frac{2\pi lm}{N},\ N \text{ even}\end{cases}, \tag{2.26}$$

where the final result will be shown to be independent of n.

Closed-form expressions for the summations in (2.26) are feasible with the aid of the exact formula (D8) of [21]. For large Q and $t > 1$, we can omit the n-dependent terms in (2.26), and, obtain, as $N\to\infty$, the asymptotic expression

$$K_l \sim \frac{I_M}{N}\begin{cases} (-1)^l t^{(N+1)/2}\dfrac{2\left(t-1\right)\cos\frac{\pi l}{N}}{t^2 - 2t\cos\frac{2\pi l}{N} + 1},\ N \text{ odd} \\ (-1)^l t^{N/2}\dfrac{t^2-1}{t^2 - 2t\cos\frac{2\pi l}{N} + 1},\ N \text{ even}\end{cases} \tag{2.27}$$

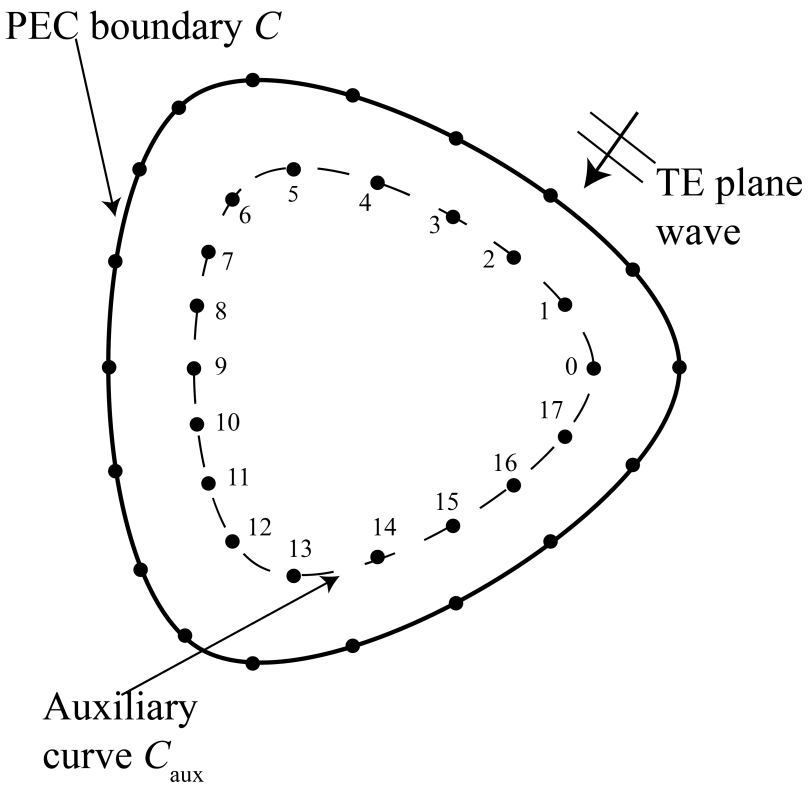

FIGURE 2.3: The discrete MAS scheme with $N = 18$ auxiliary magnetic filaments for the scattering problem by a rounded triangle.

Eq. (2.27) sheds further light in the divergence of the MAS currents presented in Section 2.4.2. The asymptotic approximations are real valued, and, thus, the imaginary parts of the currents are not expected to provide significant effects. The real divergent MAS currents *oscillate* for large N due to the factor $(-1)^l$, appearing in (2.27). Hence, adjacent MAS currents have opposite signs and due to the factor $t^{(N+1)/2}$ (or $t^{N/2}$), their real parts become exponentially large with N.

2.4.5 Discrete MAS for Non-Circular Shapes

Now, we give an example for TE plane-wave scattering by a non-circular cylinder. Particularly, we consider the rounded triangle with PEC boundary C, described in (12) of [26]; see Fig. 2.3. We assume N auxiliary magnetic current filaments of amplitudes K_l $(l = 0, \ldots, N)$, lying on an auxiliary curve C_{aux}. The total z-directed magnetic field is given by

$$H^t(\mathbf{r}) = H^{\text{inc}}(\mathbf{r}) + \sum_{l=0}^{N-1} \widetilde{K}_l H_0^{(1)}(k|\mathbf{r} - \mathbf{r}_l|), \tag{2.28}$$

where $\mathbf{r}_l$ is the position vector of the l-th filament, $\widetilde{K}_l = -(\omega\varepsilon_0/4)\, K_l$, and $H^{\text{inc}}(x, y) = \exp[-ik(x\cos\psi + y\sin\psi)]$ the incident field of angle of incidence ψ. Imposing the PEC condition on N collocation points on C, we get the linear system with respect to the normalized MAS currents $\widetilde{K}_l$

$$\sum_{l=0}^{N-1} \widetilde{K}_l \frac{\partial}{\partial n}\left[H_0^{(1)}\left(k\,|\mathbf{r}_m - \mathbf{r}_l|\right)\right] = -\frac{\partial}{\partial n}[H^{\text{inc}}(\mathbf{r}_m)], \tag{2.29}$$

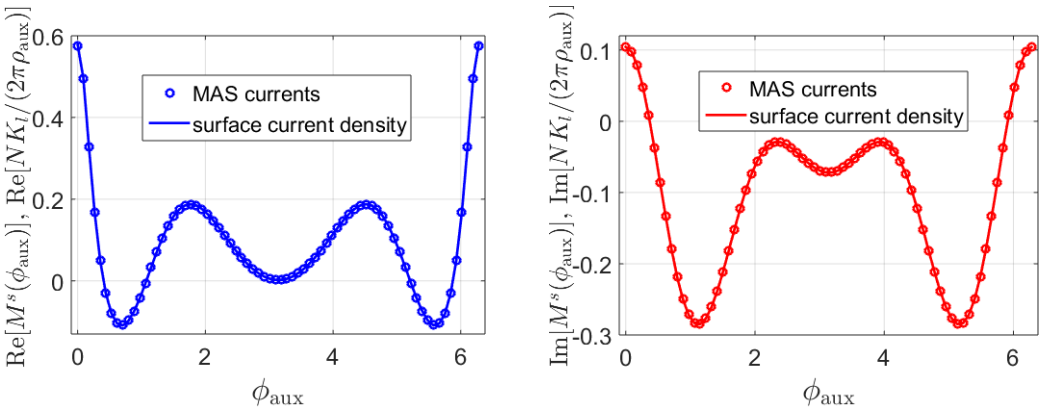

FIGURE 2.4: Real (left panel) and imaginary (right panel) parts of the auxiliary magnetic surface-current density $M^s(\phi_{\mathrm{aux}})$ and the normalized MAS currents $NK_l/(2\pi\rho_{\mathrm{aux}})$ for $k\rho_{\mathrm{cyl}} = 2.1$, $k\rho_{\mathrm{fil}} = 3$, $k\rho_{\mathrm{aux}} = 1.9$, and $N = 71$. The two sets of results coincide at the scale of this figure.

where $\hat{\mathbf{n}}$ is the normal unit vector on C, and $\mathbf{r}_m$ the position vector of the m-th collocation point, for $m = 0, \ldots, N-1$. The involved matrix in the system (2.29) is non-circulant and, hence, this system can only be solved numerically.

2.5 Numerical Results and Discussion

Numerical results are now presented to illustrate the theoretical findings of the previous sections. The results concern comparative variations of

1. the continuous magnetic surface-current density $M^s(\phi_{\mathrm{aux}})$ computed from (2.12) by retaining sufficient number of terms for the series to converge to a desired accuracy

2. the MAS currents K_l, $l = 0, 1, \ldots., N-1$ computed by solving numerically the circulant MAS system (2.14)

3. the exact scattered field H_z^{exact} computed from the series in the RHS of (2.1) by retaining sufficient number of terms

4. the MAS scattered magnetic field H_z^{MAS} computed from the series in the RHS of (2.13) with the MAS currents K_l computed as in 2. above.

We consider a circular cylinder with $k\rho_{\mathrm{cyl}} = 2.1$ illuminated by a magnetic filament at $k\rho_{\mathrm{fil}} = 3$, so that $k\rho_{\mathrm{cri}} = 1.47$.

In Fig. 2.4, we depict the real and imaginary parts of $M^s(\phi_{\mathrm{aux}})$ for $k\rho_{\mathrm{aux}} = 1.9$ and the corresponding normalized MAS currents for $N = 71$. As expected, the two sets of results coincide since here $\rho_{\mathrm{cri}} < \rho_{\mathrm{aux}} < \rho_{\mathrm{cyl}}$, in which case as we have shown in Section 2.4.2, the normalized currents converge to $M^s(\phi_{\mathrm{aux}})$.

In Fig. 2.5, we change only the auxiliary radius to $k\rho_{\mathrm{aux}} = 1.3$. In this case $\rho_{\mathrm{aux}} < \rho_{\mathrm{cri}}$, so, according to Section 2.3, now, there exists no meaningful $M^s(\phi_{\mathrm{aux}})$ to show and subsequently compare it with the normalized MAS currents. Thus, we depict only the MAS currents for $N = 71$. It is seen that the imaginary parts of the currents behave smoothly. However, in stark contrast, the real parts oscillate rapidly between large positive and negative values near $\phi_{\mathrm{aux}} = 0$ and 2π, while each two

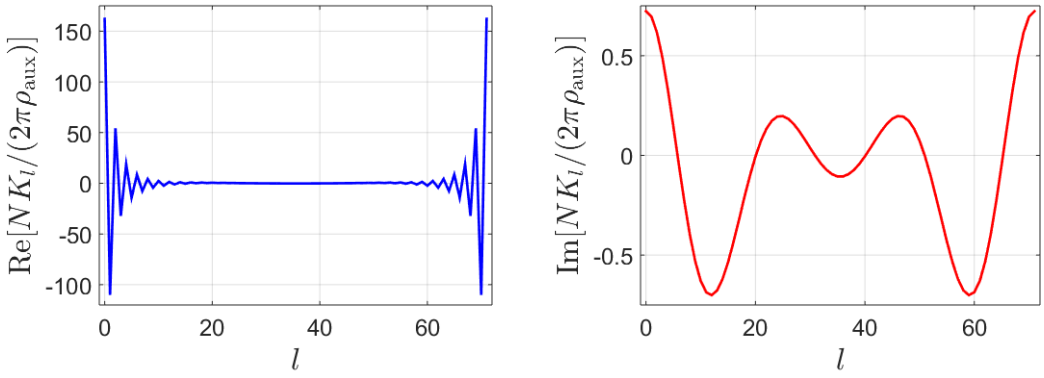

FIGURE 2.5: Real (left panel) and imaginary (rigth panel) parts of normalized MAS currents $NK_l/(2\pi\rho_{\mathrm{aux}})$ versus the source index l. The parameters are the same with Fig. 2.4 except for $k\rho_{\mathrm{aux}} = 1.3$.

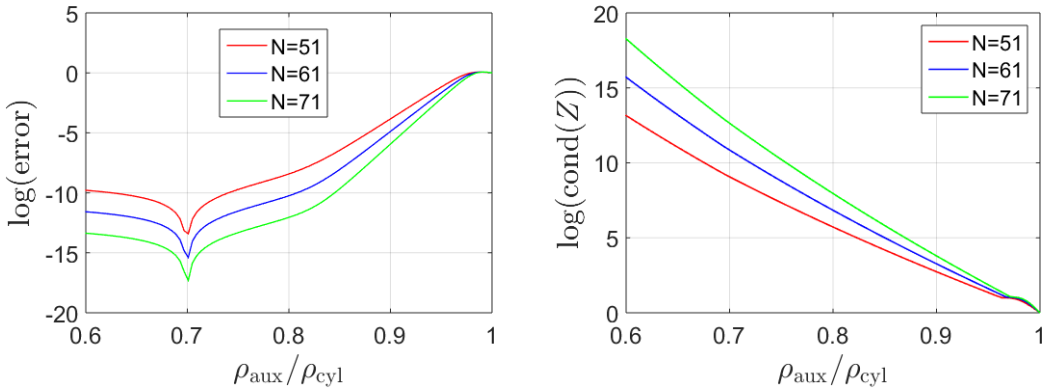

FIGURE 2.6: Boundary condition error (left panel) and matrix condition number (right panel) versus $\rho_{\mathrm{aux}}/\rho_{\mathrm{cyl}}$ for the application of MAS to the circular cylinder (cf. Figs. 2.4 and 2.5) with $N = 51, 61, 71$.

adjacent MAS currents have opposite signs. The peaks of the oscillations increase rapidly with N. This behavior is justified also by the asymptotic formula derived in Section 2.4.4; we will return to this below.

The above results provide the numerical demonstration of the theoretical conclusions of Section 2.4.2 concerning the fact that the MAS currents diverge if $\rho_{\mathrm{aux}} < \rho_{\mathrm{cri}}$. Additionally, we observe here the nature of the appearing oscillations in the divergent case, which are inherent in MAS and are not due to ill-conditioning of the system's matrix. The major differences between the divergence and oscillations phenomena analyzed herein and ill-conditioning effects were thoroughly analyzed in [27], [20], and [26]. In Fig. 2.6, we show the tradeoff between the boundary condition error and the MAS matrix condition number; such a tradeoff is characteristic in MAS [30],[31].

Now, we proceed to investigate the behaviors of the computed magnetic fields. In Fig. 2.7, we depict the curves of H_z^{exact} and H_z^{MAS} for observation at $k\rho_{\mathrm{obs}} = 10$ (Region 3 of Fig. 2.1). The auxiliary radius is $k\rho_{\mathrm{aux}} = 1.3$, hence the MAS currents diverge and oscillate (cf. Fig. 2.5). Nevertheless, the MAS magnetic field H_z^{MAS}, generated due to the divergent and oscillating MAS currents, is the true field since it coincides with the exact field H_z^{exact}. We have made also the corresponding simulations for $k\rho_{\mathrm{obs}}$ lying in Regions 1 and 2 of Fig. 2.1 (not included here for brevity),

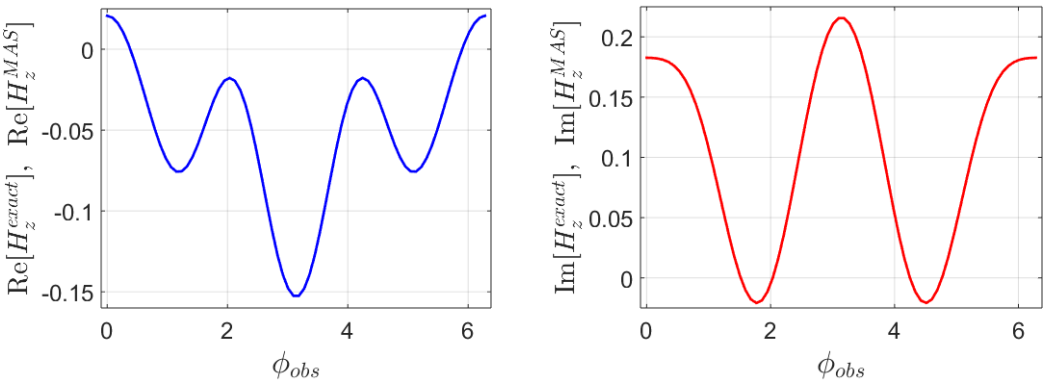

FIGURE 2.7: Real (left panel) and imaginary (right panel) parts of exact scattered field H_z^{exact} and MAS scattered field H_z^{MAS} for $k\rho_{\text{obs}} = 10$. Depicted magnetic fields have been normalized by the factor $(-\omega\epsilon_0/4)$. The two sets of curves coincide at the scale of this figure. The parameters of MAS are $k\rho_{\text{aux}} = 1.3$ and $N = 71$. Thus, H_z^{MAS} is obtained from the divergent and oscillating currents of Fig. 2.5.

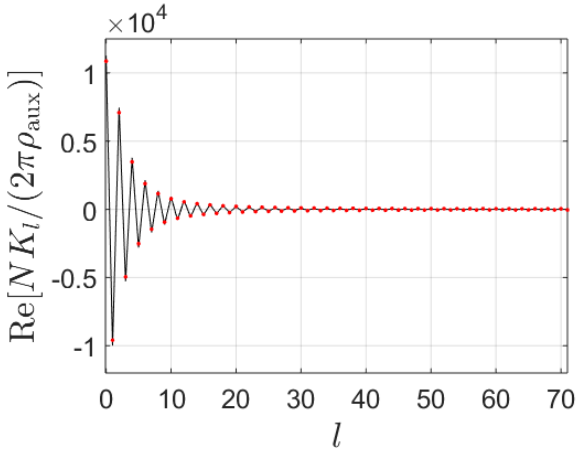

FIGURE 2.8: Real part of the normalized MAS currents $NK_l/(2\pi\rho_{\text{aux}})$ versus the source index l for $k\rho_{\text{aux}} = 1.3$ and $N = 140$. Red dots correspond to the asymptotic formula (2.27), while black straight lines to the numerical solution of the system (2.14). For clarity, we show only results corresponding to $l = 0, 1, \ldots, 71$ (currents for $l > 70$ are symmetric with respect to those for $l < 70$).

and found that the results remain in accordance to the theoretical predictions of Section 2.4.3. Precisely, the MAS field generated in Region 2 by the divergent currents of Fig. 2.5 coincides with the analytic continuation of the exact field in Region 2 inside the cylinder. Besides, the computed MAS magnetic field in Region 1 (where there is no exact field) is found to oscillate, which indicates the divergence of this field in this region, as $N \to \infty$.

In Fig. 2.8, we show numerical results corresponding to the analysis of Section 2.4.4. We compare the MAS currents obtained by the numerical solution of the circulant system (2.14) with the corresponding results obtained from the asymptotic formula (2.27). It is evident that, for large N, the asymptotic formula approximates with very good agreement the numerical solution of the MAS system.

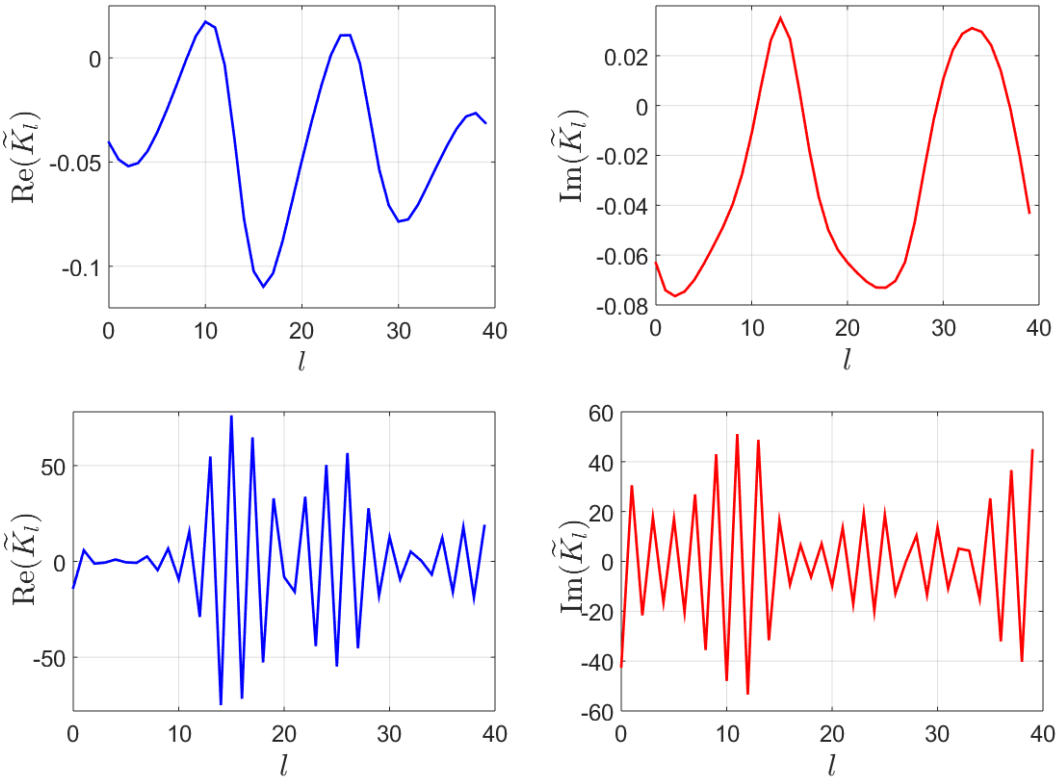

FIGURE 2.9: Real and imaginary parts of the MAS currents $\widetilde{K}_l$ versus the source index l for (a), (b) $\sigma_{\text{aux}} = 0.95$ and (c), (d) $\sigma_{\text{aux}} = 0.60$.

Next, we give numerical results for TE scattering, with $\psi = \pi/6$, by the rounded triangle C of Fig. 2.3. The coordinates of the collocation points on C are

$$x_{\text{cyl}} = 1.75(\cos\varphi_{\text{obs}} + 0.1\cos(2\varphi_{\text{obs}})),$$

$$y_{\text{cyl}} = 1.75(\sin\varphi_{\text{obs}} - 0.1\sin(2\varphi_{\text{obs}})).$$

Auxiliary filaments lie on C_{aux} with

$$(x_{\text{aux}}, y_{\text{aux}}) = \sigma_{\text{aux}}(x_{\text{cyl}}, y_{\text{cyl}}), \quad 0 < \sigma_{\text{aux}} < 1,$$

and observation points on

$$(x_{\text{obs}}, y_{\text{obs}}) = \sigma_{\text{obs}}(x_{\text{cyl}}, y_{\text{cyl}}), \quad \sigma_{\text{obs}} = 2.$$

Fig. 2.9 depicts the MAS currents $\widetilde{K}_l$ for $N = 40$ computed by solving (2.29) for $\sigma_{\text{aux}} = 0.95$ (scattered field's singularities are enclosed by C_{aux}) and $\sigma_{\text{aux}} = 0.60$ (singularities are not enclosed by C_{aux}). For $\sigma_{\text{aux}} = 0.60$, the real and imaginary parts of the MAS currents diverge and oscillate between large values of alternating sign. However, the total magnetic field (2.28) generated by the divergent and oscillating currents is convergent and coincides with the field computed by the Finite Element Method (FEM-COMSOL Multiphysics); see Fig. 2.10. In this case, no exact formulas are available for a comparison.

We now turn to an example that is, potentially, suitable for EMC applications. This corresponds to the scattering configuration of Fig. 2.11, referring to plane-wave incidence on a PEC rounded triangle (like that of Fig. 2.3) coated by a dielectric layer.

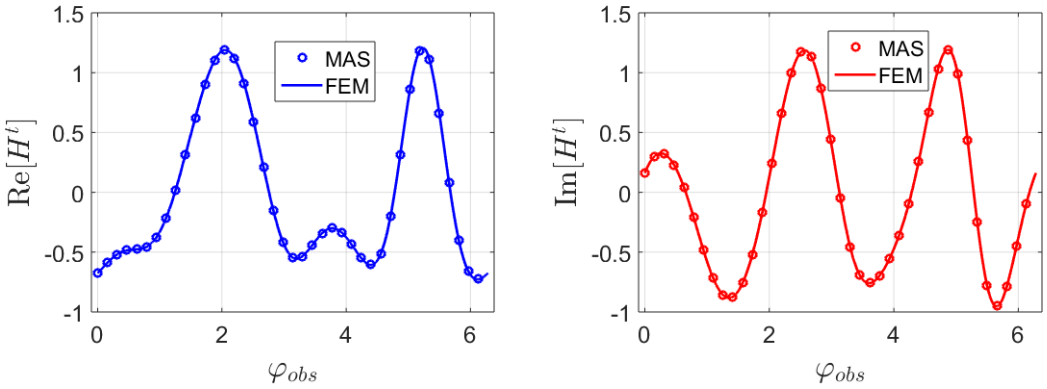

FIGURE 2.10: Real and imaginary parts of the total magnetic field H^t versus the observation angle ϕ_{obs}. For MAS, the values of the diverging MAS currents of Fig. 8c and 8d are used.

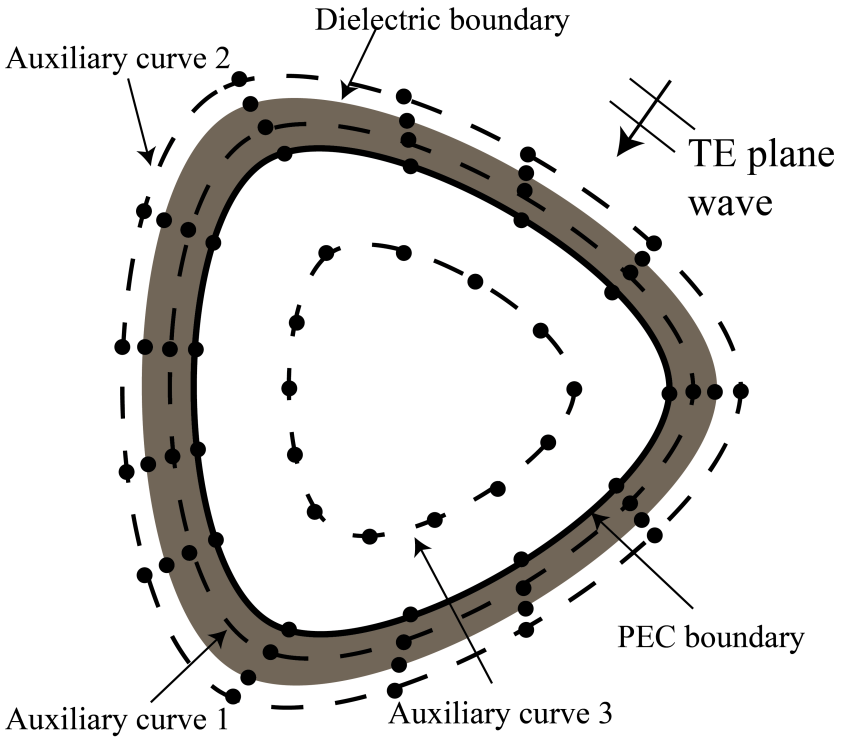

FIGURE 2.11: MAS scheme for the scattering problem of a PEC rounded triangle coated by a dielectric layer of relative permittivity ϵ_r.

The scattered field in the external region can be appropriately controlled by adjusting the permittivity and thickness of the coating layer. The discrete MAS scheme for the numerical solution of the scattering problem now involves three sets of auxiliary sources.

We consider the coated rounded triangle with $\epsilon_r = 3$, air-dielectric interface coordinates $(x_{\text{diel}}, y_{\text{diel}}) = 1.2(x_{\text{cyl}}, y_{\text{cyl}})$ and the same parameters of the PEC as previously. Fig. 2.12 depicts the diverging and oscillating MAS currents $\widetilde{K}_l^1$ of auxiliary curve 1 for $N = 60$ and $\sigma_{\text{aux}}^1 = 0.75$. The magnetic field due to these currents is depicted in Fig. 2.13 and it is convergent and coincides with the one computed by the FEM.

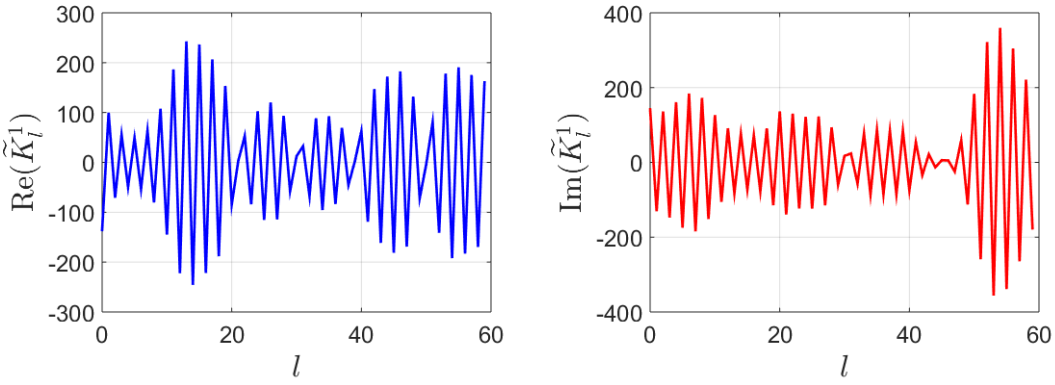

FIGURE 2.12: Real and imaginary parts of the MAS currents $\widetilde{K}_l^1$ of auxiliary curve 1 versus the source index l for $\sigma_{\text{aux}}^1 = 0.75$.

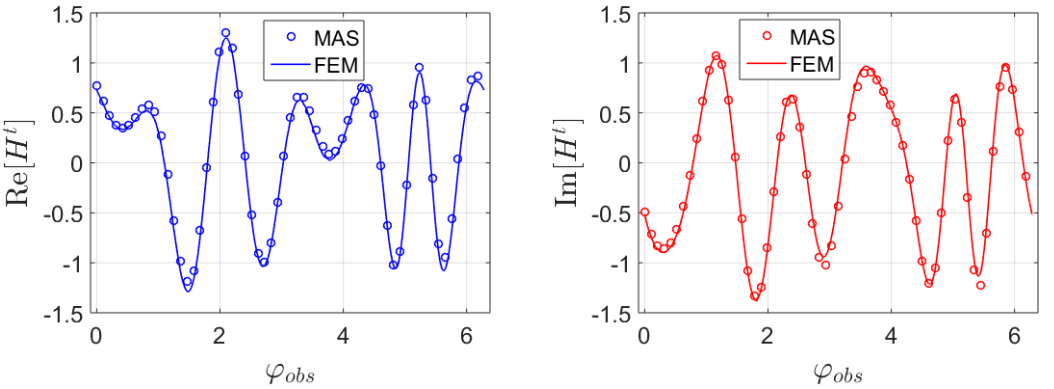

FIGURE 2.13: Real and imaginary parts of the total magnetic field H^t at $\sigma_{obs} = 4$ versus ϕ_{obs}. For MAS, the values of the diverging MAS currents of Fig. 2.12 are used.

2.6 Conclusions

We applied the MAS to the TE scattering problem concerning the excitation of a PEC cylinder by a magnetic filament. It was shown analytically that the MAS magnetic field converges to the true field, even when the MAS currents diverge and oscillate. In this divergent case, an asymptotic formula for large number of auxiliary sources was derived which was demonstrated analytically and also verified numerically that predicts accurately the nature and characteristics of the currents oscillations. It was also demonstrated numerically that the mentioned conclusions carry over to non-circular shapes.

Oscillations in the intermediate quantities involved in the implementation of numerical algorithms (like the currents in the MAS) should–in general–be avoided; this is stressed in classic books on algorithmic design, e.g. in Section 1.18 of [32]. In the context of MAS, since the final quantity (the scattered field) is expected to be small, while the intermediate quantities (the currents) are very large, subtractive cancelation is bound to occur. Hence, increasing the auxiliary-source number N will cause a vast increase in both the currents and the matrix condition number, and, in turn, the computed field will deteriorate rapidly with N. Still, and more importantly, even when the MAS currents diverge and oscillate, the MAS solution is not automatically invalidated. As it has been shown in this work, the MAS field converges in spite of

the divergence and oscillations of the MAS currents.

Future work concerns the systematic analysis of the corresponding phenomena for noncircular shapes. It is further interesting to find MAS solutions, with not-too-rapidly-oscillating MAS currents, in which some numerical instability due to oscillations is outweighed by advantages such as a rapid speed of convergence of the scattered field.

Chapter 3

Mode Analysis by the MAS With an Excitation Source

3.1 Introduction

Predicting accurately the cutoff frequencies above which electromagnetic waves propagate in a waveguide is important in several microwaves and optics applications. These frequencies are referred to as *eigenfrequencies* and the corresponding wavenumbers as *eigenvalues*. The main concern herein is the computation of the eigenvalues of hollow simply- or multiply-connected-domain waveguides with perfect electric conducting (PEC) boundaries. Therefore, no attenuation due to losses in the walls or the filling material is considered.

Specifically, the infinitely long, hollow cylindrical waveguide, with PEC boundaries and axis along the z-axis is considered. The arbitrarily-shaped 2-D cross-section of the waveguide on the xy-plane is denoted by D and its PEC boundary curve by C. With an $e^{-\mathrm{i}\omega t}$ time dependence, where $k = \omega/c = 2\pi f/c$ is the wavenumber, we write the solution to the 3-D homogeneous Helmholtz equation in the form

$$\Psi(x,y,z) = \psi(x,y)e^{\pm \mathrm{i}\beta z},\ (x,y) \in D \subset \mathbb{R}^2,\ z \in \mathbb{R}, \tag{3.1}$$

which is to be satisfied together with a homogeneous boundary condition: Transverse-magnetic (TM_z) modes have $\Psi = E_z$, with Ψ satisfying the Dirichlet condition $\Psi = 0$ on C. For transverse-electric (TE_z) modes, $\Psi = H_z$ satisfies a Neumann boundary condition. The radial wavenumber k_ρ is

$$k_\rho = \sqrt{k^2 - \beta^2}. \tag{3.2}$$

For a propagating mode, k is such that $\beta > 0$. A wave that starts propagating at cutoff corresponds to $\beta = 0$ and $k_\rho = k$. Then, from (3.1), the field Ψ on every cross-section z is exactly the same function $\psi(x,y)$. This is a nonzero (resonant) standing wave that satisfies the 2-D homogeneous Helmholtz equation

$$\nabla^2\psi(x,y) + k_\rho^2\,\psi(x,y) = 0,\ (x,y) \in D \subset \mathbb{R}^2. \tag{3.3}$$

The task of finding the eigenvalues k has thus been reduced to finding the k_ρ for which a resonant standing wave can exist in the cross-section D. From now on, it is assumed that $k_\rho = k$ and the terms eigenvalue and resonance are used interchangeably.

The problem thus formulated can be solved analytically only for simple boundaries C such as a circle or an ellipse. For more complicated geometries, many numerical methods have been developed, both with and without meshing. Some early

methods, proposed in the 1970s, are listed in [33] and [34]. The Finite Element Method (FEM) [35] and Finite Difference Method [36] are established meshing techniques for solving the eigenvalue problem. Certain cross-sections can be treated by conformal-mapping techniques [37]. Integral-equation approaches have been also used extensively. Computing the eigenvalues by solving an integro-differential equation with the Method of Moments (MoM) and a surface integral equation by an iterative technique were proposed in [38] and [39], respectively. The polynomial approximation and superquadric functions in the Rayleigh-Ritz procedure for the computation of the eigenvalues was developed in [40]. The radial basis functions collocation method to analyze the eigenproblem of elliptical waveguides was employed in [41], while radial basis functions combined with the variational principle were used in [42]. For simple shapes, cutoff wavenumbers are determined as the eigenvalue roots of the characteristic modes in [43], [44]. Acoustical mode analysis problems dealing with eigenvalues of vibrating membranes or other mechanical systems have been investigated by the singular boundary element method in [45], and by a collocation approach for the numerical solution of the Helmholtz equation in [46].

In integral-equation methods, the eigenvalue problem is first reformulated as a Fredholm integral equation. Specifically, for TE_z modes, the solution of (3.3) is written as an integral of the z-directed magnetic current density M_z on the PEC boundary C. For TM_z modes, the solution of (3.3) has the integral form

$$E_z(\mathbf{r}) = -\frac{\omega\mu_0}{4}\oint_C J_z\left(\mathbf{r}'\right) H_0^{(1)}\left(k\left|\mathbf{r}-\mathbf{r}'\right|\right) \mathrm{d}l',\ \ \mathbf{r}\in D, \tag{3.4}$$

where J_z is the electric current density on C, $\mathbf{r}' = (x', y')$, $\mathbf{r} = (x, y)$, and $H_0^{(1)}$ is the first-kind and zeroth-order cylindrical Hankel function. The Dirichlet boundary condition yields the following integral equation with respect to J_z

$$\oint_C J_z\left(\mathbf{r}'\right) H_0^{(1)}\left(k\left|\mathbf{r}-\mathbf{r}'\right|\right) \mathrm{d}l' = 0,\ \ \mathbf{r}\in C. \tag{3.5}$$

Since the integration and the physical curve coincide, the latter integral equation is weakly (logarithmically) singular. To avoid this, MAS can be applied according to which, J_z or M_z is replaced by N discrete z-directed current filaments, on a surface enclosing the PEC boundary. For the considered 2-D problem, the sources lie on an auxiliary curve C_{aux}, usually of the same shape as the physical boundary C. Then, the total field is written as a superposition of the fields due to the auxiliary sources

$$E_z(\mathbf{r}) = -\frac{\omega\mu_0}{4}\sum_{l=0}^{N-1} I_l H_0^{(1)}\left(k\left|\mathbf{r}-\mathbf{r}_l\right|\right),\ \ \mathbf{r}\in D, \tag{3.6}$$

where $\mathbf{r}_l$ the position vector of the l-th auxiliary current I_l.

Applying the boundary condition (4) on N collocation points on C yields the following linear system of equations

$$\sum_{l=0}^{N-1} I_l H_0^{(1)}\left(k\left|\mathbf{r}_p-\mathbf{r}_l\right|\right) = 0,\quad p = 0,\ldots,N-1, \tag{3.7}$$

which can be written in matrix form as $[Z(k)]\,\mathbf{I} = \mathbf{0}$. This is a discretized version of the re-formulated Fredholm equation (3.5) (with the integration over the displaced boundary C_{aux}) and has non-trivial solutions only when the impedance matrix $[Z]$ is

singular. Thus its determinant must be equal to zero

$$\det[Z(k)] = 0, \tag{3.8}$$

giving the waveguide eigenvalues. For large matrices, the solution of (3.8) is complicated and time consuming. Furthermore, one is often forced to deal with the much-discussed problem of spurious eigenvalues in the final results; these are undesirable zeros that appear to be eigenvalues, but are not [47]. The eigenvalues can also be computed by the maxima of the condition number of $Z(k)$ [48].

An alternative MAS approach exhibiting beneficial characteristics (in particular, no spurious eigenvalues), was presented in [49]–[51]. This approach adds an excitation source to the equivalent problem. In the present chapter, this source is taken to be an internal or external line source (a z-directed infinitely-long current filament) or (for external excitation only) a plane wave. We will refer to this method as *Method of Auxiliary Sources with an Excitation Source (MAS-ES)*. The determination of the eigenvalues by the MAS-ES is based on measuring the physical response of D to the excitation source. This response is high when D resonates with the source, i.e. when the frequency of the source equals the eigenfrequency of the waveguide, in which case the standing-wave field enforced in D has large amplitude. Therefore, we measure the physical response by defining a k-dependent *response function* $F(k)$, which is the mean-square value of the magnitude of the total field in D. Plotting $F(k)$ for a fine grid of k yields the so-called *response curve*, the peaks of which correspond to the eigenvalues of the waveguide. This approach does not rely on the computation of the determinant (or the condition number) of the impedance matrix and is thus efficient in terms of CPU time. Still, regularization techniques are required to eliminate spurious solutions from the response curve. The MAS-ES was applied in [52] for eigenvalues of simply- and multiply-connected domains and in [53] for periodic eigenvalue problems. Another MAS-related approach treats the PEC cylinder as a lossy cylinder with a finite but large conductivity subject to a a plane wave illumination and computes the peaks of shielding-effectiveness responses. This approach was developed in [54], [55] and tested for waveguides with circular and concentric circular boundaries.

This chapter is a comprehensive presentation and application of a number of variants of MAS-ES. Both external and internal excitation sources are examined. By analysis and examples, we particularly aim to emphasize a number of theoretical and practical aspects that, while fundamental, seem to be insufficiently familiar to workers of the field; this is but one of the novel features of our work. In particular, one of the main objectives is to *demonstrate that when internal excitation is employed no regularization is needed*. This is proved analytically for the circular waveguide and verified numerically for all examined geometries. The need for regularization for an external excitation source is also elaborated analytically and numerically. Additionally, we demonstrate the *divergence of the MAS currents* depending on the relative position between the auxiliary curve and the external or internal source. Such divergence phenomena were investigated in [20], [21], [23], [26], [27], [56], but these works pertain to internal and external scattering; only incidentally do they mention eigenvalue problems.

Section 3.2 gives the mathematical formulation of the developed method, emphasizing that it is based on a homogeneous Helmholtz equation with inhomogeneous boundary conditions. Section 3.3, which pertains to the circular waveguide, demonstrates analytically that regularization techniques are necessary for an external source but not needed for an internal source; this section also gives conditions for

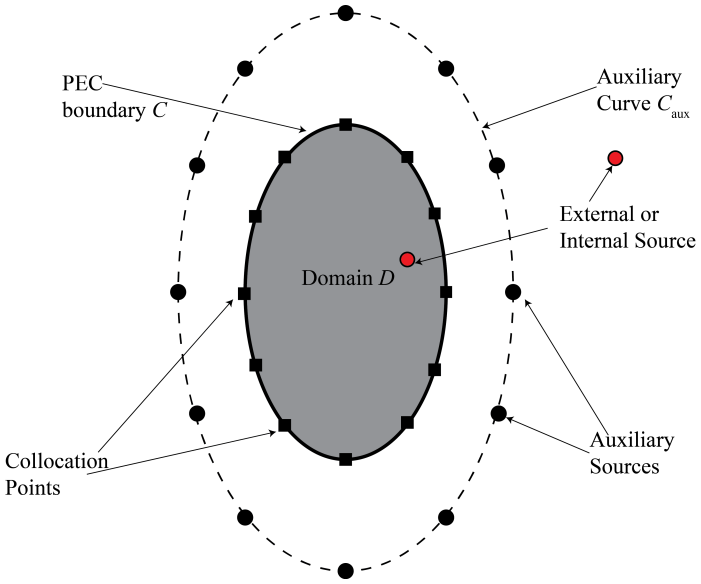

FIGURE 3.1: Geometrical configuration for the mode analysis by MAS-ES for an arbitrarily-shaped simply-connected domain waveguide.

the divergence of the MAS currents, both for an external and an internal excitation source. Section 3.4 contains numerical experiments that test the method; they also confirm that previously derived conclusions pertaining to the circular waveguide continue to hold for more general shapes. Section 3.4 specifically investigates three simply-connected and two multiply-connected domains, computes both TM- and TE-mode eigenvalues, and compares to results obtained by the FEM-based commercial software package COMSOL Multiphysics. Both Sections 4.2 and 3.4 demonstrate that MAS-current divergence appears as oscillations of the current complex amplitudes but, importantly, these may not affect the determination of the eigenvalues.

Ref. [57] distinguishes between "natural modes," which pertain to non-driven and thus homogeneous problems (such as (3.1)–(3.8)), and "eigenmodes," in which there is an excitation. Since MAS-ES does use an excitation, it deals with eigenmodes. The eigenmodes' amplitudes are certainly affected by the position and type of excitation. The positions of the resonant frequencies, however, are unaffected, and remain the same as the natural-mode frequencies.

3.2 MAS with an Excitation Source

3.2.1 Waveguides with Simply-Connected Domains

Consider a hollow waveguide (Fig. 3.1) whose cross section is a simply-connected domain D with a PEC boundary C. Both internal and external excitations are considered, where the internal excitation is a line source in D (note that Reutskiy's term "internal excitation" [50] has a slightly different meaning), and the external excitation is either a line source located in the exterior of D or a plane wave. The scattered field ψ^{sc} satisfies the homogeneous Helmholtz equation in D,

$$(\nabla^2 + k^2)\psi^{sc}(\mathbf{r}, k) = 0, \ \mathbf{r} \in D, \tag{3.9}$$

cf. (3.3). On the PEC boundary C,

$$L[\psi^{sc}(\mathbf{r},k)] = -L[\psi^{inc}(\mathbf{r},k)],\ \mathbf{r}\in C, \tag{3.10}$$

where L is the boundary-condition operator, and where ψ^{inc} is the *incident field*, also referred to as the *excitation field*.

Whereas our internal source is an unambiguous concept, it is worth elaborating on what we called "external source," which bears upon the boundary-value problem via (3.10). Inasmuch as an *interior* boundary-value problem is being solved, the boundary condition (3.10) must be understood to hold on the inner side of C (i.e., the side next to D). Since the PEC wall C is impenetrable, our external source cannot generate a physically meaningful field within D. We thus interpret the external excitation via analytic continuation: Our "external source" generates a field exterior to D. What appears in (3.10) is the analytic continuation of this field.

TM fields have $\psi^{sc} = E_z^{sc}$ and $\psi^{inc} = E_z^{inc}$. The boundary condition (3.10) is of the Dirichlet type (L is the identity operator), so that

$$\psi^{sc}(\mathbf{r},k) = -\psi^{inc}(\mathbf{r},k),\ \mathbf{r}\in C. \tag{3.11}$$

TE fields have $\psi^{sc} = H_z^{sc}$ and $\psi^{inc} = H_z^{inc}$. Here, (3.10) is of the Neumann type and L is the normal-derivative operator,

$$\frac{\partial\psi^{sc}(\mathbf{r},k)}{\partial n} = -\frac{\partial\psi^{inc}(\mathbf{r},k)}{\partial n},\ \mathbf{r}\in C. \tag{3.12}$$

Our line-source excitations have the form

$$\psi^{inc}(\mathbf{r},k) = \tilde{I}H_0^{(1)}\left(k|\mathbf{r}-\mathbf{r}_{fil}|\right), \tag{3.13}$$

where $\mathbf{r}_{fil}$ is the (internal or external) location, $\tilde{I}$ is the normalized amplitude, which is $\tilde{I} = (-\omega\mu_0/4)\,I$ for TM fields and $\tilde{I} = (-\omega\epsilon_0/4)\,I_M$ for TE fields, where I and I_M are electric and magnetic currents. Note that $\tilde{I}$ depends on ω and thus on k. A plane-wave excitation is given by

$$\psi^{inc}(\mathbf{r},k) = \tilde{I}e^{-\mathrm{i}k(x\cos\phi+y\sin\phi)}, \tag{3.14}$$

where ϕ is the incidence angle measured counterclockwise from the positive x-axis.

Excitations that possess obvious symmetries must be avoided, as they are likely to miss resonances. For the circular problem, for example, a line source placed at the origin can only excite resonances whose fields are circularly symmetric.

According to the standard MAS scheme, the scattered field ψ^{sc} in D is generated by N auxiliary sources lying on an auxiliary curve C_{aux} enclosing the physical boundary C cf. Fig. 3.1. Hence ψ^{sc} is

$$\psi^{sc}(\mathbf{r},k) = \sum_{l=0}^{N-1}\tilde{I}_l H_0^{(1)}\left(k\,|\mathbf{r}-\mathbf{r}_l|\right),\ \mathbf{r}\in D, \tag{3.15}$$

where $\mathbf{r}_l$ is the position vector on C_{aux} and $\tilde{I}_l$ is the current of the l-th auxiliary source, normalized in the same way as $\tilde{I}$. Imposing the boundary condition (3.10) on N

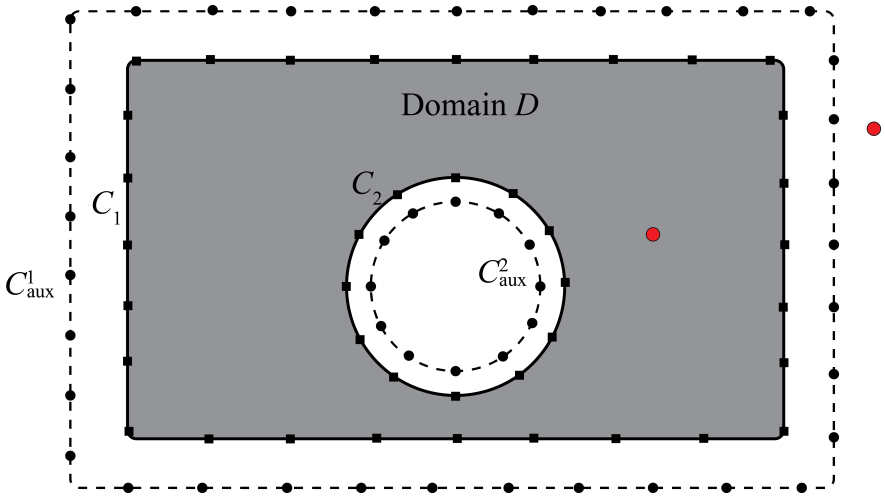

FIGURE 3.2: Like Fig. 3.1, but for a doubly-connected domain waveguide.

collocation points on C leads to a system of equations satisfied by the $\tilde{I}_l$, viz.,

$$\sum_{l=0}^{N-1} \tilde{I}_l L[H_0^{(1)}(k\,|\mathbf{r}_m - \mathbf{r}_l|)] = -L[\psi^{inc}(\mathbf{r}_m, k)],$$
$$m = 0, 1, \ldots, N-1, \tag{3.16}$$

where $\mathbf{r}_m$ is the position vector of the m-th collocation point.

To find the waveguide's eigenvalues k, the response function $F(k)$ of [49]–[51] is used. This is

$$F(k) = \sqrt{\sum_{n=1}^{N_t} \frac{|\psi^t(\mathbf{r}_n, k)|^2}{N_t}}, \tag{3.17}$$

where $\psi^t = \psi^{sc} + \psi^{inc}$ is the *total* field and $\mathbf{r}_n$ are the position vectors of N_t randomly selected sample points in D. The response function $F(k)$ is maximized when a resonant standing wave is formed in D due to the large magnitude of the total field at many points $\mathbf{r}_n$. The random selection of the points reduces the probability of selecting node positions of the standing wave (i.e., zero-field points) that would yield small values of $F(k)$.

3.2.2 Algorithm

For a given k and a given $\mathbf{r}$, the scheme thus consists of solving (3.16) for $\tilde{I}_l$ and then computing ψ^t via $\psi^t = \psi^{sc} + \psi^{inc}$, (3.15), and (3.13) or (3.14). Doing this for all randomly selected $\mathbf{r} = \mathbf{r}_n$ allows computation of $F(k)$ via (3.17). Finally, a plot of $F(k)$ versus k yields the response curve whose peaks are the eigenvalues. The exact locations of the peaks are actually determined by the MATLAB function *findpeaks*. The determination is performed quickly without affecting significantly the total computation time.

3.2.3 Waveguides with Multiply-Connected Domains

The methodology of Section 3.2.1 is easily extended to multiply-connected domains. In the doubly-connected domain of Fig. 3.2, for example, the unknown scattered

field ψ^{sc} must also satisfy a boundary condition on the internal PEC boundary curve C_2. The application of MAS thus involves two sets of auxiliary sources, one on an external auxiliary curve C^1_{aux} (as for the simply-connected region) and a second one on an internal curve C^2_{aux} enclosed by the internal boundary of D. Imposing the boundary conditions yields the linear system

$$\sum_{l=0}^{N_1+N_2-1} \tilde{I}_l L[H_0^{(1)}(k\,|\mathbf{r}_m - \mathbf{r}_l|)] = -L[\psi^{inc}(\mathbf{r}_m, k)],$$
$$m = 0, 1, \ldots, N_1 + N_2 - 1, \tag{3.18}$$

where N_1 and N_2 are the numbers of auxiliary sources on the external and internal auxiliary curves, respectively.

3.3 The circular problem and its implications

Perhaps the simplest waveguide problem is the circular waveguide of radius ρ_{cyl}. Here, the TM eigenvalues are known to be all k that satisfy

$$J_n(k\rho_{\text{cyl}}) = 0, \quad n = 0, 1, 2, \ldots. \tag{3.19}$$

The present section studies the application of MAS-ES to this problem. All variants of MAS-ES must lead to (3.19), but it is not our purpose to re-discover a solution known beforehand. Rather, we discuss *how* each variant arrives at (3.19). This is done because (as will be shown numerically in Section 3.4) the obtained conclusions hold in more general cases.

Both internal ($\rho_{\text{fil}} < \rho_{\text{cyl}}$) and external ($\rho_{\text{cyl}} < \rho_{\text{fil}}$) excitations are considered, where $(\rho_{\text{fil}}, 0)$ are the polar coordinates of the line source I (Fig. 3.3). In both cases, the total field ψ^t in D (i.e. the field E_z^t of the TM modes) is $\psi^t = \psi^{inc} + \psi^{sc}$, where

$$\psi^{inc} = AH_0^{(1)}(kR_{\text{fil,obs}}),\ \rho_{\text{obs}} < \rho_{\text{cyl}}, \tag{3.20}$$

where $A = \frac{-k^2 I}{4\omega\epsilon_0}$ and $R_{\text{fil,obs}}$ is the distance between the source and observation points. In the external case, (3.20) is only meaningful as the analytic continuation discussed in Section 3.2.

Our main tool is, of course, Fourier series. Functions such as the ψ^{inc} of (3.20) can be expanded using the addition theorem

$$H_0^{(1)}\left(\sqrt{x_1^2 + x_2^2 - 2x_1x_2\cos\theta}\right) = \sum_{n=-\infty}^{\infty} J_n(x_1)\, H_n^{(1)}(x_2)\, e^{in\theta},\ 0 < x_1 < x_2. \tag{3.21}$$

Also used are the usual large-order asymptotic approximations to the Bessel and Hankel functions,

$$J_n(x) \sim \frac{1}{\sqrt{2\pi n}}\left(\frac{ex}{2n}\right)^n,\ n \to +\infty, \tag{3.22}$$

$$H_n^{(1)}(x) \sim -\mathrm{i}\sqrt{\frac{2}{\pi n}}\left(\frac{ex}{2n}\right)^{-n},\ n \to +\infty. \tag{3.23}$$

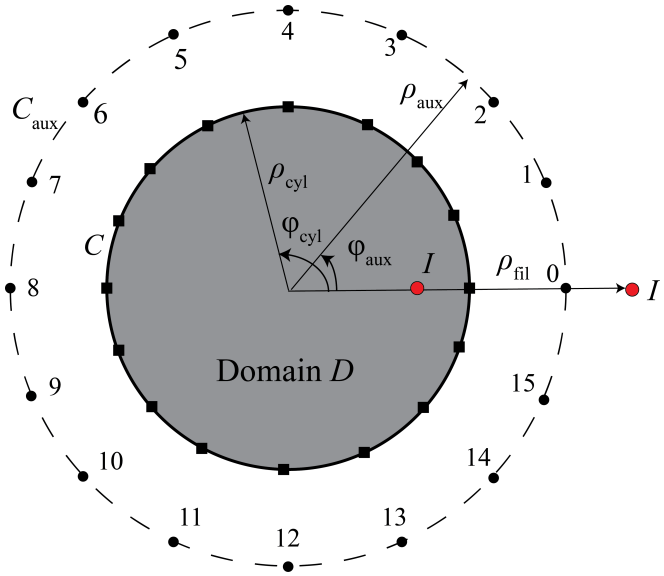

FIGURE 3.3: Application of MAS-ES for a circular waveguide subject to an external or internal line-source excitation.

3.3.1 Exact solutions for internal and external excitations

Let us solve the relevant interior boundary-value problem. The scattered field ψ^{sc} is the general solution of (3.9) that remains finite at the origin. Separation of variables gives

$$\psi^{sc} = A \sum_{n=-\infty}^{\infty} a_n J_n\left(k\rho_{\text{obs}}\right) e^{in\phi_{\text{obs}}},\ \rho_{\text{obs}} < \rho_{\text{cyl}}. \tag{3.24}$$

The a_n are such that the boundary condition (3.10) is satisfied. To find a_n, set $(\rho_{\text{obs}}, \phi_{\text{obs}}) = (\rho_{\text{cyl}}, \phi_{\text{cyl}})$ in (3.20) and then use the addition theorem (3.21) to expand ψ^{inc} into a Fourier series. This yields different series for external and internal excitations:

$$\psi^{inc}\Big|_{\text{PEC}} = \begin{cases} A \sum_n J_n\left(k\rho_{\text{cyl}}\right) H_n^{(1)}\left(k\rho_{\text{fil}}\right) e^{in\phi_{\text{cyl}}},\ \rho_{\text{cyl}} < \rho_{\text{fil}}, \\ A \sum_n J_n\left(k\rho_{\text{fil}}\right) H_n^{(1)}\left(k\rho_{\text{cyl}}\right) e^{in\phi_{\text{cyl}}},\ \rho_{\text{fil}} < \rho_{\text{cyl}}. \end{cases} \tag{3.25}$$

Set $(\rho_{\text{obs}}, \phi_{\text{obs}}) = (\rho_{\text{cyl}}, \phi_{\text{cyl}})$ in (3.24) and apply (3.10) to get

$$a_n = \begin{cases} -H_n^{(1)}\left(k\rho_{\text{fil}}\right),\ \rho_{\text{cyl}} < \rho_{\text{fil}}, \\ -J_n\left(k\rho_{\text{fil}}\right) H_n^{(1)}\left(k\rho_{\text{cyl}}\right) / J_n\left(k\rho_{\text{cyl}}\right),\ \rho_{\text{fil}} < \rho_{\text{cyl}}. \end{cases} \tag{3.26}$$

The interior scattered field is thus given, analytically, by (3.24) and (3.26).

3.3.2 Regularizations for external excitation

External excitations ($\rho_{\text{cyl}} < \rho_{\text{fil}}$) are considered first. In [49]–[51], Reutskiy stresses that the values of the response function $F(k)$ might be too small even in resonance conditions, resulting in response curves without easily distinguishable sharp peaks, hindering the accurate computation of the eigenvalues, and necessitating regularization. Our analytical expressions provide simple explanations for all these findings: By (3.20), (3.24), and the top expression in (3.26), the *total* field $\psi^t = \psi^{inc} + \psi^{sc}$ is zero. Note that the result $\psi^t = 0$ is *physically* correct (no external field penetrates the PEC

waveguide), despite our understanding of the nonzero "incident field" (in D) only in the sense of analytic continuation.[1]

The derivation of the top expression in (3.26) involved cancellation of a factor $J_n(k\rho_{\text{cyl}})$. Slight but judicious changes can negate this cancellation, resulting in a nonzero total field. Such are the two remedies proposed by Reutskiy:

Shift-k regularization technique

The wavenumber k of the incident field in (3.20) and (3.25) is changed to $\tilde{k} = k + \Delta k$ [49]–[51]. In place of the top expression (3.26), one obtains

$$a_n = -\frac{H_n^{(1)}\left(\tilde{k}\rho_{\text{fil}}\right) J_n\left(\tilde{k}\rho_{\text{cyl}}\right)}{J_n\left(k\rho_{\text{cyl}}\right)},\ \rho_{\text{cyl}} < \rho_{\text{fil}}. \tag{3.27}$$

The total field is now generally nonzero,

$$\psi^t = A\sum_{n=-\infty}^{\infty}\left[H_n^{(1)}\left(\tilde{k}\rho_{\text{fil}}\right) J_n\left(\tilde{k}\rho_{\text{obs}}\right) - \frac{H_n^{(1)}\left(\tilde{k}\rho_{\text{fil}}\right) J_n\left(\tilde{k}\rho_{\text{cyl}}\right)}{J_n\left(k\rho_{\text{cyl}}\right)} J_n\left(k\rho_{\text{obs}}\right)\right] \times e^{in\phi_{\text{obs}}}. \tag{3.28}$$

Furthermore, at resonance this total field becomes infinite, as one can see from (3.19) and the denominator of the second term. This is why $F(k)$ exhibits highly visible peaks.

Friction regularization technique

Here, the k in the left-hand side of the Helmholtz equation is modified to $k + i\varepsilon k$, where ε is small and positive [49]–[51]. Physically, this yields a slightly dissipated scattered field, leaving the incident field unaltered. In this case, one finds

$$a_n = -\frac{H_n^{(1)}\left(k\rho_{\text{fil}}\right) J_n\left(k\rho_{\text{cyl}}\right)}{J_n\left(\left(k + i\varepsilon k\right)\rho_{\text{cyl}}\right)},\ \rho_{\text{cyl}} < \rho_{\text{fil}}, \tag{3.29}$$

giving the nonzero total field

$$\psi^t = A\sum_{n=-\infty}^{\infty}\left[H_n^{(1)}\left(k\rho_{\text{fil}}\right) J_n\left(k\rho_{\text{obs}}\right) - \frac{H_n^{(1)}\left(k\rho_{\text{fil}}\right) J_n\left(k\rho_{\text{cyl}}\right)}{J_n\left(\left(k + i\varepsilon k\right)\rho_{\text{cyl}}\right)} J_n\left(\left(k + i\varepsilon k\right)\rho_{\text{obs}}\right)\right] e^{in\phi_{\text{obs}}}. \tag{3.30}$$

For k equal to an eigenvalue and for proper small ε, the denominator of the second term becomes small, resulting in a total field that is large.

[1] More generally, analytic continuation plays an important role in the study of computational methods that involve displaced boundaries, examples being MAS/MFS and the Extended Integral Equation (EIE) [15], [56].

3.3.3 Internal excitation: No regularization is needed

Now consider internal excitations, so that $\rho_{\text{fil}} < \rho_{\text{cyl}}$. By (3.20), (3.24), and the bottom expression in (3.26), the total field ψ^t is

$$\psi^t = \psi^{inc} + \psi^{sc} = \\ A\left[H_0^{(1)}\left(kR_{\text{fil,obs}}\right) - \sum_{n=-\infty}^{\infty} \frac{J_n\left(k\rho_{\text{fil}}\right) H_n^{(1)}\left(k\rho_{\text{cyl}}\right)}{J_n\left(k\rho_{\text{cyl}}\right)} J_n\left(k\rho_{\text{obs}}\right) e^{in\phi_{\text{obs}}}\right], \tag{3.31}$$

which is generally nonzero, and—due to (3.19) and the denominator of the second (scattered) term—infinite at the eigenvalues. The very different nature of this ψ^t (compared to the case of external excitations, where we found $\psi^t = 0$) means that the response curves will have highly visible peaks *without applying any regularization technique*.

3.3.4 Divergence and oscillations of MAS currents

In the context of MFS/MAS, the phenomenon of auxiliary-source divergence and oscillations has been studied for many years [20], [21] and is by now well-established, even for non-circular shapes [26], [27]. Nonetheless, the phenomenon often goes unmentioned, even in works aiming to discuss the convergence of MFS/MAS; an example is the recent review paper [15]. Here, by means of the circular TM problem, we briefly describe the phenomenon within the context of MAS-ES.

Whether for internal or external excitations, the $N \times N$ system (3.16) takes the form

$$\sum_{l=0}^{N-1} I_l H_0^{(1)}\left(kb_{p,l}\right) = -IH_0^{(1)}\left(kd_p\right), \; p = 0, \ldots, N-1, \tag{3.32}$$

where $b_{p,l}$ (d_p) is the distance between collocation point p and the MAS current I_l (the primary current I), viz.,

$$b_{p,l} = \sqrt{\rho_{\text{aux}}^2 + \rho_{\text{cyl}}^2 - 2\rho_{\text{aux}}\rho_{\text{cyl}} \cos\frac{2\pi(p-l)}{N}}, \tag{3.33}$$

$$d_p = \sqrt{\rho_{\text{fil}}^2 + \rho_{\text{cyl}}^2 - 2\rho_{\text{fil}}\rho_{\text{cyl}} \cos\frac{2\pi p}{N}}. \tag{3.34}$$

In what follows, the key ideas are three: (i) The system (3.32) is circulant, so that its (exact) solution can be found in closed form using the methodology of Appendix B of [20]. (ii) The aforementioned closed-form solution is amenable to a large-N asymptotic study. (iii) If the large-N limit of the normalized MAS currents exists and is a finite surface-current density $J_{\text{limit}}^s\left(\phi_{\text{aux}}\right)$, the MAS currents converge. Otherwise, they diverge. Internal and external excitations are examined separately.

Internal excitation The case $\rho_{\text{fil}} < \rho_{\text{cyl}}$ is fully analyzed in [56]. By eqn. (24) of [56],

$$J_{\text{limit}}^s\left(\phi_{\text{aux}}\right) = \\ -\frac{I}{2\pi\rho_{\text{aux}}} \sum_{n=-\infty}^{\infty} \frac{J_n\left(k\rho_{\text{fil}}\right) H_n^{(1)}\left(k\rho_{\text{cyl}}\right)}{H_n{}^{(1)}\left(k\rho_{\text{aux}}\right) J_n\left(k\rho_{\text{cyl}}\right)} e^{in\phi_{\text{aux}}}. \tag{3.35}$$

Eqns. (3.22) and (3.23) show that the n-th term of the series in (3.35) behaves as $(\rho_{\text{aux}}/\rho_{\text{cri}})^n$ as $n \to +\infty$, where the critical radius ρ_{cri} is defined by

$$\rho_{\text{cri}} = \rho_{\text{cyl}}^2/\rho_{\text{fil}}. \tag{3.36}$$

Therefore, the series in (3.35) diverges for $\rho_{\text{aux}} > \rho_{\text{cri}}$, and so do the MAS currents. Ref. [56] further shows that this divergence manifests itself as rapid oscillations in the MAS currents; in fact, the oscillations are shown to be exponentially large in N.

External excitation For $\rho_{\text{cyl}} < \rho_{\text{fil}}$, a similar analysis (details omitted for brevity) shows that

$$J^s_{\text{limit}}(\phi_{\text{aux}}) = -\frac{I}{2\pi\rho_{\text{aux}}} \sum_{n=-\infty}^{\infty} \frac{H_n^{(1)}(k\rho_{\text{fil}})}{H_n^{(1)}(k\rho_{\text{aux}})} e^{in\phi_{\text{aux}}}. \tag{3.37}$$

In this case, (3.23) shows that the n-th term of the series in (3.37) behaves as $(\rho_{\text{aux}}/\rho_{\text{fil}})^n$ as $n \to +\infty$. This means that the MAS currents converge for $\rho_{\text{aux}} < \rho_{\text{fil}}$, but diverge otherwise.[2]

3.3.5 MAS fields, response curves, and eigenvalues: Convergence

Theoretically, one obtains convergent and correct MAS fields even when the MAS currents diverge and oscillate. To the best of our knowledge, this rather peculiar result was first established—within the context of the circular external TM scattering problem—in [20]. This was done by showing that the large-N limit of the MAS field exists and equals the true field, even when the MAS currents diverge.

Following the procedure outlined above, we showed that the true field (for which we found closed-form expressions in Section 3.3.1) is correctly obtained in all of the divergent cases previously analyzed.

For MAS-ES, this means that one can—in theory—correctly obtain waveguide eigenvalues in all cases where the MAS currents diverge. In practice, however, one should take care to avoid *extreme* divergences (i.e., very substantial oscillations) because the large intermediate values (i.e., the large MAS currents) may *numerically* affect the sought-after final values (i.e. the field in D and therefore the associated $F(k)$ and the resulting eigenvalues). It actually seems that mild oscillations might be advantageous in some cases, as discussed in Section 5.5 of [27].

3.3.6 Extensions; more complicated geometries

This section is concluded with a list of some ramifications of the conclusions arrived at via the circular problem. This is done because—as will be established via numerical results in Section 3.4—the basic conclusions remain true for more complicated problems, in which little is known beforehand.

Since the internal-source variant of MAS-ES requires no regularization (Section 3.3.3), it may be preferable to the external-source variant. However, when randomly selecting the measurement points and calculating $F(k)$, one should take care to exclude a small area around the internal source. This is because $F(k)$ involves the total field; thus, the large values near the source might give rise to spurious resonances.

[2] These results have all been extended to the TE case: When $\rho_{\text{fil}} < \rho_{\text{cyl}}$, the equation corresponding to (3.35) is different, but the series continues to diverge when $\rho_{\text{aux}} > \rho_{\text{cri}}$. Eqn. (3.37) holds unaltered. Consequently, the conclusions regarding divergence/convergence are exactly the same as in the TM case.

When using a line current as an *external* source, it is obvious how to avoid oscillations when one wishes to do so: The divergence condition $\rho_{\text{aux}} > \rho_{\text{fil}}$ (for the circular problem, as discussed in Section 3.3.4) simply means that *the exciting line source should lie to the exterior of the auxiliary curve.* For *internal* excitations, however, the divergence condition for the circular problem involves the critical point $(\rho_{\text{cri}}, 0)$. For noncircular geometries, the critical points are the set of singularities of the analytic continuation of the internal scattered field to the exterior of the PEC cavity [56]. Since these are usually not known beforehand, *there seems to be no a priori method of avoiding oscillations.*

For noncircular geometries, numerical results indicating the correctness of MAS fields obtained from oscillating MAS currents can be found in [26], where correctness is established by comparing to independent methods.

3.4 Numerical Results

This section presents numerical results for simply-connected waveguides of circular, elliptical, and rounded-triangular cross sections; and multiply-connected, concentric waveguides with annular-circular and annular-elliptical domains. For each examined waveguide, TM- and TE-mode eigenvalues are computed via MAS-ES. External and internal excitation sources are considered for all cases, with the numerical results presented interchangeably. Unless stated otherwise, we plot the dimensionless function $F_d(k) = F(k)/F(k_0)$ where k_0 is a reference wavenumber that is not close to the resonant wavenumbers. In accordance with Section 3.3.2, a regularization technique is applied for external problems, but no such technique for internal problems.

Results are compared to corresponding ones obtained from the commercial software COMSOL Multiphysics, which solves the eigenvalue problem with the Finite Element Method (FEM) (Comsol Multiphysics). Moreover, for both circular and noncircular problems, we show MAS currents that oscillate. When doing so, however, we choose parameters such that the computed fields, the corresponding response curve, and the resulting eigenvalues, are unaffected, as discussed in Sections 3.3.5 and 3.3.6 .

The collocation points were, in all cases, angularly equispaced (we investigated random distributions of collocation points, but the results were poor). The numbers of collocation points/auxiliary sources, measurement points, and plot points are denoted by N, N_t, and N_g, respectively. Increasing N or N_t above certain thresholds, does not affect significantly the results, but generally gives larger values of the response function $F_d(k)$ and hence sharper peaks in the response curve (the computational time, of course, increases). Increasing N_g yields more accurate eigenvalues k, yet again boosts the computational time. In all the examined cases, $N = 40$, $N_t = 20$, and $N_g = 2000$ were considered; these values yield satisfactory accuracy. Indicatively, for the circular waveguide, when $N > 18$, $N_t > 5$, and $N_g > 500$, no significant changes in the eigenvalues' computations are observed. Besides, whenever a regularization procedure was employed, it was found that the values Δk and ε (see Section 3.3.2) do affect the values of $F_d(k)$. In fact, larger values of Δk and ε generally give larger and smaller values of $F_d(k)$, respectively.

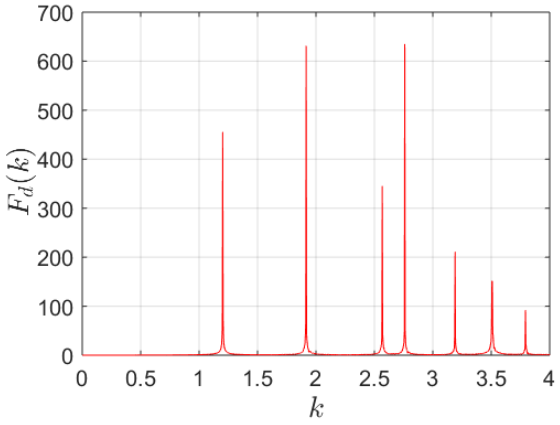

FIGURE 3.4: Response curve for the TM-mode eigenvalues of a circular waveguide with $\rho_{\text{cyl}} = 2$ as obtained using an external excitation line source and the friction regularization technique with $\varepsilon = 10^{-4}$.

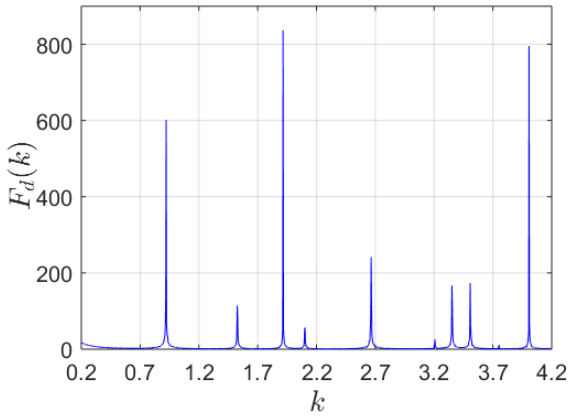

FIGURE 3.5: As in Fig. 3.4, but for TE modes and using an internal line source without a regularization method.

3.4.1 Simply-Connected Domains

Circular Waveguide Consider a circular waveguide with a PEC boundary of radius $\rho_{\text{cyl}} = 2$ (Fig. 3.3). The TM- and TE-mode eigenvalues are the roots of $J_n(k\rho_{\text{cyl}})$ and $J_n'(k\rho_{\text{cyl}})$, respectively.

For the TM-mode eigenvalues, we use an external excitation line source at $\rho_{\text{fil}} = 4$ and an auxiliary curve radius $\rho_{\text{aux}} = 3$. For a smooth response curve we employ the friction regularization technique with $\varepsilon = 10^{-4}$. The response curve is shown in Fig. 3.4.

TE-mode eigenvalues were obtained via an internal excitation magnetic source at $\rho_{\text{fil}} = 1$. Here, no regularization is needed and $k_0 = 1.256$. The response curve is depicted in Fig. 3.5.

The eigenvalues for the TE and TM modes are shown in Table 4.1 along with the corresponding exact values and the results obtained by applying the FEM. The results of all three methods are in excellent agreement.

Elliptical Waveguide Consider the elliptical waveguide shown in Fig. 3.6 with large semiaxis $a = 2$ and small semiaxis $b = 1.5$; the eccentricity is thus $e = 0.66$. The

	TM modes			TE modes		
modes	EXACT	FEM (COMSOL)	MAS-ES	EXACT	FEM (COMSOL)	MAS-ES
1	1.202	1.201	1.203	0.920	0.920	0.921
2	1.915	1.915	1.915	1.527	1.526	1.526
3	2.567	2.566	2,568	1.915	1.915	1.916
4	2.760	2.759	2.760	2.100	2.099	2.100
5	3.190	3.189	3.190	2.658	2.657	2.659
6	3.507	3.506	3.508	2.665	2.664	2.666

TABLE 3.1: TE and TM eigenvalues for circular waveguide

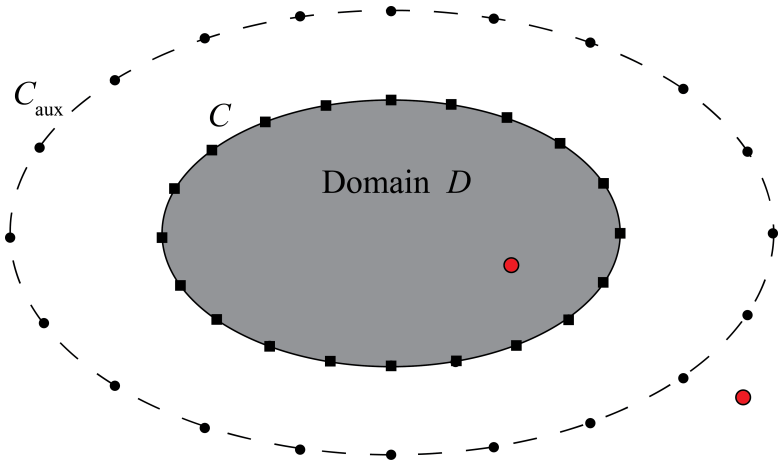

FIGURE 3.6: Application of MAS-ES for the elliptical waveguide.

coordinates of the collocation points are denoted by (x_{cyl}, y_{cyl}). The auxiliary points are located at $(x_{aux}, y_{aux}) = \sigma_{aux}(x_{cyl}, y_{cyl})$ with $\sigma_{aux} = 1.2$; thus the auxiliary curve is a similar ellipse enclosing the physical boundary C.

For the TM-mode eigenvalues an internal source at $(x_{fil}, y_{fil}) = (0.2, 0.2)$ was chosen. The corresponding response curve is shown in Fig. 3.7. TE-mode eigenvalues

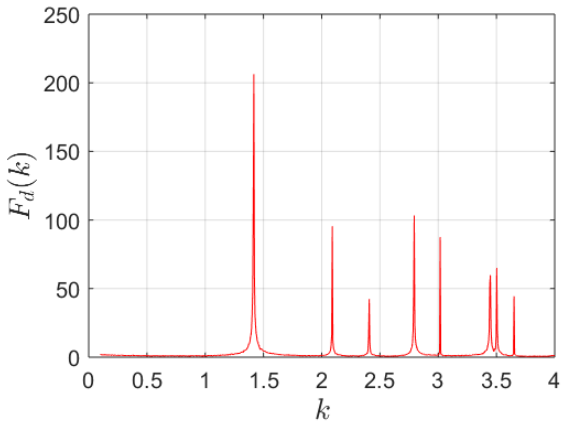

FIGURE 3.7: Response curve for the TM-mode eigenvalues of an elliptical waveguide obtained using an internal line source without a regularization procedure.

	TE modes		TM modes	
modes	FEM (COMSOL)	MAS-ES	FEM (COMSOL)	MAS-ES
1	0.929	0.929	1.414	1.415
2	1.209	1.210	2.089	2.090
3	1.656	1.655	2.404	2.406
4	1.786	1.788	2.791	2.792
5	2.340	2.340	3.015	3.017
6	2.347	2.347	3.444	3.446

TABLE 3.2: TE and TM eigenvalues for the elliptical waveguide

were found using a plane wave given by (3.14) with $\phi = \pi/4$. Friction regularization with $\varepsilon = 10^{-4}$ yielded a smooth response curve. All the other parameters are the same as in the TM-mode case. The response curve shown in Fig. 3.8. Table 3.2

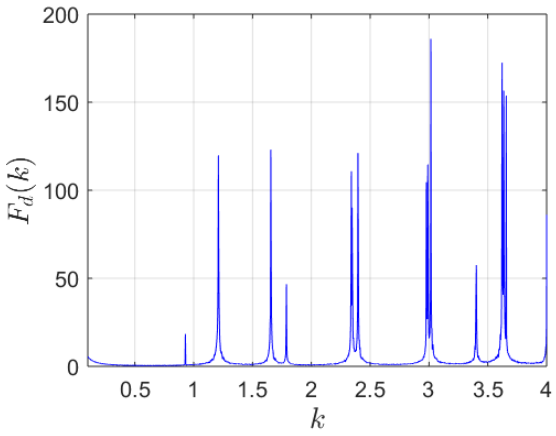

FIGURE 3.8: Response curve for the TE-mode eigenvalues of an elliptical waveguide obtained using a TE plane incident wave as the excitation source and the friction regularization technique with $\varepsilon = 10^{-4}$.

includes the computed TM and TE eigenvalues together with the results extracted by FEM. The close agreement between the results of MAS-ES and FEM is evident.

Rounded Triangular Waveguide The cross section of the rounded triangular waveguide is depicted in Fig. 3.9. The coordinates of the collocation points are

$$x_{\text{cyl}} = 1.75(\cos\varphi + 0.2\cos(2\varphi))$$
$$y_{\text{cyl}} = 1.75(\sin\varphi - 0.2\sin(2\varphi)),$$

where φ is the azimuthal angle. The auxiliary points are located at $(x_{\text{aux}}, y_{\text{aux}}) = \sigma_{\text{aux}}(x_{\text{cyl}}, y_{\text{cyl}})$, with $\sigma_{\text{aux}} = 1.2$.

For the TM-mode eigenvalues an external source at $(x_{\text{fil}}, y_{\text{fil}}) = (4, 4)$ was chosen, in conjunction with a shift-k regularization technique with $\Delta k = 0.1$. The response curve is shown in Fig. 3.10. TE-mode eigenvalues used an internal source at

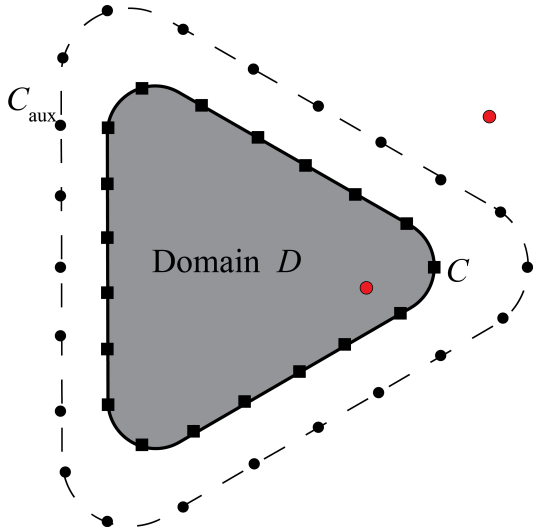

FIGURE 3.9: Application of MAS-ES for the rounded triangular waveguide.

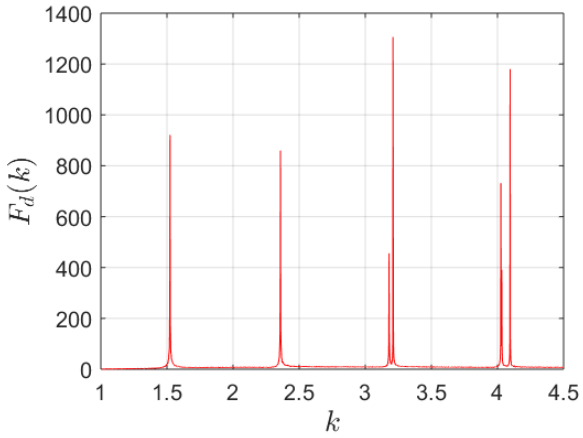

FIGURE 3.10: Response curve for TM-mode eigenvalues of the rounded triangular waveguide obtained using an external excitation source and the shift k regularization technique with $\Delta k = 0.1$.

$(x_{\text{fil}}, y_{\text{fil}}) = (0.2, 0.2)$. The response curve is depicted in Fig. 3.11. The eigenvalues are shown in Table 4.2 for both TM and TE modes. Once again very good agreement is observed between MAS-ES and FEM.

3.4.2 Multiply-connected domains

Fig. 3.12 shows an eccentric elliptical annular waveguide.

Circular concentric case Consider, first, the case of a waveguide that is circular and concentric, with outer and inner boundaries of radii $r_o = 2$ and $r_i = 0.5$. The auxiliary circular curves have radii $r_o^{\text{aux}} = 3$ and $r_i^{\text{aux}} = 0.4$. For the TM modes we use an internal source at $(x_{\text{fil}}, y_{\text{fil}}) = (1, 0)$, thus obtaining the response curve of Fig. 3.13. TE modes were obtained via an external source at $(x_{\text{fil}}, y_{\text{fil}}) = (4, 4)$, together with shift-$k$ regularization with $\Delta k = 0.1$. The response curve is shown in Fig. 3.14. The eigenvalues computed by MAS-ES and FEM are given in Table 3.4.

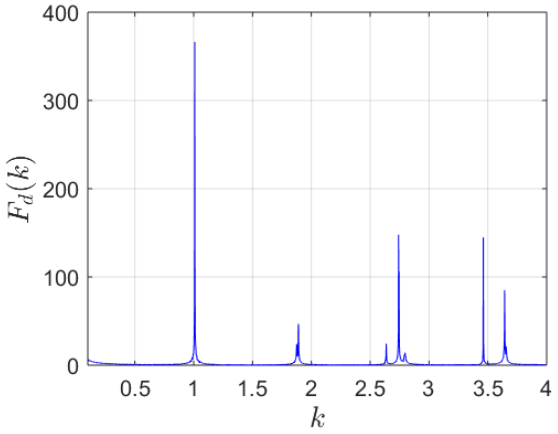

FIGURE 3.11: Response curve for TE-mode eigenvalues of the rounded triangular waveguide using an internal excitation source without a regularization method.

	TE modes		TM modes	
modes	FEM (COMSOL)	MAS-ES	FEM (COMSOL)	MAS-ES
1	1.008	1.009	1.517	1.523
2	1.876	1.877	2.347	2.359
3	1.887	1.891	3.159	3.166
4	2.635	2.636	3.196	3.201
5	2.742	2.742	4.000	4.007
6	2.798	2.796	4.017	4.022

TABLE 3.3: Eigenvalues for the rounded triangular waveguide

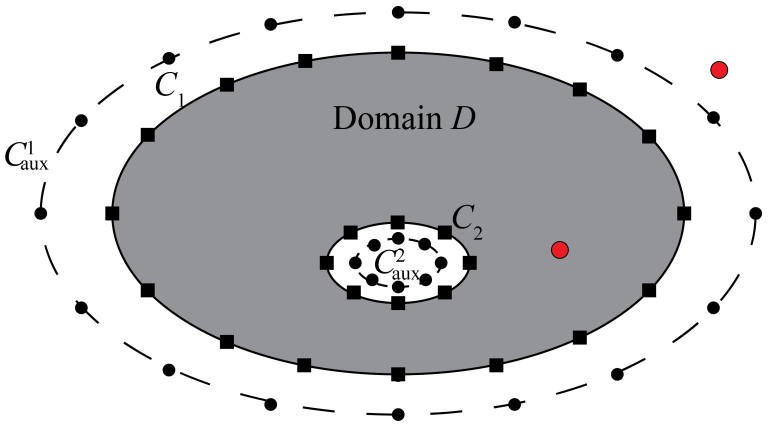

FIGURE 3.12: MAS-ES applied to eccentric elliptical annular waveguide

Elliptical Annular Waveguide A truly elliptical (i.e., noncircular) and noncentric waveguide (Fig. 3.12), was also studied. The inner ellipse has a large (small) semi-axis equal to $a_i = 0.5$ ($b_i = 0.375$), and has a center at $(0, -0.5)$. For the external

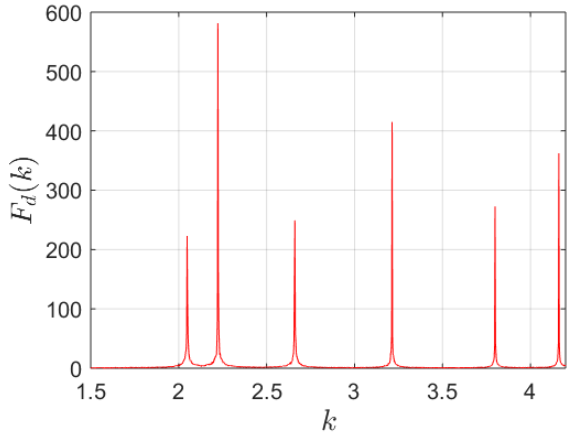

FIGURE 3.13: Response curve for TM-mode eigenvalues of the circular annular concentric waveguide obtained using an internal excitation source without a regularization procedure.

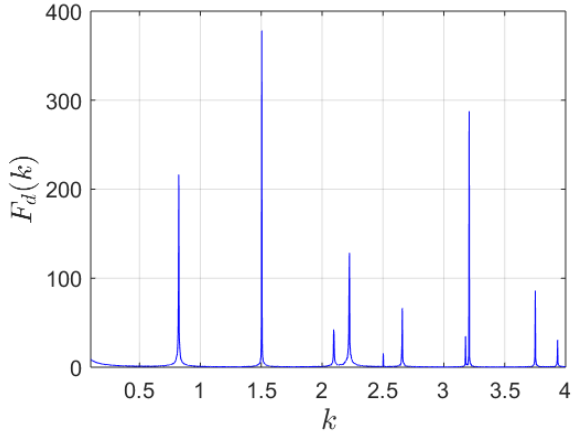

FIGURE 3.14: Response curve for TE-mode eigenvalues of the circular annular concentric waveguide obtained using an external excitation source and the shift-k regularization technique with $\Delta k = 0.1$

auxiliary ellipse, $\sigma_o^{\text{aux}} = 1.2$, while for the internal $\sigma_i^{\text{aux}} = 0.9$. For the TM modes, we used an external source at $(x_{\text{fil}}, y_{\text{fil}}) = (4, 4)$ and applied shift-k regularization with $\Delta k = 0.1$. The response curve is shown in Fig. 3.15. For the TE modes we use an internal source at $(x_{\text{fil}}, y_{\text{fil}}) = (1, 0)$ with $k_0 = 1.365$. The corresponding curve is depicted in Fig. 3.16. The eigenvalues are listed in Table 3.5 along with the values obtained by FEM.

The closeness observed in Tables 3.4 and 3.5 demonstrates the effectiveness of MAS-ES for multiply-connected domains.

3.4.3 Lossy waveguides

The performance of the MAS-ES for the computation of the eigenvalues of a waveguide filled with an actual realistic material (including losses) is exhibited by providing an additional example for a circular waveguide of radius $\rho_{\text{cyl}} = 2$ filled with Teflon (a material frequently used in microwave engineering). For Teflon, typical values of the real part of the complex permittivity and the loss tangent are

	TE modes		TM modes	
modes	FEM (COMSOL)	MAS-ES	FEM (COMSOL)	MAS-ES
1	0.821	0.821	2.048	2.050
2	1.504	1.505	2.221	2.223
3	2.095	2.095	2.658	2.661
4	2.222	2.223	3.211	3.213
5	2.501	2.502	3.797	3.800
6	2.657	2.658	4.160	4.163

TABLE 3.4: TE and TM eigenvalues for the circular annular concentric waveguide

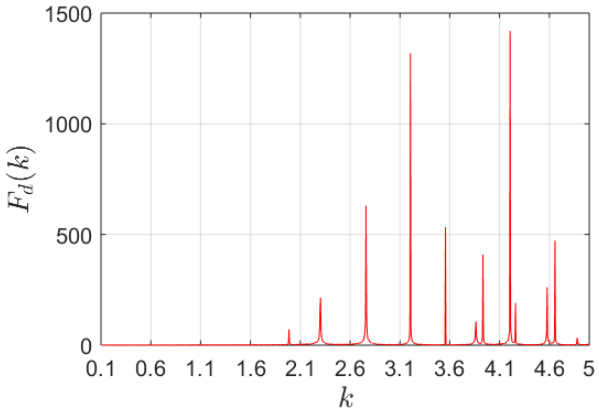

FIGURE 3.15: Response curve for TM-mode eigenvalues of the eccentric elliptical annular waveguide using an external excitation source and the shift-k regularization technique with $\Delta k = 0.1$.

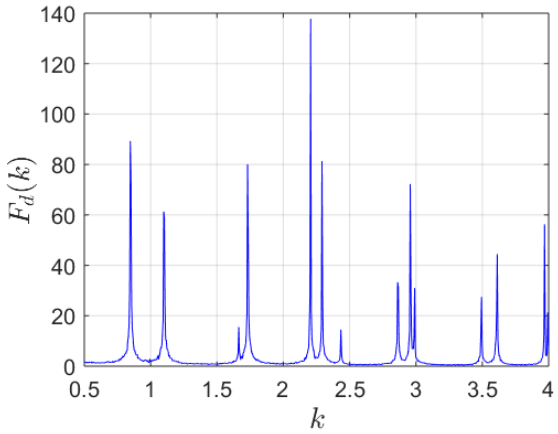

FIGURE 3.16: Response curve for TE-mode eigenvalues of the eccentric elliptical annular waveguide using an internal excitation source without a regularization method.

	TE modes		TM modes	
modes	FEM (COMSOL)	MAS-ES	FEM (COMSOL)	MAS-ES
1	0.848	0.848	1.987	1.987
2	1.093	1.100	2.300	2.304
3	1.662	1.665	2.759	2.759
4	1.730	1.734	3.203	3.205
5	2.197	2.205	3.555	3.557
6	2.292	2.294	3.860	3.864

TABLE 3.5: TE and TM eigenvalues for the eccentric elliptical annular waveguide.

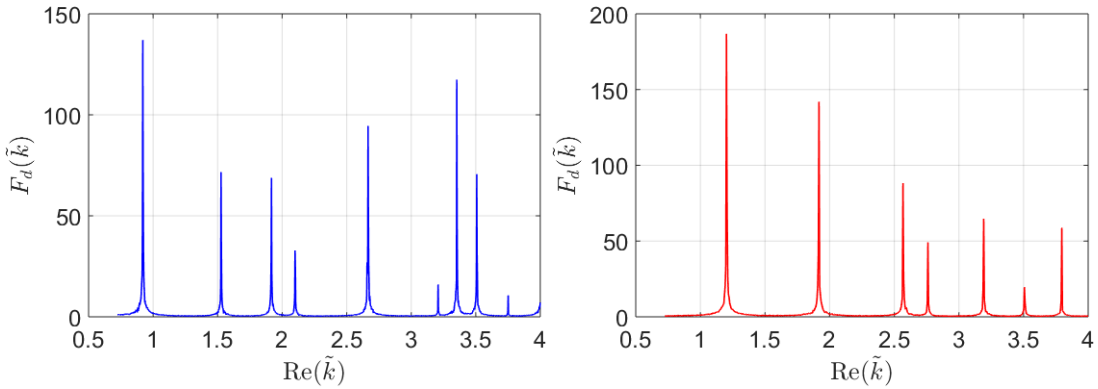

FIGURE 3.17: Response curves for the TE (upper panel) and TM (lower panel) modes of a circular waveguide with $\rho_{\mathrm{cyl}} = 2$ filled with Teflon. The horizontal axis is the real part of the complex wavenumbers $\tilde{k}$.

$\varepsilon_r' = 2.1$ and $\tan\delta = 3 \times 10^{-4}$, respectively [58]. Thus, the complex permittivity is given by $\tilde{\varepsilon}_r = \varepsilon_r' + \mathrm{i}\varepsilon_r'' = 2.1 + \mathrm{i}\,0.00063$, and the complex refractive index by $\tilde{n} = \sqrt{\tilde{\varepsilon}_r} = 1.4491 + \mathrm{i}\,0.0002$. Then, the complex wavenumber is $\tilde{k} = \tilde{k}_0\tilde{n} = k' + \mathrm{i}k''$, where $\tilde{k}_0$ is the free-space wavenumber.

The complex eigenvalues of the above-described Teflon waveguide are computed by MAS-ES with an internal excitation source located at $(x_{\mathrm{fil}}, 0) = (1, 0)$. The results are depicted in Tables 3.6 and 3.7, where they are also compared with the ones obtained by FEM, showing a very good agreement both in the real and in the imaginary parts of the eigenvalues. The corresponding response curves for the TE and TM modes are illustrated in Fig. 3.17.

3.4.4 Divergent MAS currents; convergent MAS eigenvalues

For the case of external excitation, we finally present results demonstrating MAS-current divergence together with response-curve and eigenvalue convergence.

modes	FEM (COMSOL)	MAS-ES
1	0.9187294+0.0001268i	0.9187294 +0.0001268i
2	1.5259023+0.0002106i	1.5259023 +0.0002106i
3	1.9171593+0.0002646i	1.9171593 +0.0002646i
4	2.0982968 + 0.0002896i	2.0997459 +0.0002898i
5	2.6634458 +0.0003676i	2.6648949 +0.0003678i
6	3.2054092 +0.0004424i	3.2083074 +0.0004428i

TABLE 3.6: TE complex eigenvalues for a circular Teflon waveguide with $\rho_{\text{cyl}} = 2$

modes	FEM (COMSOL)	MAS-ES
1	1.2013039+0.0001658i	1.202753 +0.000166i
2	1.9171593+0.0002646i	1.9171593 +0.0002646i
3	2.5663561+0.0003542i	2.5678052+0.0003544i
4	2.7590864+0.0003808i	2.7605355 +0.000381i
5	3.18802 + 0.00044i	3.1923673 +0.0004406i
6	3.5053729+0.0004838i	3.5082711+ 0.0004842i

TABLE 3.7: TM complex eigenvalues for a circular Teflon waveguide with $\rho_{\text{cyl}} = 2$

Circular case Consider the circular waveguide of Fig. 3.3 with $\rho_{\text{cyl}} = 2$ excited by an electric (magnetic) external source at $(x_{\text{fil}}, y_{\text{fil}}) = (4, 0)$. For $\rho_{\text{aux}} = 6 > \rho_{\text{fil}}$, one obtains the divergent currents of Fig. 3.18 (which show oscillating real parts only) for the first TM (TE) eigenvalue. Similar results occur for the other eigenvalues. Nevertheless, the response curve is not affected by these oscillations and is found to be very similar to the ones of Figs. 3.4 and 3.5.

Noncircular case Similar results occur for external excitations of noncircular shapes. Fig. 3.19, for example, was obtained with $\sigma_{\text{aux}} = 2.5$ for the elliptic waveguide of Fig.

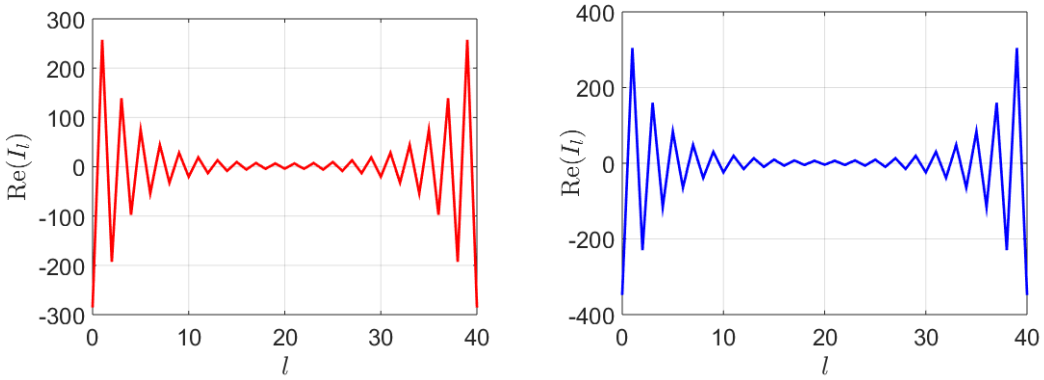

FIGURE 3.18: Oscillations of the diverging real parts of the MAS currents for the first eigenvalue of the TM modes (left panel) and TE modes (right panel) for external excitation.

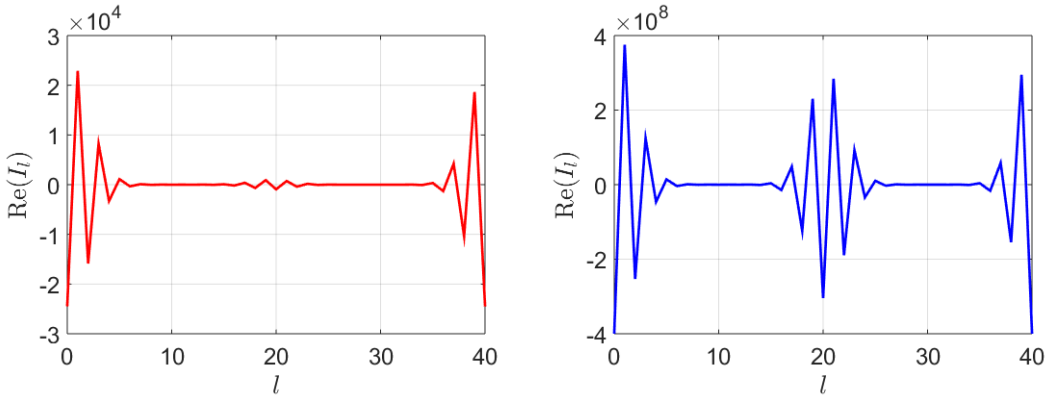

FIGURE 3.19: Oscillations of the diverging real parts of the MAS currents for the first eigenvalue of the TM modes (left panel) and TE modes (right panel) for external excitation in an elliptical waveguide.

3.6. The observed oscillations occur because the exciting line source lies in the interior of the auxiliary curve, as discussed in Section 3.3.6. Despite the oscillations, we found a similar response curve and identical eigenvalues.

3.5 Computer times: A discussion

Although CPU-time optimization is not a main focus of this chpater, this section does include some discussions. The aim is to show that a properly optimized and improved code will be capable of yielding computer times that can outperform other methods.

As a test case we choose the above-described rounded triangle, for which the COMSOL CPU time is 3 s (seconds). We use $N = 35$ and $N_t = 10$, and $N_g = 1000$ or $N_g = 1500$ (an increase in N_g was sometimes necessary in order not to loose peaks). With these parameters, our MATLAB MAS-ES time is 6.0 s for TM modes and 8.2 s for TE modes. These large times are greatly reduced if the matrix elements are preloaded, as they reduce to 1.3 s and 1.4 s, respectively.

This last comparison, which excludes matrix fill-times, might seem unfair. However, we believe it to be relevant because MAS-ES has the following property, which is uncommon in numerical methods: *All* matrix elements are Hankel functions of a single *real* variable, denoted here by x. (In the notation of Section 3.2.2 and Eq. (3.16), $x = k\,|\mathbf{r}_m - \mathbf{r}_l|$.)

For definiteness, suppose that one wishes to optimize the dimensions of a waveguide, calling for a large number of runs for waveguides of differing dimensions. In such a scenario, the range of x will be roughly known beforehand, as the smallest (largest) x-value will be the minimum (maximum) electrical distance between points on the auxiliary surfaces and points on the waveguide. Therefore, it is not difficult, in principal, to pre-store the necessary Hankel-function values (in a complex-valued array) and, given x, to look the desired value up (or, depending on the desired accuracy, to interpolate between the stored values). Given the small times required for look-ups of this sort—even when the array is very large—the effect on the overall CPU time is expected to be negligible. This process will be further helped by the fact that x cannot be very small; for this reason, the Hankel-function values cannot be very large and will therefore not vary much (as compared, say, to MoM-based methods, in which x can be vanishingly small).

Another idea (which can be considered to be a variation to MAS-ES) is to find eigenvalues via the peaks of the auxiliary currents themselves, thus completely avoiding the need of computing fields and response functions. This required 5.5 s for TM modes and 7.3 s for TE modes. With preloaded matrices, these dropped to 0.38 s and 0.40 s, which are an order of magnitude smaller than the COMSOL time of 3 s. These results should be considered preliminary; we plan to examine this promising method thoroughly in the near future, with due attention to the phenomenon of auxiliary-current oscillations.

3.6 Conclusion

MAS-ES is a mode-analysis numerical technique combining the general approach of MAS together with the use of an external or internal excitation source. MAS-ES computes the eigenvalues by measuring the generated fields in the waveguide's domain due to the excitation source by means of a response function $F(k)$, the peaks of which correspond to the eigenvalues. For external excitations, obtaining an $F(k)$ with sharp peaks requires a regularization method. For internal excitation, on the other hand, no regularization procedure is required; this constitutes a significant improvement to the method's robustness. Many numerical experiments for simply- and multiply-connected geometries showed response curves free of spurious oscillations and excellent agreement with FEM results. Finally, it was demonstrated that the divergence of the MAS currents appears as oscillations of their real parts between large values of alternating sign. Importantly, however, this divergence may not affect the computation of the eigenvalues. In the future, we plan to extend this work to 3-D resonating cavities.

Chapter 4

Method of Auxiliary Sources with an Excitation Source: The Auxiliary-Current Vector Norm

4.1 Introduction

This chapter improves and complements the previois one, by showing that eigenvalues can be determined via what we call the *Auxiliary Current-Vector Norm* (ACVN). The vector components are the complex amplitudes of the auxiliary (MAS) currents. Use of the ACVN instead of $F(k)$ is algorithmically simpler because there is no need to calculate the field at randomly chosen points inside the waveguide. On the other hand, this method has the peculiarity of obtaining physical results (eigenvalues) from non-physical quantities (the auxiliary currents). Thus, our *analytical* study for the simple problem of a *circular* waveguide (Section 4.2) is helpful in explaining how and why the method works; in addition, it points to potential difficulties. We also include a Hankel-function look-up technique that reduces CPU times. An $\exp(-\mathrm{i}\omega t)$ time dependence is assumed.

4.2 Circular Waveguide

Fig. 4.1 shows a hollow circular waveguide with perfect electric conducting (PEC) boundary of radius ρ_{cyl}. In the TM case of the figure, the excitation is a line-source current filament I, lying within the waveguide ($\rho_{\text{fil}} < \rho_{\text{cyl}}$), or the waveguide's exterior ($\rho_{\text{fil}} > \rho_{\text{cyl}}$). The $N = 16$ points are line sources I_n ($n = 0, 1, \ldots, N-1$) that lie on an auxiliary surface of radius $\rho_{\text{aux}} > \rho_{\text{cyl}}$. As discussed in the previous chapter and in [56], one can *analytically* determine the limit, as $N \to \infty$, of the auxiliary currents. In the limit, the discrete MAS currents become a surface current density $J^s_{\text{limit}}(\phi_{\text{aux}})$, where ϕ_{aux} is shown in the figure. For TE polarization, we replace I and I_n by *magnetic* line currents I_M and I_{M_n}; the limit then corresponds to a magnetic surface current density $K^s_{\text{limit}}(\phi_{\text{aux}})$. The eigenvalues are known beforehand to be all k that satisfy

$$J_n(k\rho_{\text{cyl}}) = 0 \quad \text{and} \quad J'_n(k\rho_{\text{cyl}}) = 0, \quad n = 0, 1, 2, ..., \tag{4.1}$$

for the TM and TE cases, respectively.

4.2.1 Internal Excitation

In the TM case, the above-described limit is given by

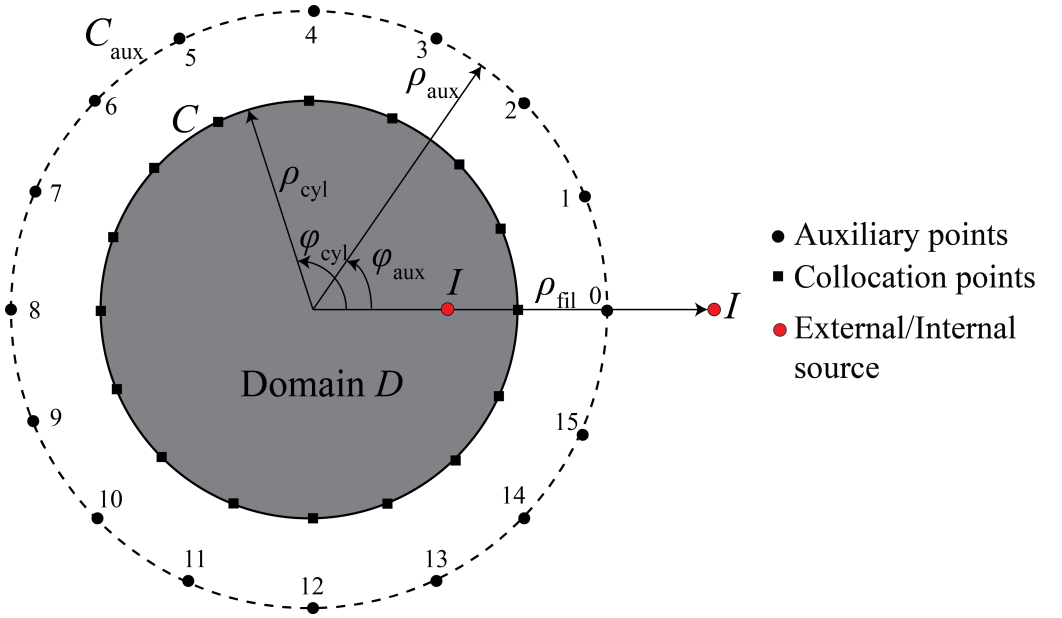

FIGURE 4.1: Circular waveguide with external or internal TM excitation.

$$J^s_{\text{limit}}(\phi_{\text{aux}}) = -\frac{I}{2\pi\rho_{\text{aux}}}\sum_{n=-\infty}^{\infty}\frac{J_n(k\rho_{\text{fil}})\,H_n^{(1)}(k\rho_{\text{cyl}})}{H_n^{(1)}(k\rho_{\text{aux}})\,J_n(k\rho_{\text{cyl}})}e^{in\phi_{\text{aux}}}, \tag{4.2}$$

see (3.35). Thus, at any TM resonance, the presence of $J_n(k\rho_{\text{cyl}})$ causes some term in the series to become infinite. In actual application with finite N, the discrete auxiliary currents I_n will become *large* at the resonances. Our method thus consists of plotting what we define as the ACVN $\|I_{\text{aux}}(k)\| \equiv \sum_{n=0}^{N-1}|I_n|$, as function of k, for a dense set of k. The peaks of this plot correspond to the TM eigenvalues.

The series in (4.2), however, presents a well-studied [20], [26], [27], [56] difficulty: The n-th term of the series behaves as $(\rho_{\text{aux}}/\rho_{\text{cri}})^n$, in which the *critical radius* $\rho_{\text{cri}} = \rho_{\text{cyl}}^2/\rho_{\text{fil}}$ satisfies $\rho_{\text{cri}} > \rho_{\text{cyl}}$. Thus, the series converges when $\rho_{\text{aux}} < \rho_{\text{cri}}$, but diverges exponentially otherwise. When N is finite, the above divergence manifests itself as rapid oscillations in real parts of the auxiliary currents. Similar oscillations arise in noncircular geometries and are a potential source of difficulty when one applies the method [20], [26], [27], [56].

All these conclusions continue to hold in the TE case: The limit $K^s_{\text{limit}}(\phi_{\text{aux}})$ is given by a Fourier series with a $J_n'(k\rho_{\text{cyl}})$ in the denominator of the n-th term. We thus find resonances by plotting the ACVN $\|K_{\text{aux}}(k)\| \equiv \sum_{n=0}^{N-1}|I_{M_n}|$ vs. k. This Fourier series diverges when $\rho_{\text{aux}} > \rho_{\text{cri}}$, in which case oscillations will arise.

4.2.2 External Excitation

For an external excitation and TM polarization, we can show that the series corresponding to (4.2) is

$$J^s_{\text{limit}}(\phi_{\text{aux}}) = -\frac{I}{2\pi\rho_{\text{aux}}}\sum_{n=-\infty}^{\infty}\frac{H_n^{(1)}(k\rho_{\text{fil}})}{H_n^{(1)}(k\rho_{\text{aux}})}e^{in\phi_{\text{aux}}}. \tag{4.3}$$

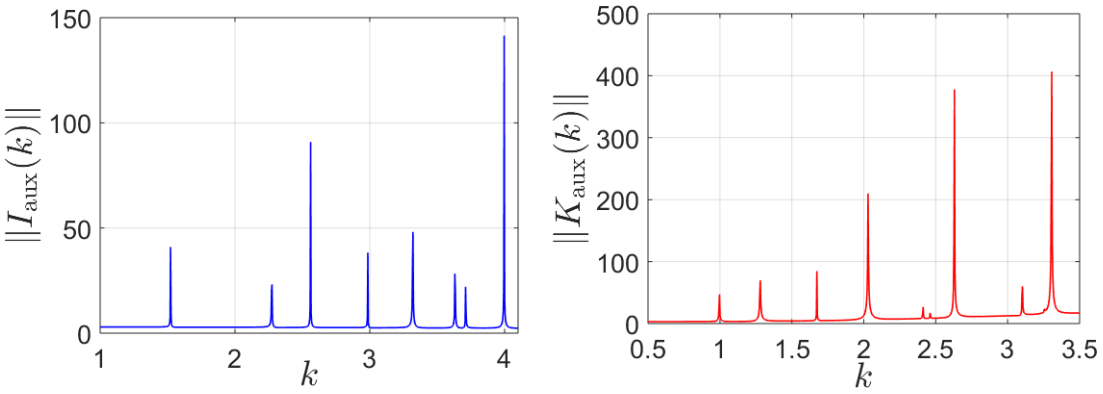

FIGURE 4.2: Plots of $\|I_{\text{aux}}(k)\|$ (left panel, TM case) and $\|K_{\text{aux}}(k)\|$ (right panel, TE case) for the super-elliptic waveguide.

Since there is no $J_n(k\rho_{\text{cyl}})$ in the denominator, there seems to be no *direct* way of detecting eigenvalues. We can circumvent this by applying one of the two regularization methods of [49]–[51]. To illustrate, shift-k regularization yields

$$J^s_{\text{limit}}(\phi_{\text{aux}}) = -\frac{I}{2\pi\rho_{\text{aux}}} \times \sum_{n=-\infty}^{\infty} \frac{H_n^{(1)}((k+\Delta k)\rho_{\text{fil}})\, J_n((k+\Delta k)\rho_{\text{cyl}})}{H_n^{(1)}(k\rho_{\text{aux}})\, J_n(k\rho_{\text{cyl}})} e^{in\phi_{\text{aux}}}, \tag{4.4}$$

which reduces to (4.3) when $\Delta k \to 0$, and whose denominator presents the desired factor $J_n(k\rho_{\text{cyl}})$. Our conclusions carry over to friction regularization, and to the TE case.

4.3 Numerical Results

In all numerical results that follow, the numbers of measurement, plot, and collocation/auxiliary points are 20, 2000, and $N = 40$, respectively. We compare to results obtained by the $F(k)$-approach of chpater 3, and to FEM.

Our first waveguide is super-elliptic, with a boundary C whose coordinates are

$$x_{\text{cyl}} = a\ \text{sgn}(\cos\varphi)|\cos\varphi|^{2/n},$$
$$y_{\text{cyl}} = b\ \text{sgn}(\sin\varphi)|\sin\varphi|^{2/n},$$

with $a = 2$, $b = 1.5$, $n = 3/2$, and φ is the azimuthal angle. The auxiliary points are located on C_{aux}, with coordinates $(x_{\text{aux}}, y_{\text{aux}}) = \sigma_{\text{aux}}(x_{\text{cyl}}, y_{\text{cyl}})$ where $\sigma_{\text{aux}} = 1.2$. For TM polarization and an internal source at $(x_{\text{fil}}, y_{\text{fil}}) = (1, 0)$, we obtain the ACVN plot in Fig. 4.2 (left). For the TE case, an external source at $(x_{\text{fil}}, y_{\text{fil}}) = (4, 4)$, and shift-$k$ regularization with $\Delta k = 0.1$, we obtain Fig. 4.2 (right). Peak locations are given in Table 4.1, along with corresponding values by FEM. Excellent agreement is observed.

Our second example is the multiply-connected waveguide of Fig. 4.3. It consists of a super-elliptic external boundary C_1 and an elliptic internal boundary C_2. The ellipse C_2 has semi-axes $a_i = 0.5$ and $b_i = 0.375$ and a center at $(0, -0.5)$. The auxiliary curve C^1_{aux} (C^2_{aux}) is a scaled version of C_1 (C_2) with a scaling factor $\sigma_o^{\text{aux}} = 1.2$ ($\sigma_i^{\text{aux}} = 0.8$). Here, our ACVN's make use of the electric/magnetic current amplitudes belonging to *both* boundaries. For TM modes, we used an external source at $(x_{\text{fil}}, y_{\text{fil}}) = (4, 0)$ and shift-k regularization with $\Delta k = 0.1$ to obtain Fig. 4.4 (left).

	TE modes		TM modes	
modes	FEM	MAS-ES	FEM	MAS-ES
1	0.996	0.997	1.522	1.522
2	1.279	1.280	2.272	2.275
3	1.674	1.674	2.559	2.561
4	2.028	2.030	2.984	2.986
5	2.462	2.461	3.317	3.320
6	2.627	2.630	3.631	3.631

TABLE 4.1: Eigenvalues of the super-elliptical waveguide

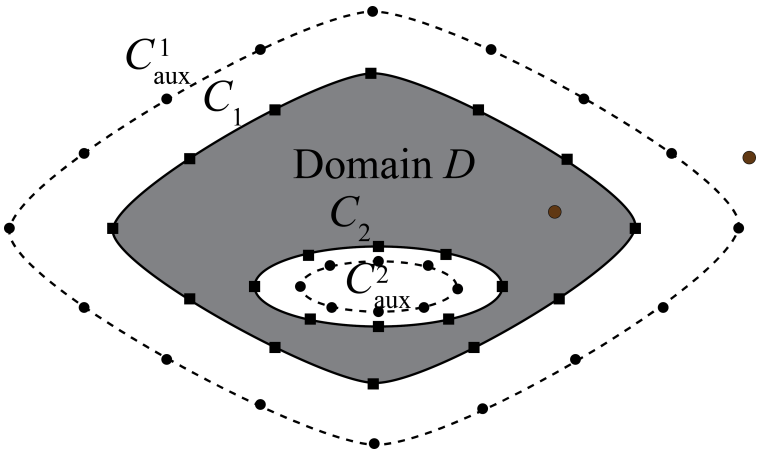

FIGURE 4.3: Multiply-connected waveguide.

For TE modes, we used an internal source at $(x_{\text{fil}}, y_{\text{fil}}) = (1, 0)$ to obtain Fig. 4.4 (right). A table like Table 4.1 (not shown for brevity) exhibits an 3-4 significant digits agreement of FEM and MAS-ES.

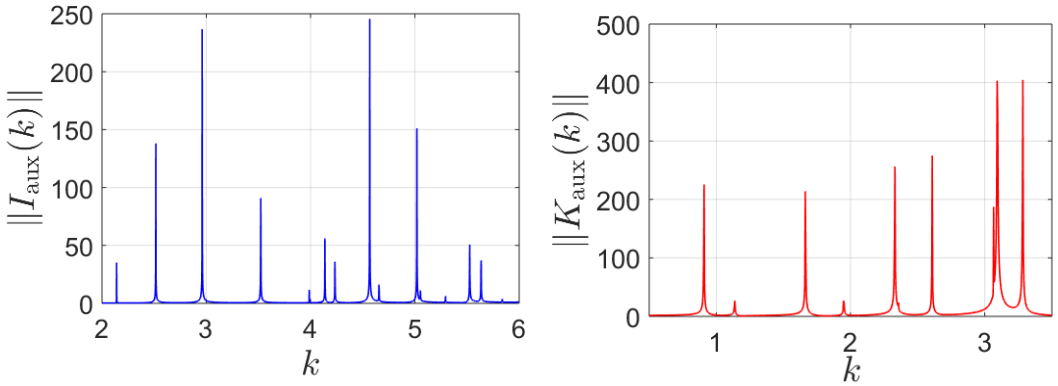

FIGURE 4.4: Plots of $\|I_{\text{aux}}(k)\|$ (left panel, TM case) and $\|K_{\text{aux}}(k)\|$ (right panel, TE case) for the waveguide of Fig. 4.3.

One important advantage of the ACVN over the $F(k)$ approach is that for a small number of auxiliary sources the ACVN plots are much smoother than the $F(k)$ response curves. This is illustrated in Fig. 4.5 with both plots corresponding to the TM modes for the elliptical geometry of chpater 3, obtained for $N = 25$ auxiliary sources and $N_t = 10$ measurement points (for the $F(k)$ response curve). Zooming in the

$F(k)$ resonance peak of the eigenvalue $k = 2.404$, a secondary peak is observed due to non-smoothness. This local maximum is detected by the peak-finding algorithm, and the corresponding wavenumber k is falsely stored as an eigenvalue. Similar findings are encountered in the majority of the resonant peaks of $F(k)$. The ACVN plot on the other hand, is very smooth and only the correct eigenvalues are detected.

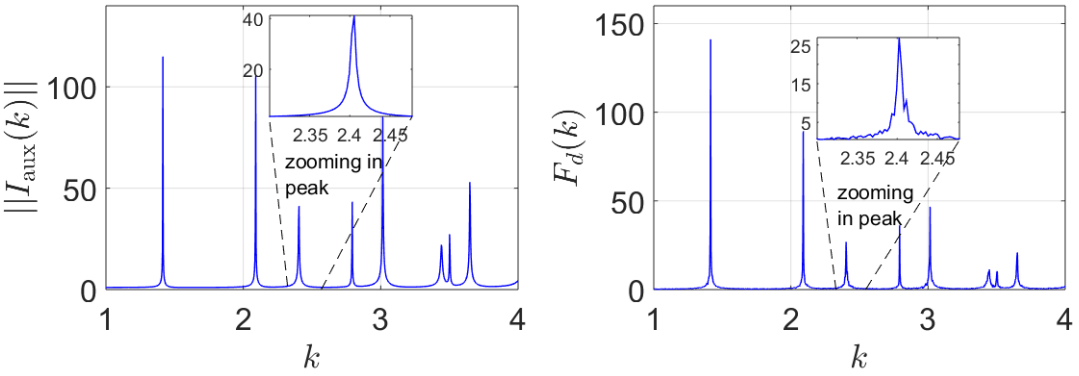

FIGURE 4.5: The ACVN plot (left panel), and the $F(k)$ response curve (right panel) for the TM modes of the elliptic waveguide of chapter 3. The same peak area is enlarged and embedded in the main plots.

4.4 Oscillations in the auxiliary currents

As mentioned in Section 4.2 for the circular geometry, oscillations are a potential source of difficulty. While it is evident that *severe* oscillations should be avoided, it is also true that not-too-severe oscillations can still yield correct results. The circular problem explains this, because the *fields* obtained from the oscillating currents are correct, see chapter 3 and [27] for details (within the context of MAS-ES and MAS, respectively).

For MAS-ES with the ACVN, we illustrate such correct results via the inverted elliptic geometry (depicted in Fig. 7a of [26]), with CPs lying on the PEC boundary with

$$x_{\text{cyl}} = 1.884\frac{1.3\cos\varphi}{1+0.6\cos(2\varphi)+0.09},$$

$$y_{\text{cyl}} = 1.884\frac{0.7\sin\varphi}{1+0.6\cos(2\varphi)+0.09},$$

and with a TM plane-wave as the excitation source. This geometry has two external branch points at $(\pm 1.3186, 0)$ [26]; when $\sigma_{\text{aux}} = 1.8$, these lie in the interior of the auxiliary curve. Consequently, the auxiliary currents oscillate, see the real parts in Fig. 5.11 (right). We stress that the oscillating values are orders of magnitude larger than cases where the auxiliary curve is small enough to avoid oscillations. Despite the oscillations, eigenvalue determination is unaffected: see Fig. 5.11 (left), which gives nearly identical values with the non-oscillating cases.

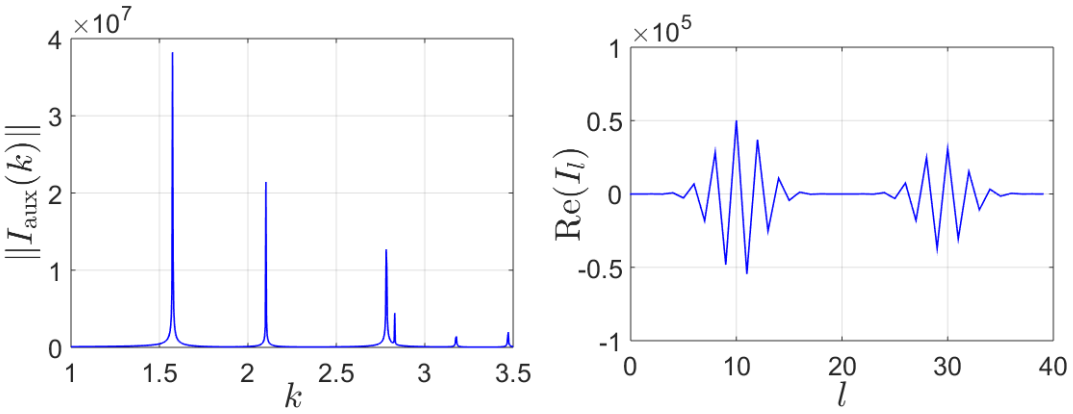

FIGURE 4.6: Plots of $\|I_{\text{aux}}(k)\|$ (left panel) and $\text{Re}(I_l)$ (right panel) for the inverted elliptic geometry.

4.5 Computer Times

In MAS-ES, *all* matrix elements are Hankel functions ($H_0^{(1)}$ for TM and $H_1^{(1)}$ for TE modes) of a real variable x, a feature uncommon in numerical methods. We reduced computer times by implementing an idea suggested in chpater 3, namely to replace Hankel-function computations by array look-ups. (Look-up times are typically small, even for large arrays.) Since the range of x depends on the geometry, it is roughly known beforehand (even in scenarios such as geometry optimization). We specifically prestored an array with 10^7 Hankel-function values and, for any given x, looked up the closest value.

We conducted extensive numerical experiments for all waveguides studied in chpater 3. The representative results of Table 4.2 reveal that the lookup procedure is successful and leads to much lower computation times; also, that the ACVN method requires less CPU time than does the $F(k)$-approach. As a matter of fact, when combined with the lookup procedure, the ACVN method usually requires less time than Comsol Multuphysics which is a FEM-based software package (Comsol Multiphysics). Thus, the methods introduced herein constitute a significant improvement of MAS-ES. Notably, the computation time of Comsol is the same for every geometry since their areas are similar and the center frequecy around which the eigenvalues are computed is the same.

At this point, we mention that contrary to the FEM, the CPU times of MAS-ES are not affected by the increase of the center frequency around which the eigenvalues are computed. To prove this, numerical experiments were conducted for the TE modes of a circular waveguide with radius $\rho_{\text{cyl}} = 1$ m. Specifically, changing the center frequency from 100 MHz to 1000 MHz, the CPU times gradually increase from 4 s to 7 s for FEM and from 0.33 s to 0.43 s for the ACVN MAS-ES. Similar results are obtained for more complex geometries.

4.6 Conclusions

Instead of using the response function of MAS-ES, waveguide eigenvalues can be found from the peaks of the ACVN. This method is algorithmically simpler. Numerical experiments for several geometries show excellent agreements with FEM results. They also demonstrate that not-too-rapid oscillations in the auxiliary currents do not affect the eigenvalues' determination. When combined with the Hankel-function

TM modes	Circular	Elliptic	Rounded Triangle	Circular ann. con.	Elliptical ann. ecc.
F(k)	1.069	3.571	5.999	2.625	12.568
F(k) lookup	0.992	1.731	2.469	2.117	3.311
ACVN	0.478	3.008	5.471	1.542	11.421
ACVN lookup	0.362	1.109	2.004	1.290	2.227
FEM	3	3	3	3	3

TABLE 4.2: CPU times (in secs) for the geometries of chapter 3.

lookup-procedure of Section 4.5, the present approach requires very small computer times, even for complicated geometries.

Chapter 5

Computing Eigenvalues of Dielectric Waveguides by a Method of Auxiliary Sources with Two Excitation Sources

5.1 Introduction

Cylindrical dielectric waveguides are extensively used in optics mainly in the form of optical fibers with circular or elliptical core shapes. Most optical fibers are constructed from glass without impurities and exhibit advantages such as low transmission loss and manufacturing cost, light weight, high carrying capacity and long life cycle [59].

One of the fundamental problems in cylindrical dielectric waveguides is the determination of modes' eigenvalues (i.e., the propagation constants β of the guided waves). Analytical solutions exist only for waveguides with circular [60]–[62] and elliptical cores [63]–[65]. For other cases, the eigenvalue problem is solved numerically; reviews of related numerical methods are contained in [66] and [67]. Two widely-used methods for modal analysis of dielectric waveguides are the Finite Element Method (FEM) [68]–[71] and the Finite Difference Method (FDM) [72]–[75]. Surface Integral-Equation Based Methods are also effective for computing the eigenvalues. These are based on solving an integral equation on the core-cladding boundary either by point matching [76], [77] or by the boundary element method [78], [79]. However, in these methods the integration and the physical boundary curves coincide, resulting in weakly singular integral equations. To avoid this, methods have been developed that formulate an equivalent problem in which the current distribution lies on a fictitious curve that is displaced from the physical boundary. One of these methods is the Method of Auxiliary Sources.

There are two approaches when using MAS in mode analysis problems. In the first approach, referred to as standard MAS, a nondriven problem (with no incident fields) is formulated leading to a homogeneous linear system [47], [80], [81]. The eigenvalues are detected as the propagation constants for which the involved impedance matrix $Z(\beta)$ becomes singular. These constants correspond to the zeros of the determinant of $Z(\beta)$. The drawback of this approach is that a number of discrete spurious eigenvalues may also be detected.

The main purpose of this chapter is to demonstrate that MAS-ES is also suitable for computing accurately and with no spurious solutions the propagation constants of a cylindrical dielectric waveguide with arbitrary cross section of its core. Still, since dielectric waveguides generally support the propagation of hybrid modes, a

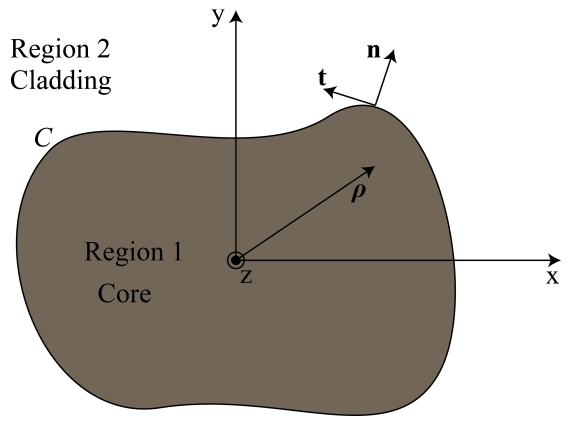

FIGURE 5.1: Cross section of a cylindrical dielectric waveguide with an arbitrarily-shaped core.

modification is necessary. Specifically, two excitation sources (instead of one as in PEC hollow waveguides), an electric and a magnetic current filament placed inside the waveguides' core and parallel to its axis, are utilized. The method thus obtained is referred to as the Method of Auxiliary Sources with Two Excitation Sources (MAS-TES). Since the propagating modes are localized in the core, one can detect the eigenvalues by measuring the response of the core to the two internal sources. This is performed by employing a response function $F(\beta)$, which is maximized when a standing wave is formed inside the core and an evanescent wave in the cladding. Plotting $F(\beta)$ for a dense set of β results in a response curve the peaks of which correspond to the eigenvalues of the dielectric waveguide.

This chapter is organized as follows: The fundamental theory of dielectric waveguides is presented in Section 5.2. In Section 5.3, we describe the application of MAS-TES to cylindrical dielectric waveguides. Section 5.4 contains the analytical solution for the circular dielectric waveguide. In Section 5.5. results of numerical experiments demonstrating the effectiveness of MAS-TES. Six different core geometries are studied, including two multimode dielectric waveguides.

An $e^{i\omega t}$ time dependence is assumed and suppressed throughout the following analysis.

5.2 Fundamentals of Cylindrical Dielectric Waveguides

A cross section of a dielectric waveguide, which extends infinitely in the z-direction, is depicted in Fig. 5.1. It consists of two regions R_1 and R_2 filled with homogeneous, isotropic, and non-magnetic dielectric materials. Region R_1 is the *core* (guiding medium), which has an arbitrary cross section and is characterized by a high index of refraction n_1 and dielectric permittivity ϵ_1. Region R_2 is the *cladding* surrounding the core and is characterized by a lower index of refraction $n_2 < n_1$ and permittivity ϵ_2. In single-mode optical fibers, the thickness of the cladding is more than ten times larger than that of the core; hence, the cladding can be assumed to be of infinite extent. However, in multimode optical fibers, the thickness of the cladding and the core are comparable. The analysis of this section concerns waveguides with infinite cladding.

A dielectric waveguide can theoretically support an infinite number of guided fields (modes). We are usually interested in modes with their fields confined in the

vicinity of the core. There are two approaches for the related mode analysis problem, depending on the presence or not of sources. Below, we present the theoretical aspects of both approaches.

In *source-free* regions, the electric and magnetic fields of the modes satisfy Faraday's and Ampère's laws

$$\nabla \times \mathbf{E}_s = -\mathrm{i}\omega\mu_0\mathbf{H}_s,\ \nabla \times \mathbf{H}_s = \mathrm{i}\omega\epsilon_0 n_s^2\mathbf{E}_s, \tag{5.1}$$

where ω is the angular frequency, ϵ_0 and μ_0 the free-space permittivity and permeability, and $s = 1, 2$ characterizes regions R_1 (core) and R_2 (cladding). Eqs. (5.1) are reduced to the *homogeneous* Helmholtz equations in R_1 and R_2

$$\nabla^2\mathbf{E}_s + k_0^2 n_s^2\mathbf{E}_s = \mathbf{0},\ \nabla^2\mathbf{H}_s + k_0^2 n_s^2\mathbf{H}_s = \mathbf{0}, \tag{5.2}$$

where $k_0 = \omega/c = 2\pi/\lambda_0$, c is the speed of light, and λ_0 is the free-space wavelength.

For propagating fields along the z-direction, it is assumed that their z-dependence is of the form $e^{-\mathrm{i}\beta z}$, i.e.,

$$\mathbf{E}_s = \mathbf{E}(\boldsymbol{\rho})e^{-\mathrm{i}\beta z},\ \mathbf{H}_s = \mathbf{H}(\boldsymbol{\rho})e^{-\mathrm{i}\beta z}, \tag{5.3}$$

where $\boldsymbol{\rho}$ is a vector on the transverse plane (cross section of the waveguide) and β the propagation constant. Satisfying the transmission conditions on the core-cladding boundary C requires (except for some special cases) contributions from both TM_z and TE_z fields (Sec. 3.1 of [82]). Thus, modes with both E_z and H_z components are supported, which are known as *hybrid modes* and designated as HE or EH modes, depending on whether H_z or E_z dominates [83].

By (5.2) and (5.3), the fields on the cross section of the waveguide satisfy

$$(\nabla_{xy}^2 + k_{\rho_s}^2)\mathbf{E}_s = \mathbf{0},\ (\nabla_{xy}^2 + k_{\rho_s}^2)\mathbf{H}_s = \mathbf{0}, \tag{5.4}$$

where ∇_{xy}^2 is the transverse Laplacian and

$$k_{\rho_s}^2 = k_0^2 n_s^2 - \beta^2 \tag{5.5}$$

are the radial wavenumbers of the transverse fields in the core ($s = 1$) and the cladding ($s = 2$).

For a propagating, transverse field localized near the core, we seek a *resonant* (standing) wave solution in the core, together with an evanescent wave solution in the cladding (related to the energy leaking from the standing wave of the core). This is possible only when k_{ρ_1} is real and k_{ρ_2} is purely imaginary with a negative imaginary part, leading to the following condition for the propagation constant β

$$0 < k_0 n_2 < \beta < k_0 n_1. \tag{5.6}$$

Only a finite number of values of β in the range of (5.6) correspond to guided modes in the vicinity of the core. These are determined by the shape of the boundary C and the material parameters of R_1 and R_2. We refer to these values as the *eigenvalues* of the dielectric waveguide at the specific frequency $f = ck_0/2\pi$. Any other value of β, besides the eigenvalues, corresponds to a field for which most of its electromagnetic energy is spread out in the cladding.

An alternative approach is to add *excitation sources* to the original problem, i.e. incident fields that excite the modes of the waveguide. This is a *source-driven* problem

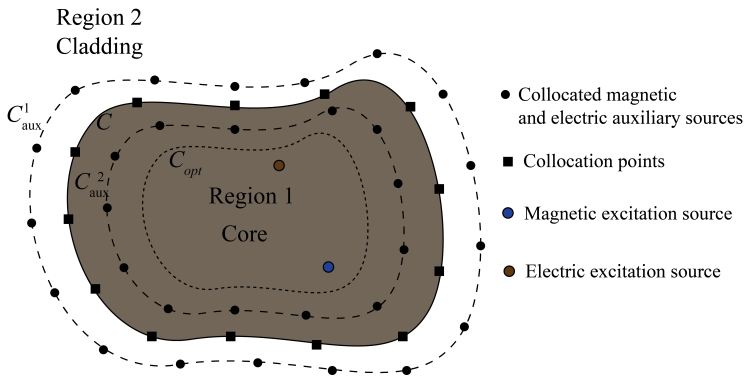

FIGURE 5.2: Application of MAS-TES for a cylindrical waveguide with an arbitrary cross section of its core and infinite cladding.

which is closely related to the scattering problem by the dielectric core.

Since the modes are hybrid, the sources are required to generate a combination of TM_z and TE_z fields. Thus, *two internal excitation sources* must be used, i.e., two z-directed current filaments lying inside the core. The one filament carries an electric current and radiates a TM_z field and the other a magnetic current and radiates a TE_z field, as shown in Fig. 5.2.

The *scattered* field $(\mathbf{E}_1, \mathbf{H}_1)$ in the core and the *transmitted* field $(\mathbf{E}_2, \mathbf{H}_2)$ in the cladding satisfy the homogeneous Helmholtz equations (5.4), as in the non-driven problem, as well as the following *inhomogeneous boundary conditions* on C

$$\hat{\mathbf{n}} \times (\mathbf{E}_1 - \mathbf{E}_2) = -\hat{\mathbf{n}} \times \mathbf{E}_{\text{inc}}, \tag{5.7}$$

$$\hat{\mathbf{n}} \times (\mathbf{H}_1 - \mathbf{H}_2) = -\hat{\mathbf{n}} \times \mathbf{H}_{\text{inc}}, \tag{5.8}$$

where $\hat{\mathbf{n}}$ is the normal unit vector to the boundary C. Similarly to the source-free problem, satisfying the boundary conditions (5.7) and (5.8) requires generally both TM_z and TE_z fields (namely both E_z and H_z components). The rest of the analysis proceeds as in the source-free problem above.

5.3 MAS with Two Excitation Sources

5.3.1 Dielectric Waveguide with Infinite Cladding

As in the original problem described in Section 5.2, there are also two possible approaches when applying the MAS in mode analysis of a dielectric waveguide. In the standard MAS approach, an equivalent to the source-free problem is formulated and solved [47], [80], [81]. A homogeneous linear system is obtained with unknowns the electric and magnetic auxiliary current amplitudes. The eigenvalues are then detected by the roots of the determinant of the impedance matrix $Z(\beta)$ computed by plotting $\det[Z(\beta)]$ for a fine grid of β in the range of (5.6) and determining the obtained local minima.

A second MAS approach, which we develop here and refer to it as the *Method of Auxiliary Sources with Two Excitation Sources* (MAS-TES) is related to the source-driven problem. The application of MAS-TES for a cylindrical waveguide with arbitrarily-shaped core is illustrated in Fig. 5.2. Two z-directed and infinitely-long sources are placed inside the core, carrying an electric and a magnetic current filament with amplitudes

$$I = I_0 e^{-\mathrm{i}\beta z}, \; K = K_0 e^{-\mathrm{i}\beta z}. \tag{5.9}$$

The $e^{-\mathrm{i}\beta z}$ dependence is used to excite propagating modes along z instead of a standing wave in the whole waveguide (as in the PEC case).

The longitudinal and transverse components of the field radiated from the electric current filament are

$$\mathbf{E}_z^e = -\frac{k_{\rho_1}^2 I}{4\omega\epsilon_1} H_0^{(2)}(k_{\rho_1} R_l)\hat{\mathbf{z}}, \tag{5.10a}$$

$$\mathbf{E}_t^e = -\frac{2\beta k_{\rho_1} I}{4\omega\epsilon_1} \frac{(x-x_e)\hat{\mathbf{x}} + (y-y_e)\hat{\mathbf{y}}}{R_l} H_1^{(2)}(k_{\rho_1} R_e), \tag{5.10b}$$

$$\mathbf{H}_t^e = \frac{2k_{\rho_1} I}{4} \frac{(y-y_e)\hat{\mathbf{y}} - (x-x_e)\hat{\mathbf{x}}}{R_e} H_1^{(2)}(k_{\rho_1} R_e), \tag{5.10c}$$

while those from the magnetic current filament are

$$\mathbf{H}_z^m = \frac{-k_{\rho_1}^2 K}{4\omega\mu_0} H_0^{(2)}(k_{\rho_1} R_m)\hat{\mathbf{z}}, \tag{5.11a}$$

$$\mathbf{H}_t^m = -\frac{2\beta k_{\rho_1} K}{4\omega\mu_0} \frac{(x-x_m)\hat{\mathbf{x}} + (y-y_m)\hat{\mathbf{y}}}{R_m} H_1^{(2)}(k_{\rho_1} R_m), \tag{5.11b}$$

$$\mathbf{E}_t^m = -\frac{2k_{\rho_1} K}{4} \frac{(y-y_m)\hat{\mathbf{y}} - (x-x_m)\hat{\mathbf{x}}}{R_m} H_1^{(2)}(k_{\rho_1} R_m). \tag{5.11c}$$

The subscript t denotes transverse components, $\boldsymbol{\rho} = (x, y)$ is the radial observation vector in the core, $\boldsymbol{\rho}_e = (x_e, y_e)$ and $\boldsymbol{\rho}_m = (x_m, y_m)$ are the radial vectors of the electric and magnetic current filaments, $R_e = |\boldsymbol{\rho} - \boldsymbol{\rho}_e|$ and $R_m = |\boldsymbol{\rho} - \boldsymbol{\rho}_m|$ are the corresponding distances, $H_0^{(2)}$ and $H_1^{(2)}$ are the second-kind Hankel functions of zeroth and first orders, respectively.

According to the MAS-TES numerical scheme, the scattered field in R_1 is simulated by the fields due to a set of N electric and N magnetic ($2N$ in total) z-directed current filaments. These filaments are distributed as coincident pairs (two collocated current sources) on an auxiliary surface C_{aux}^1, enclosing the boundary C, and radiate in an unbounded space filled by the material of R_1. Since the scattered field corresponds to a *propagating* hybrid mode, the current amplitudes must also have an $e^{-\mathrm{i}\beta z}$ dependence, i.e.,

$$I_l^{(1)} = I_{0l}^{(1)} e^{-\mathrm{i}\beta z},\ K_l^{(1)} = K_{0l}^{(1)} e^{-\mathrm{i}\beta z}, \tag{5.12}$$

with $l = 1, 2, \ldots, N$ being the index of the auxiliary current. Similarly, the transmitted field in R_2 is simulated by the field due to a set of N electric and N magnetic current filaments distributed on an auxiliary surface C_{aux}^2 placed inside the core and radiating in an unbounded space filled by the material of R_2. The corresponding current amplitudes are given by

$$I_l^{(2)} = I_{0l}^{(2)} e^{-\mathrm{i}\beta z},\ K_l^{(2)} = K_{0l}^{(2)} e^{-\mathrm{i}\beta z}. \tag{5.13}$$

The components of the radiated field from an auxiliary electric current filament are

$$\mathbf{E}_{zl}^{e,s} = -\frac{k_{\rho_s}^2 I_l^s}{4\omega\epsilon_s} H_0^{(2)}(k_{\rho_s} R_l)\hat{\mathbf{z}}, \tag{5.14a}$$

$$\mathbf{E}_{tl}^{e,s} = -\frac{2\beta k_{\rho_s} I_l^s}{4\omega\epsilon_s} \frac{(x-x_l)\hat{\mathbf{x}} + (y-y_l)\hat{\mathbf{y}}}{R_l} H_1^{(2)}(k_{\rho_s} R_l), \tag{5.14b}$$

$$\mathbf{H}_{tl}^{e,s} = \frac{2k_{\rho_s} I_l^s}{4} \frac{(y-y_l)\hat{\mathbf{y}} - (x-x_l)\hat{\mathbf{x}}}{R_l} H_1^{(2)}(k_{\rho_s} R_l), \tag{5.14c}$$

while those radiated from an auxiliary magnetic current are

$$\mathbf{H}_{zl}^{m,s} = \frac{-k_{\rho_s}^2 K_l^s}{4\omega\mu_0} H_0^{(2)}(k_{\rho_s} R_l)\hat{\mathbf{z}}, \tag{5.15a}$$

$$\mathbf{H}_{tl}^{m,s} = -\frac{2\beta k_{\rho_s} K_l^s}{4\omega\mu_0} \frac{(x-x_l)\hat{\mathbf{x}} + (y-y_l)\hat{\mathbf{y}}}{R_l} H_1^{(2)}(k_{\rho_s} R_l), \tag{5.15b}$$

$$\mathbf{E}_{tl}^{m,s} = -\frac{2k_{\rho_s} K_l^s}{4} \frac{(y-y_l)\hat{\mathbf{y}} - (x-x_l)\hat{\mathbf{x}}}{R_l} H_1^{(2)}(k_{\rho_s} R_l), \tag{5.15c}$$

where $s = (1), (2)$ for regions 1 and 2, $\boldsymbol{\rho}_l = (x_l, y_l)$ the radial position vector of the l-th source, $\boldsymbol{\rho} = (x, y)$ the observation vector, and $R_l = |\boldsymbol{\rho} - \boldsymbol{\rho}_l|$ the corresponding distance.

Next, we apply the boundary conditions (5.7) and (5.8) at N collocation points on C, with $\mathbf{E}_s$ ($\mathbf{H}_s$) the total electric (magnetic) field radiated by the auxiliary sources on C_{aux}^s, for $s = 1, 2$, and $\mathbf{E}_{inc}$ ($\mathbf{H}_{inc}$) the incident electric (magnetic) field. In this way, we obtain a system of the form

$$[Z]\mathbf{I} = \mathbf{V}, \tag{5.16}$$

where $\mathbf{I}$ is a $4N \times 1$ column vector consisting of the unknown complex amplitudes of the electric and magnetic filaments, and $\mathbf{V}$ is a $4N \times 1$ column vector with elements the samples of the tangential components of the electric and magnetic incident fields, while $[Z]$ is the $4N \times 4N$ matrix

$$Z = \begin{bmatrix} E_z^{1,e} & 0 & E_z^{2,e} & 0 \\ 0 & H_z^{1,m} & 0 & H_z^{2,m} \\ E_t^{1,e} & E_t^{1,m} & E_t^{2,e} & E_t^{2,m} \\ H_t^{1,e} & H_t^{1,m} & H_t^{2,e} & H_t^{2,m} \end{bmatrix} \tag{5.17}$$

where each $N \times N$ submatrix consists of the fields' samples, given by (5.14) and (5.15), at the N collocation points.

Solving the system (5.16) yields the $4N$ auxiliary current amplitudes from which we can compute the fields in the core and the cladding by using (5.14) and (5.15). A propagating mode corresponds to a standing wave in the core and an evanescent wave in the cladding. Thus, the eigenvalues can be detected by measuring the field inside the core, i.e., the response of the core to the excitation sources. This is measured by the response function $F(\beta)$ defined as

$$F(\beta) = \frac{1}{\zeta_1} \sqrt{\sum_{n=1}^{N_t} \frac{|\mathbf{E}_1(\boldsymbol{\rho}_n, \beta)|^2}{N_t}} + \sqrt{\sum_{n=1}^{N_t} \frac{|\mathbf{H}_1(\boldsymbol{\rho}_n, \beta)|^2}{N_t}} \tag{5.18}$$

where $\mathbf{E}_1$ ($\mathbf{H}_1$) is the scattered electric (magnetic) field in the transverse cross section of the waveguide, $\zeta_1 = \sqrt{\mu_0/\epsilon_1}$ the wave impedance of R_1 and $\boldsymbol{\rho}_n$ the positions of N_t randomly-selected sampling points in R_1. The random selection of the points reduces the probability of selecting nodal positions of the standing wave (i.e., zero-field points) that would yield small values of $F(\beta)$. Plotting $F(\beta)$ for a dense set of β, in the range of (5.6), yields a response curve the peaks of which correspond to the eigenvalues β.

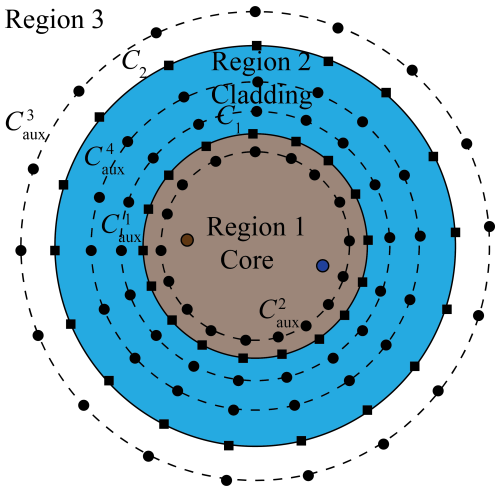

FIGURE 5.3: Application of MAS-TES for a multimode dielectric waveguide with a circular cross section.

5.3.2 Multimode Dielectric Waveguide

Dielectric waveguides in which the thickness of the cladding and the core are comparable are called multimode because they can support a large number of modes at a specific frequency. The cross section of such a waveguide with a circular boundary is depicted in Fig. 5.3; the third region R_3 is characterized by refractive index n_3 and permittivity ε_3.

Both excitation sources are placed at random positions inside the core. Now, the application of MAS-TES requires four auxiliary surfaces. The fields in R_1, R_2, and R_3 are simulated by the fields due to N electric and N magnetic current filaments placed on the auxiliary surfaces C^1_{aux}, C^2_{aux} and C^3_{aux}, and C^4_{aux}, respectively. The transmission conditions on the two boundaries C_1 and C_2 have the form

$$\hat{\mathbf{n}}_1 \times (\mathbf{E}_1 - \mathbf{E}_2) = -\hat{\mathbf{n}}_1 \times \mathbf{E}_{\text{inc}}, \tag{5.19a}$$

$$\hat{\mathbf{n}}_1 \times (\mathbf{H}_1 - \mathbf{H}_2) = -\hat{\mathbf{n}}_1 \times \mathbf{H}_{\text{inc}}, \tag{5.19b}$$

$$\hat{\mathbf{n}}_2 \times (\mathbf{E}_2 - \mathbf{E}_3) = \mathbf{0}, \tag{5.19c}$$

$$\hat{\mathbf{n}}_2 \times (\mathbf{H}_2 - \mathbf{H}_3) = \mathbf{0}, \tag{5.19d}$$

where $\hat{\mathbf{n}}_1$ and $\hat{\mathbf{n}}_2$ are the normal unit vectors on C_1 and C_2, $\mathbf{E}_s$ and $\mathbf{H}_s$ are the electric and magnetic fields generated in each region R_s, for $s = 1, 2, 3$. Applying these boundary conditions at N collocation points on C_1 and C_2, an $8N \times 8N$ linear system is obtained with unknowns the $8N$ electric and magnetic auxiliary current amplitudes. Solving this system, we compute the scattered fields in R_1, and then plot the response function $F(\beta)$ for a dense set of β in the range of (5.6). The peaks of the obtained response curve correspond to the propagation constants of the modes.

5.4 The Circular Dielectric Waveguide Excited by Two Sources

In this section, we analyze the scattering problem of a dielectric waveguide, composed of a circular core of radius a and an infinite cladding, excited by two sources in the core. The reason for this analysis is to demonstrate how the source-driven problem yields the eigenvalues.

The electric and magnetic current filaments are placed inside the core at positions $\boldsymbol{\rho}_e$ and $\boldsymbol{\rho}_m$, respectively. Their radiated fields are given by (5.10) and (5.11). The z-components of the scattered field in the core R_1 are expressed by

$$E_z^{\text{sc}}(\rho,\phi,z) = e^{-\mathrm{i}\beta z}\sum_{n=-\infty}^{+\infty} A_n^s J_n(k_{\rho_1}\rho)e^{\mathrm{i}n\phi}, \tag{5.20a}$$

$$H_z^{\text{sc}}(\rho,\phi,z) = e^{-\mathrm{i}\beta z}\sum_{n=-\infty}^{+\infty} B_n^s J_n(k_{\rho_1}\rho)e^{\mathrm{i}n\phi}, \tag{5.20b}$$

while the corresponding components of the transmitted field in the cladding are expressed by

$$E_z^{\text{tr}}(\rho,\phi,z) = e^{-\mathrm{i}\beta z}\sum_{n=-\infty}^{+\infty} A_n K_n(-\mathrm{i}k_{\rho_2}\rho)e^{\mathrm{i}n\phi}, \tag{5.21a}$$

$$H_z^{\text{tr}}(\rho,\phi,z) = e^{-\mathrm{i}\beta z}\sum_{n=-\infty}^{+\infty} B_n K_n(-\mathrm{i}k_{\rho_2}\rho)e^{\mathrm{i}n\phi}, \tag{5.21b}$$

where K_n is the modified Bessel function of the second kind which is related to the Hankel function of the second kind by

$$K_n\left(-\mathrm{i}k_{\rho_2}\rho\right) = -\frac{\pi}{2}\mathrm{i}^{n+1}H_n^{(2)}(k_{\rho_2}\rho) \tag{5.22}$$

and it is used in the expressions, so the transmitted field goes to zero at infinity (it is reminded that k_{ρ_2} is purely imaginary with a negative imaginary part). The other components of the fields in the core and the cladding are obtained by means of the z-components of the electric and magnetic fields.

Next, we apply the transmission conditions for the electric and magnetic fields' tangential components at $\rho = a$

$$E_z^{\text{sc}} - E_z^{\text{tr}} = -E_z^{\text{inc}}, \quad E_\phi^{\text{sc}} - E_\phi^{\text{tr}} = -E_\phi^{\text{inc}}, \tag{5.23a}$$

$$H_z^{\text{sc}} - H_z^{\text{tr}} = -H_z^{\text{inc}}, \quad H_\phi^{\text{sc}} - H_\phi^{\text{tr}} = -H_\phi^{\text{inc}}, \tag{5.23b}$$

and obtain a linear system with respect to the Fourier coefficients A_n, B_n and A_n^s, B_n^s of the transmitted and scattered fields. The matrix of this system is given by (A.5). The determinant of the matrix (A.6) is found to be

$$[Z] = \begin{bmatrix} J_n(k_{\rho_1}\alpha) & 0 & -K_n(-\mathrm{i}k_{\rho_2}\alpha) & 0 \\ 0 & J_n(k_{\rho_1}\alpha) & 0 & -K_n(-\mathrm{i}k_{\rho_2}\alpha) \\ \frac{\beta n}{k_{\rho_1}^2\alpha}J_n(k_{\rho_1}\alpha) & \frac{\mathrm{i}\Gamma_0}{k_{\rho_1}}J_n'(k_{\rho_1}\alpha) & -\frac{\beta n}{k_{\rho_2}^2\alpha}K_n(-\mathrm{i}k_{\rho_2}\alpha) & \frac{\omega\mu_0 k_{\rho_2}}{\beta}K_n'(-\mathrm{i}k_{\rho_2}\alpha) \\ \frac{-\mathrm{i}\omega\epsilon_1}{k_{\rho_1}}J_n'(k_{\rho_1}\alpha) & \frac{\beta n}{k_{\rho_1}^2\alpha}J_n(k_{\rho_1}\alpha) & \frac{\omega\epsilon_2}{k_{\rho_2}}K_n'(-\mathrm{i}k_{\rho_2}\alpha) & -\frac{\beta n}{k_{\rho_2}^2\alpha}K_n(-\mathrm{i}k_{\rho_2}\alpha) \end{bmatrix} \tag{5.24}$$

$$D(\beta) = \left[\frac{J_n'(k_{\rho_1}\alpha)}{k_{\rho_1}\alpha J_n(k_{\rho_1}\alpha)} + \frac{K_n'(-\mathrm{i}k_{\rho_2}\alpha)}{-\mathrm{i}k_{\rho_2}\alpha K_n(-\mathrm{i}k_{\rho_2}\alpha)}\right] \times \left[n_1^2\frac{J_n'(k_{\rho_1}\alpha)}{k_{\rho_1}\alpha J_n(k_{\rho_1}\alpha)} + n_2^2\frac{K_n'(-\mathrm{i}k_{\rho_2}\alpha)}{-\mathrm{i}k_{\rho_2}\alpha K_n(-\mathrm{i}k_{\rho_2}\alpha)}\right] - \frac{\beta^2 n^2}{k_0^2}\left[\frac{1}{k_{\rho_1}^2\alpha^2} - \frac{1}{k_{\rho_2}^2\alpha^2}\right]^2. \tag{5.25}$$

The roots of the determinant (5.25) correspond to the eigenvalues β of the dielectric waveguide; see, e.g., [60]. The unknown Fourier coefficients A_n, B_n and A_n^s, B_n^s are calculated by solving the system of (5.23) and in the obtained expressions of these coefficients the determinant $D(\beta)$ appears in all the denominators. Hence, when β equals an eigenvalue, these coefficients go to infinity and so does the scattered field given by (5.20). So, a plot of the response function $F(\beta)$ for a dense set of β will showcase highly visible peaks corresponding to the eigenvalues of the waveguide.

5.5 Numerical Results

In Section 5.4, we analyze the problem of a circular dielectric waveguide excited by two sources. In this section, we investigate numerically more general cases by presenting results for the application of MAS-TES in five geometries of dielectric waveguides. In the first four examples, the cladding is considered to be of infinite extent. The last example corresponds to a multimode waveguide, where the cladding has similar dimensions with the core. Specifically, we investigate the cases of circular, elliptical, rounded-triangular and inverted-elliptical cores, while the multimode dielectric waveguide has a concentric-circular shape. For each case, the refractive index of the core is $n_1 = 1.8$ and the refractive index of the cladding is $n_2 = 1.5$. The free space wavenumber is $k_0 = 1$ m^{-1}, and hence from (5.6) follows that the propagation constants β lie in the interval $1.5 < \beta < 1.8$. All coordinates in the following results are in meters. Besides, hereafter, N is the number of each set of the electric and magnetic auxiliary sources and collocation points, N_g is the number of plot points in the response curve and N_t is the number of measurement points used for the response function $F(\beta)$. Regarding the choices of the parameters N, N_g and N_t, we note that in the considered numerical experiments their values were chosen such that response curves with highly-visible peaks are generated. Specifically, we performed systematic convergence checks for each waveguide's geometry and estimated the thresholds below which the eigenvalues are undetectable. For N and N_t, a further increase above these thresholds, does not have a noticeable effect in the significant digits of the computed eigenvalues. However, the number N_g of plot points affects more crucially the computation of the eigenvalues. Still, for all examined geometries, the choice $N_g \geq 1000$ guarantees convergence of the computed eigenvalues within the desired number of digits. Indicatively, for the elliptical waveguide, when $N > 28$, $N_t > 5$, and $N_g > 1000$, no significant changes in the eigenvalues are observed.

All the MAS-TES results are compared with those obtained by the FEM-based commercial software COMSOL Multiphysics as well as by the method computing the zeros of the determinant of the impedance matrix $Z(\beta)$ of the standard MAS approach. For the latter method, we defined the function $L(\beta) = \ln[|\det(Z(\beta))|]$, i.e., the logarithm of the absolute value of the impedance matrix determinant.

5.5.1 Circular Core

We consider a dielectric waveguide with a circular core of radius $\rho_c = \lambda_0/2$ and an infinitely-extended cladding; see Fig. 5.4. The electric and magnetic excitation sources are placed inside the core at $(x_e, y_e) = (0, 0)$ and $(x_m, y_m) = (1.5, 0)$, respectively. The external (internal) auxiliary surface C^1_{aux} (C^2_{aux}) is a circle of radius $\rho_e = 2\rho_c$ ($\rho_i = 0.5\rho_c$). We apply the MAS-TES for $N = 24$, $N_g = 1000$ and $N_t = 20$ and obtain the response curve of Fig. 5.5. The results do not include discrete and continuous spurious solutions in contrast to the plot of $L(\beta)$, of the standard MAS approach, depicted also in Fig. 5.5. Table I shows the eigenvalues of the modes obtained analytically (exact solutions) together with the results extracted by MAS-TES and FEM. An excellent agreement is observed.

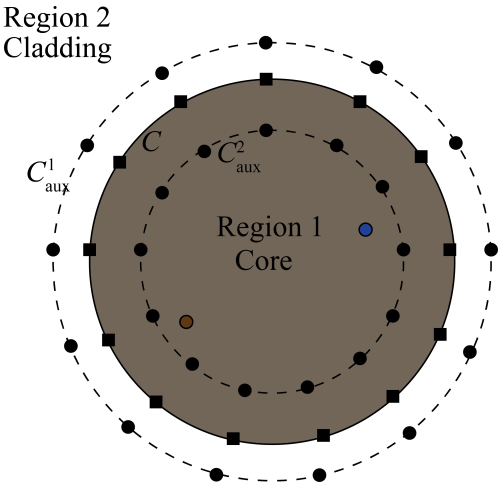

FIGURE 5.4: Application of MAS-TES for a dielectric waveguide with circular core.

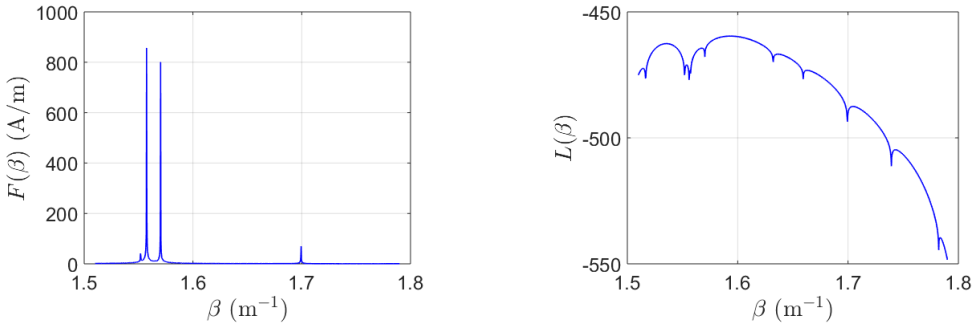

FIGURE 5.5: Eigenvalues of the waveguide with circular core as obtained by the MAS-TES (left panel) and the determinant method (right panel).

5.5.2 Elliptical Core

As a second example, we investigate a dielectric waveguide with an elliptical core and infinitely-extended cladding, as shown in Fig. 5.6. The elliptical core has large semiaxis $a = \lambda_0/2$ and small semiaxis $b = 0.8a$. The excitation sources lie at $(x_e, y_e) = (1.2, -0.8)$ and $(x_m, y_m) = (1.2, 0.8)$. The coordinates of the external auxiliary curve C^1_{aux} are $(x_{\text{a1}}, y_{\text{a1}}) = 2(x_{\text{c}}, y_{\text{c}})$ and of the internal auxiliary curve C^2_{aux}

modes	Exact	MAS-TES	FEM
1	1.552	1.552	1.551
2	1.557	1.557	1.557
3	1.570	1.570	1.570
4	1.699	1.699	1.699

TABLE 5.1: Eigenvalues of a dielectric waveguide with circular core as obtained analytically (exact solutions), by the MAS-TES, and by the FEM

are $(x_{a2}, y_{a2}) = 0.5(x_c, y_c)$, where (x_c, y_c) is the elliptical boundary C. For $N = 30$, $N_g = 1000$ and $N_t = 20$, we obtain the response curve of Fig. 5.7. Again, no discrete or continuous spurious solutions are observed such as those detected by standard MAS. In Table II, the eigenvalues of the modes obtained by MAS-TES and FEM are depicted, and an excellent agreement is observed.

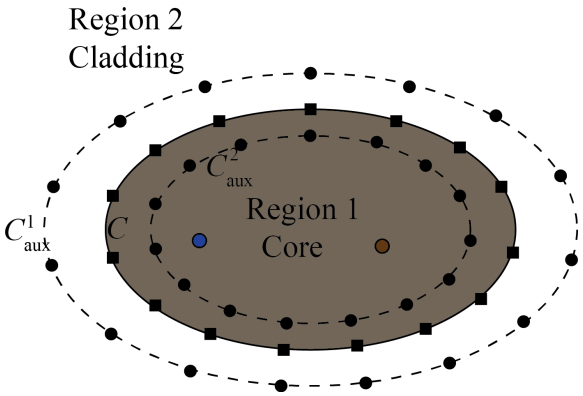

FIGURE 5.6: Application of MAS-TES for a dielectric waveguide with elliptical core.

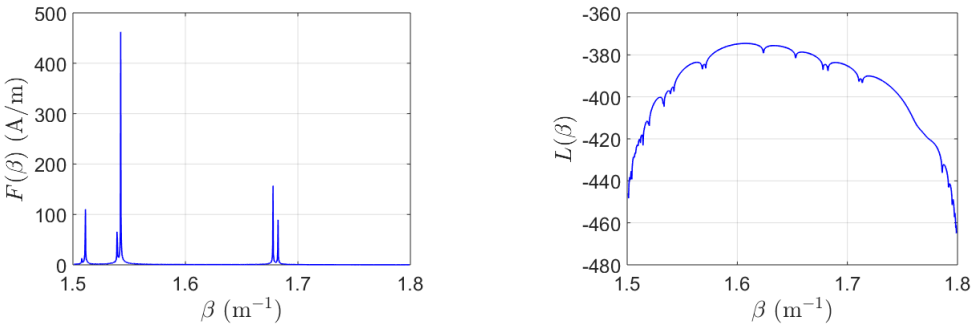

FIGURE 5.7: Eigenvalues of the waveguide with elliptical core as obtained by MAS-TES (left panel) and the determinant method (right panel).

modes	MAS-TES	FEM
1	1.508	1.508
2	1.511	1.511
3	1.539	1.539
4	1.542	1.543
5	1.678	1.678
6	1.682	1.682

TABLE 5.2: Eigenvalues of a dielectric waveguide with elliptical core as obtained by MAS-TES and FEM

5.5.3 Rounded-Triangular Core

Next, we seek the eigenvalues of a waveguide with rounded-triangular core and infinitely-extended cladding as in Fig. 5.8. The parametric equations of the triangular boundary are

$$x_c = 1.75(\cos\varphi + 0.1\cos(2\varphi)),$$
$$y_c = 1.75(\sin\varphi - 0.1\sin(2\varphi)).$$

The electric excitation source is placed at $(x_e, y_e) = (-0.7, -0.3)$ and the magnetic source at $(x_m, y_m) = (1.1, 1.1)$. The external auxiliary curve C^1_{aux} is located at $(x_{a1}, y_{a1}) = 1.3(x_c, y_c)$, while the internal one C^2_{aux} at $(x_{a2}, y_{a2}) = 0.7(x_c, y_c)$. In this case, we choose $N = 40$, $N_g = 1000$, and $N_t = 20$, which results to the response curve of Fig. 5.9. Only one eigenvalue, $\beta = 1.582$, is detected for this geometry by MAS-TES and coincides with that computed by FEM. Standard MAS on the other hand detects several discrete spurious solutions.

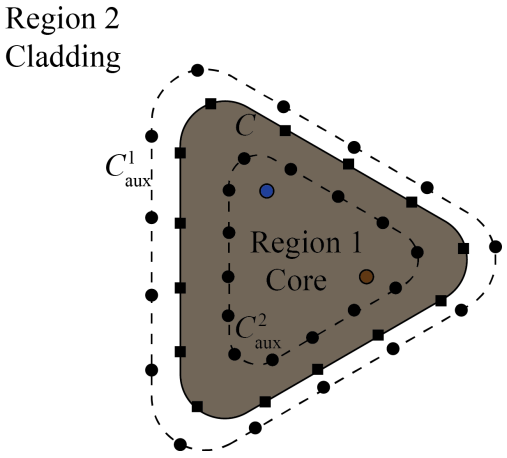

FIGURE 5.8: Application of MAS-TES for a dielectric waveguide with rounded-triangular core.

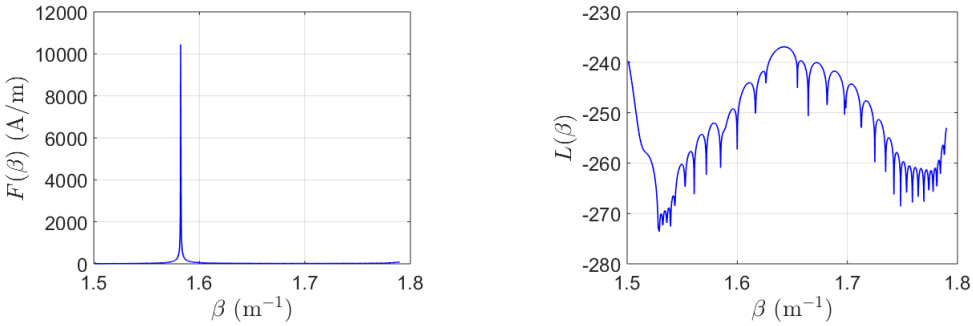

FIGURE 5.9: Eigenvalues of the waveguide with rounded-triangular core as obtained by MAS-TES (left panel) and the determinant method (right panel).

5.5.4 Inverted-Elliptical Core

Moreover, we examine an inverted-elliptical core surrounded by an infinitely-extended cladding, as shown in Fig. 5.10. The coordinates of the core's boundary are

$$x_c = 1.884\frac{1.3\cos\varphi}{1+0.6\cos 2\varphi + 0.09},$$
$$y_c = 1.884\frac{0.7\sin\varphi}{1+0.6\cos 2\varphi + 0.09}.$$

The excitation sources are placed at $(x_e, y_e) = (0.5, 1.5)$ and $(x_m, y_m) = (0.4, -1)$ inside the core. The external auxiliary curve C^1_{aux} lies at $(x_{\text{a1}}, y_{\text{a1}}) = 1.3(x_{\text{c}}, y_{\text{c}})$, while the internal one C^2_{aux} at $(x_{\text{a2}}, y_{\text{a2}}) = 0.7(x_{\text{c}}, y_{\text{c}})$. Here, $N = 48$, $N_g = 1000$ and $N_t = 10$ yielding the response curve of Fig. 5.11. In Table III, the two eigenvalues detected by MAS-TES and FEM are shown. In contrast, the standard MAS detects many spurious solutions.

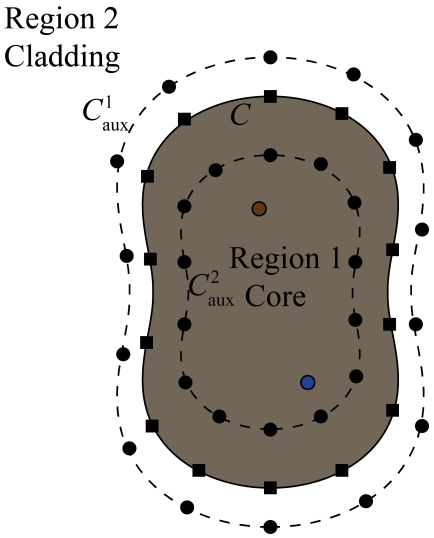

FIGURE 5.10: Application of MAS-TES for a dielectric waveguide with inverted-elliptical core.

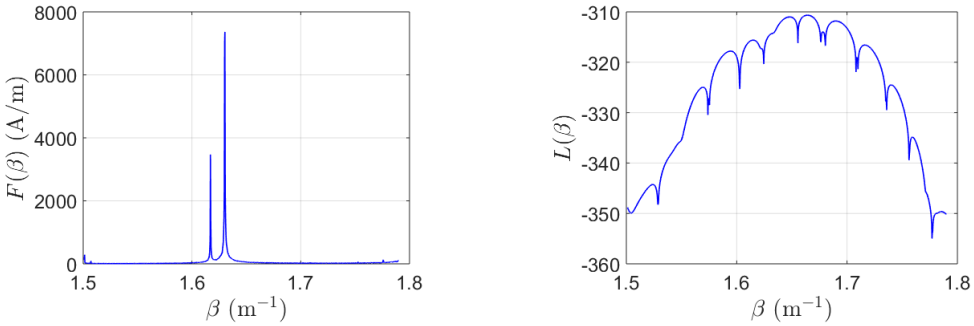

FIGURE 5.11: Eigenvalues of the waveguide with rounded triangular core as obtained by the repsponse function method (left panel) and the determinant method (rigth panel).

modes	MAS-TES	FEM
1	1.617	1.617
2	1.630	1.630

TABLE 5.3: Eigenvalues of a dielectric waveguide with inverted-elliptical core as obtained by MAS-TES and FEM

5.5.5 Circular Multimode Waveguide

Next, we examine a case of a multimode waveguide. The whole structure is surrounded by region R_3, which is filled with air. Both the core and the cladding have circular boundaries with radii $\rho_1 = 0.75\lambda_0$ and $\rho_2 = \lambda_0$, as illustrated in Fig. 5.3. The electric and magnetic excitation sources are placed inside the core at $(x_e, y_e) = (-0.7, -0.3)$ and $(x_m, y_m) = (1.1, 1.1)$. For this case, four auxiliary curves are defined with their radii being $\rho_{\text{aux}}^{(1)} = 2\rho_1, \rho_{\text{aux}}^{(2)} = 0.5\rho_1, \rho_{\text{aux}}^{(3)} = 2\rho_2$ and $\rho_{\text{aux}}^{(4)} = 0.5\rho_2$. Each of these auxiliary curves hosts two sets of $N = 24$ electric and magnetic auxiliary sources. For $N_g = 1000$ and $N_t = 20$, we obtain the response curve Fig. 5.12. It is obvious that many modes are supported by this waveguide. Again, MAS-TES detects accurately all eigenvalues as opposed to the standard MAS. The first six eigenvalues as obtained by MAS-TES and FEM are shown in Table IV and an excellent agreement is observed.

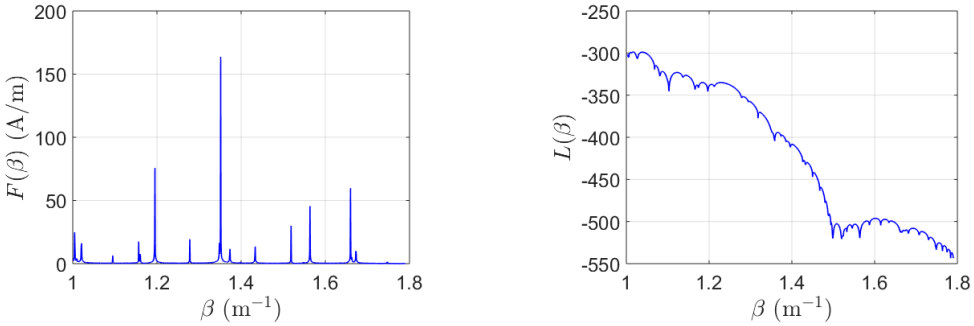

FIGURE 5.12: Eigenvalues of the multimode waveguide as obtained by MAS-TES (left panel) and the determinant method (right panel).

modes	MAS-TES	FEM
1	1.004	1.005
2	1.010	1.010
3	1.020	1.021
4	1.095	1.095
5	1.157	1.157
6	1.160	1.160

TABLE 5.4: Eigenvalues of a multimode waveguide with circular core as obtained by MAS-TES and FEM

5.5.6 Elliptical Multimode Waveguide

A more complex geometry of a multimode dielectric waveguide is illustrated in Fig. 5.13. The core has an elliptic boundary C_1 with large semiaxis $a_1 = 0.8\lambda_0$ and small semiaxis $b_1 = 0.7\lambda_0$ corresponding to coordinates (x_1, y_1). The cladding has also an elliptical boundary C_2 with large semiaxis $a_2 = 1.2\lambda_0$ and small semiaxis $b_2 = \lambda_0$ corresponding to coordinates (x_2, y_2). As in the circular multimode waveguide, we assume that the cladding is surrounded by region R_3 filled with air. The electric excitation source is placed at $(x_e, y_e) = (0, 0)$ and the magnetic source at $(x_m, y_m) = (1.5, 0.8)$. Four elliptically shaped auxiliary curves are considered for which $(x^{(1)}_{\text{aux}}, y^{(1)}_{\text{aux}}) = 2(x_1, y_1)$, $(x^{(2)}_{\text{aux}}, y^{(2)}_{\text{aux}}) = 0.5(x_1, y_1)$, $(x^{(3)}_{\text{aux}}, y^{(3)}_{\text{aux}}) = 2(x_2, y_2)$, and $(x^{(4)}_{\text{aux}}, y^{(4)}_{\text{aux}}) = 0.5(x_2, y_2)$. Each of these curves hosts $N = 40$ pairs of electric and magnetic auxiliary sources, while an equal number of collocation points on C_1 and C_2 is employed. For $N_g = 1000$ and $N_t = 20$, the response curve of Fig. 5.14 is obtained. A large number of eigenvalues are supported without any spurious solutions being among them in contrast to the plot of $L(\beta)$. In Table V, the first six eigenvalues are compared with the ones acquired by applying FEM.

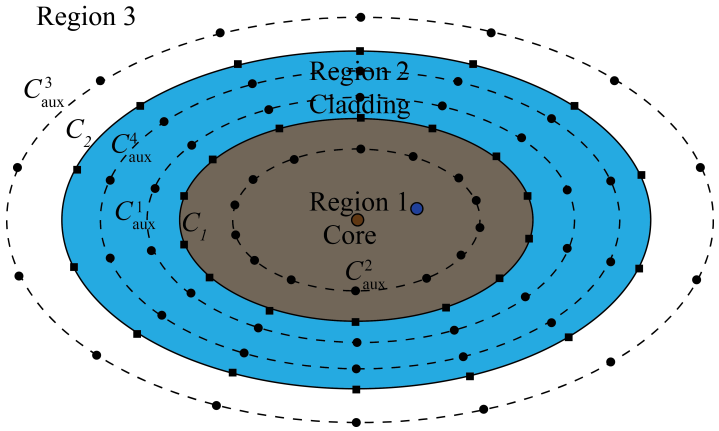

FIGURE 5.13: Application of MAS-TES on an elliptical concentric multimode dielectric waveguide.

5.5.7 Effect of the Locations of the Excitation and Auxiliary Sources

Regarding the effect of the excitation sources' locations on the computation of the eigenvalues, we note that in single mode waveguides numerical results showed that when either of the excitation sources is placed near the boundary C, a number of

,

modes	MAS-TES	FEM
1	1.011	1.010
2	1.013	1.013
3	1.026	1.025
4	1.044	1.043
5	1.060	1.059
6	1.088	1.087

TABLE 5.5: Eigenvalues of a multimode elliptical concentric dielectric waveguide

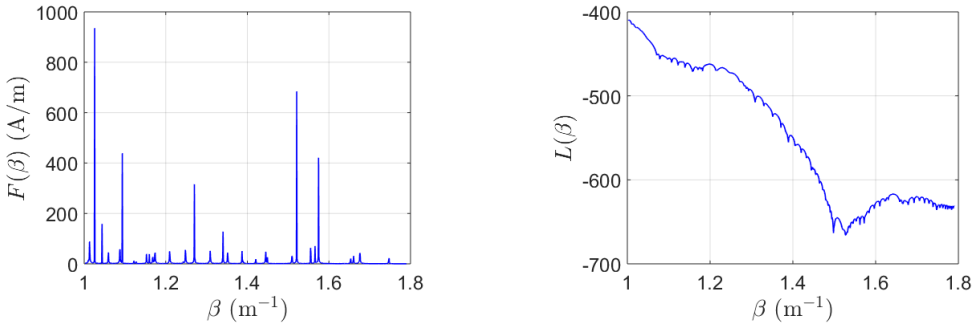

FIGURE 5.14: Eigenvalues of the elliptical multimode dielectric waveguide as obtained by the MAS-TES (left panel) and the determinant method (right panel).

spurious eigenvalues appear in the response curve of $F(\beta)$. However, as the excitation sources move toward the center of the core, these spurious solutions gradually vanish. A general rule that can be formulated for the single mode dielectric waveguides is that when the excitation sources are placed inside an *optimum curve* C_{opt}, which is a downscaled version of C with coordinates $0.6(x_c, y_c)$, then it is guaranteed that no spurious solutions appear in the response curve. Moreover, in multimode waveguides, extensive numerical experiments have revealed that there are no similar restrictions on the placement of the excitation sources inside the core. In multimode waveguides, even collocated excitation sources lying near the boundary C_1 yield the correct eigenvalues without the appearance of any spurious solutions.

Moreover, the auxiliary sources' locations affect the accuracy of the fields in the core, and, thus, also the eigenvalues determination. After systematic numerical investigations, we found that correct eigenvalues, without spurious solutions, are obtained for the following conditions per waveguide geometry:
Circular: $1.3\rho_c \leq \rho_e \leq 2\rho_c$, $0.5\rho_c \leq \rho_i \leq 0.7\rho_c$.
Elliptical: $1.3x_c \leq x_{a1} \leq 2.3x_c$, $1.3y_c \leq y_{a1} \leq 2.3y_c$, $0.3x_c \leq x_{a2} \leq 0.5x_c$, $0.3y_c \leq y_{a2} \leq 0.5y_c$.
Rounded triangular: $1.3x_c \leq x_{a1} \leq 2x_c$, $1.3y_c \leq y_{a1} \leq 2y_c$, $0.5x_c \leq x_{a2} \leq 0.7x_c$, $0.5y_c \leq y_{a2} \leq 0.7y_c$.
Inverted elliptical: $1.3x_c \leq x_{a1} \leq 1.4x_c$, $1.3y_c \leq y_{a1} \leq 1.4y_c$ $0.68x_c \leq x_{a2} \leq 0.7x_c$, $0.68y_c \leq y_{a2} \leq 0.7y_c$.

For the multimode waveguides, similar conditions hold with the corresponding single-mode ones.

5.6 Conclusions

The Method of Auxiliary Sources with an Excitation Source (MAS-ES) is a reliable method for mode analysis. Especially, for dielectric waveguides, two excitation sources are required to be placed appropriately inside the core in order to excite the propagating hybrid modes; this is what we here called MAS-TES. The eigenvalues are detected by measuring the fields inside the core by means of a response function the peaks of which correspond to the eigenvalues. Several numerical experiments for different geometries showed that all eigenvalues are accurately computed contrary to conventional MAS which detects also spurious eigenvalues. In future, we plan to extend this work to dielectric waveguides with anisotropic regions.

Chapter 6

Shielding Effectiveness of Ideal Monolayer Graphene in Cylindrical Configurations with the Method of Auxiliary Sources

6.1 Introduction

In today's technology-driven world, a plethora of electronic devices emitting electromagnetic (EM) waves are used [84]. In addition, there exist also natural sources of EM radiation such as lightnings, auroras and solar flares. Under these conditions, it is understood that an electronic device is continuously exposed to signals which are not related to its functionality causing what is known as Electromagnetic Interference (EMI) or Radio Frequency Interference (RFI) when the signals are in the RF spectrum (20 KHz-300 GHz). If care is not taken, this interference may lead to a performance degradation or even to destruction. Furthermore, excessive exposure to EM fields may cause health issues to several living organisms (including human beings) [85], [86].

An effective way of dealing with EMI is to use an EM shield, which usually refers to a structure that encloses completely an electronic device or a portion of that device. Shielding works partially by reflection of the incident wave and partly by absorption as the wave travels through the shielding material. For the past few decades, metals were employed as shielding materials, not only due to their high reflectivity but also because they provide attenuation to high-frequency waves [87]. However, metals are limited by their heavy weight, difficulty to process, low flexibility, and corrosion problems. Besides, metal-based shields are more than tens of microns in thickness and thus opaque, hence preventing the visibility of the device enclosed by the shield.

While carbon itself is not considered a metallic element, carbon-based materials, such as graphene, can offer remarkable EM shielding properties, mainly via the mechanism of absorption [88]. Advances in chemical vapor decomposition (CVD) growth of large-area and high-quality graphene [89] has already enabled its practical applications [90]. The high conductivity, saturation velocity, flexibility, optical transparency, resistance to corrosion, and mechanical strength of graphene make it an excellent choice for high-performance EMI shielding. Graphene is utilized in various forms for EMI shielding applications including mono and multi-layered graphene structures, and composites with different materials [91].

Considerable experimental work has demonstrated the suitability of graphene in EMI shielding. In [92], the shielding effectiveness (SE) of a true monolayer CVD

graphene was investigated in the frequency range 2.2-7 GHz, and was shown experimentally to have seven times (in terms of dB) greater SE than gold film; the developed theoretical model for ideal monolayer graphene predicted EMI shielding up to 97.8%. Composites based on incorporating graphene sheets into an epoxy matrix were tested in 8.2-12.4 GHz and a SE of 21 dB was obtained [93]. Porous graphene/polystyrene lightweight composites exhibited high values of SE [94]. In [95], large-sized graphene sheets and doping strategy were employed to fabricate lightweight and flexible graphene paper showing an exceptional SE of 47 dB at 8.4 GHz. In [96], a thin nanoribbon/polyvinyl alcohol composite was developed achieving an EMI shielding as high as 60 dB in 8.0-12.0 GHz.

Various analytical and numerical methods have been developed to compute the electromagnetic response of graphene [97]. Traditionally, graphene is modeled as a very thin 3-D material as in [98] as well as in commercial packages applying the Finite-Difference Time-Domain Method (FDTD) and the Finite Element Method (FEM) (Comsol Multiphysics, CST Studio). To achieve good numerical accuracy, a very fine mesh is needed to adequately discretize the thin graphene layer. This approach may become impracticable due to high requirements in terms of memory storage and computer time. To alleviate these requirements, the 3-D model is replaced by a suitable boundary condition. In [99], a conductive surface boundary condition was implemented in the FDTD method in combination with the dispersive surface conductivity of graphene. An impedance transmission boundary condition (ITBC) [100] and an impedance network boundary condition (INBC) [101] were also used to model thin layers of graphene into FEM. Moreover, a surface impedance boundary condition (SIBC) associated with graphene was incorporated in the Method of Moments in [102]. Also, in [103] and [104], an equivalent circuit model is proposed for graphene monolayer, which considers the conditional spatial dispersion of surface conductivity [105].

In this chpater, we apply MAS to compute the SE of an ideal monolayer graphene in the RF frequency range, when used as the conductive layer in cylindrical structures of arbitrary cross sections. The standard MAS approach encounters numerical difficulties in multilayered structures containing a highly conductive layer [106]; thus the same problems might occur with graphene. To deal with this, a modification of MAS is proposed by which the conductive layer is modeled as an Impedance Matrix Boundary Condition (IMBC) instead of a very thin conductive layer. In [107], [108], an 1-D IMBC is proposed for infinite planar conductive layers, while in [54] a 2-D IMBC is proposed considering the curvature of the conductive layer.

This chapter is organized as follows. Graphene's electronic and electromagnetic properties, emphasizing on its frequency dependent surface conductivity, are presented in 6.2. In 6.3, we describe the application of MAS in cylindrical multilayered configurations containing a highly-conductive layer. We explain why the standard approach of MAS is inadequate and how the modified MAS with an IMBC yields accurate results for the fields in the regions enclosed by the conductive layer. 6.4 contains numerical experiments testing the modified MAS. The fact that graphene can be easily deposited on glass [109], [110] enables us to study four cases of cylindrical shielding configurations where the shield consists of a graphene monolayer deposited on a silicon dioxide-SiO_2 (glass) substrate. Such a shield has the advantage of being optically transparent, non corrosive, and relatively light weighted, thus, it is potentially realizable. We also investigate the case of a Few Layer Graphene (FLG) shield, composed of three graphene layers (trilayer), which are a combination of a misoriented layer, and an AA-stacked double layer (bilayer). By applying the modified MAS, the graphene layer (or FLG) is replaced by a 2-D IMBC and the shielding

effectiveness is computed along with the scattered fields. The results for each investigated case are compared to those obtained by the FEM-based commercial software package.

An $\exp(\mathrm{i}\omega t)$ time dependence is assumed and suppressed throughout with $k = \omega/c = 2\pi f/c = \omega\sqrt{\epsilon_0\mu_0}$.

6.2 Electronic Properties of Graphene

6.2.1 Ideal Monolayer Graphene

Graphite is a mineral made from layers of carbon atoms arranged in a hexagonal structure. These layers are very weakly bonded together allowing the effortless mechanical exfoliation of few or many of them. For years, efforts were made to isolate a thermodynamically stable single atomically thin, graphite layer. This was finally achieved in 2004 giving birth to the first 2-D material called *graphene* [111], [112].

Graphene is a material with special mechanical and electronic properties originating from the unusual way the carbon atoms are bonded in the hexagonal lattice. Each carbon atom has six electrons surrounding its nucleus, two in the inner shell and four in the outer shell. The fourth electron in the outer shell has a π orbital and is delocalized, oriented perpendicular to the graphene layer. These delocalized electrons are responsible for the electrical conductivity of graphene.

The peculiarity of graphene's electrical conductivity is understood by studying the energy band structure of a delocalized electron in the lattice. What makes the energy band structure of *pure graphene* distinct from that of other materials (conductors, insulators and semiconductors) is that the energy band gap is zero meaning that the Fermi level E_F is exactly at the point where the conductive and the valence bands meet (also called Dirac point) and has a zero value. Hence, pure graphene can be characterized as a semiconductor with a zero-energy gap or a conductor with an empty valence band.

Just like in semiconductors, we can modify the conductivity of pure graphene by moving the Fermi level inside the conduction band or in the valence band. This can be accomplished by chemical doping, where a small number of carbon atoms in the graphene layer are replaced by a dopant atom yielding *doped graphene*. For n-doped graphene, E_F is increased moving in the conduction band, while for p-doped graphene, E_F moves in the valence band. The position of the Fermi level can also be tuned by applying a static electric field between graphene and a metallic layer called gate, separated by a thin insulator.

The surface conductivity of single-layer graphene is derived by the Kubo formula [113]

$$\sigma(\omega) = \frac{2e^2 k_B T}{\pi\hbar^2}\frac{\mathrm{i}}{\omega + \mathrm{i}\tau^{-1}}\ln\left(2\cosh\left(\frac{E_F}{2k_B T}\right)\right) + \frac{e^2}{4\hbar}\left(H(\omega/2) + \int_0^\infty \frac{H(\Omega) - H(\omega/2)}{\omega^2 - 4\Omega^2}d\Omega\right), \quad (6.1)$$

where e is the charge of the electron, k_B is the Boltzmann constant, τ is the Drude relaxation time of graphene (mean time between two successive collisions of electrons with carbon atoms), T is the absolute ambient temperature measured in Kelvins, $\hbar$ is the reduced Planck constant, ω is the radial frequency of the incident EM field

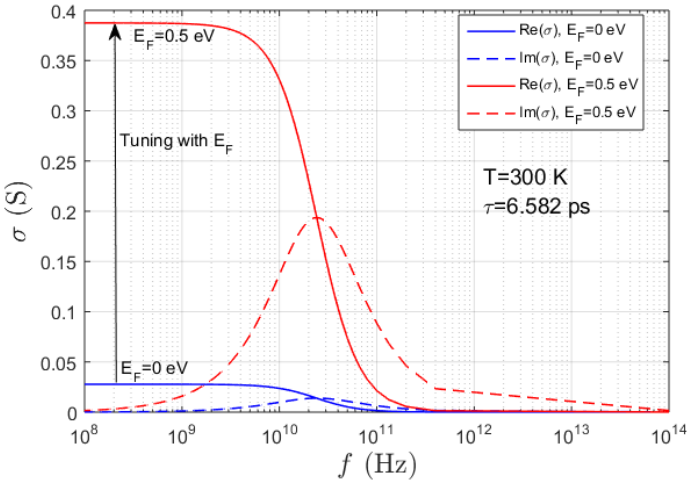

FIGURE 6.1: Real and imaginary parts of monolayer graphene surface conductivity versus frequency for two values of E_F.

(photons), while

$$H(\Omega) = \frac{\sinh(\hbar\Omega/k_BT)}{\cosh(\hbar\Omega/k_BT) + \cosh(E_F/k_BT)}. \tag{6.2}$$

The first term in (6.1) represents the intraband surface conductivity, and the second integral term the interband surface conductivity with the first one being dominant in the RF/microwave region. For this reason, in all the derivations and computations that follow, only the intraband surface conductivity is taken into account. Using the surface conductivity in the Maxwell equations, the equivalent complex permittivity of graphene is obtained

$$\varepsilon_g(\omega) = 1 - \frac{i\sigma(\omega)}{\omega\varepsilon_0\Delta}, \tag{6.3}$$

where Δ is the thickness of the graphene monolayer which is usually chosen equal to 0.5 nm [114], [115]. Notably, ideal monolayer graphene is intrinsically nonmagnetic and lacks magnetic moments due to the delocalized π-bonding network [116]. Thus, there appears no dispersion in graphene's magnetic permeability, which we consider to be that of vacuum, i.e., μ_0. The volumetric (bulk) conductivity of graphene is given by [117]

$$\sigma_V(\omega) = \frac{\sigma(\omega)}{\Delta}, \tag{6.4}$$

and is measured in S/m.

Figure 6.1 depicts the real and imaginary parts of the surface conductivity given by (6.1) at room temperature ($T = 300$K) and $\tau = 6.582$ ps (which corresponds to carrier scattering rate $\Gamma = 0.1$ meV) for different positive values of the Fermi level E_F with electrons as current carriers. Similar plots may be obtained for negative E_F with holes as current carriers. It is evident that graphene exhibits high surface conductivity in the RF region, which is *tunable* by changing the value of E_F.

It is worth to point out that although we are presenting the graphene planar model, we will use the same formulas for cylindrical (curved) geometries since for the structures of interest the number of carbon atoms exceed 10^4 [118], and the strain

due to bending the graphene monolayer does not cause any defects on the lattice.

Another improtant aspect of graphene's surface conductivity is its conditional spatial dispersion [105]. Specifically, a graphene sheet showcases a spatially dispersive conductivity when it is biased by a perpendicular static electric field, or by a static magnetic field via the Hall Effect.

6.2.2 Few Layer Graphene

The term graphene is not exclusively used for a single layer of carbon atoms bounded together in a honeycomb structure (graphene monolayer), but also for a material composed of a few of these layers stacked together. This structure is called *Few Layer Graphene* (FLG) or *Multi Layered Graphene* (MLG), and is also considered as a 2-D material. Specifically, according to ISO/TS 80004-13 [119], FLG is a 2-D material consisting of three to ten well-defined stacked graphene layers. Above ten layers, the material is referred to as graphite or micro-graphite, thus, it is not considered as graphene.

FLG can be misoriented multilayer graphene (frequently observed in CVD), AA-stacked, and AB-stacked (Bernal) [120]–[122]. In case of N layers of misoriented graphene, the surface conductivity from the RF up to the THz region is given by

$$\sigma_{mis}(\omega) = N \times \sigma(\omega) = N \frac{2e^2 k_B T}{\pi \hbar^2} \frac{\mathrm{i}}{\omega + \mathrm{i}\tau^{-1}} \ln\left(2\cosh\left(\frac{E_F}{k_B T}\right)\right). \tag{6.5}$$

The surface conductivity per layer of AA-stacked FLG is expressed by [121]

$$\sigma_{AA}(\omega) = \frac{2e^2 k_B T}{\pi \hbar^2 N} \frac{\mathrm{i}}{\omega + \mathrm{i}\tau^{-1}} \times \sum_{r=1}^{N} \ln\left(2\cosh\left\{\frac{E_F + 2a_1 \cos\left[\frac{r\pi}{N+1}\right]}{2k_B T}\right\}\right), \tag{6.6}$$

with $a_1 = 217$ meV. It is also possible that an FLG consists of misoriented layers as well as layers that are AA or AB stacked. For example, the surface conductivity of a graphene trilayer, which comprises of a two layer (bilayer) AA-stack and one misoriented monolayer, is given by

$$\sigma_{AAA'}(\omega) = 2 \times \sigma_{AA}(\omega)|_{N=2} + \sigma(\omega). \tag{6.7}$$

The permittivity and bulk conductivity are then calculated by (6.3) and (6.4), respectively, with thickness $\Delta_{AAA'} = 3\Delta = 1.5$ nm.

6.3 Shielding Effectiveness of a Conductive Layer using MAS with an IMBC

In a typical shielding configuration, an electromagnetic wave impinges on a conductive layer separating a region 1 from a region 2 of a stratified medium. The conductive layer acts as an electromagnetic shield blocking the field entering from region 1 to region 2. Most commonly, the examined stratified media have planar, cylindrical, or spherical interfaces which are considered as models of electromagnetic shields. In this work, we investigate cylindrical shielding layers.

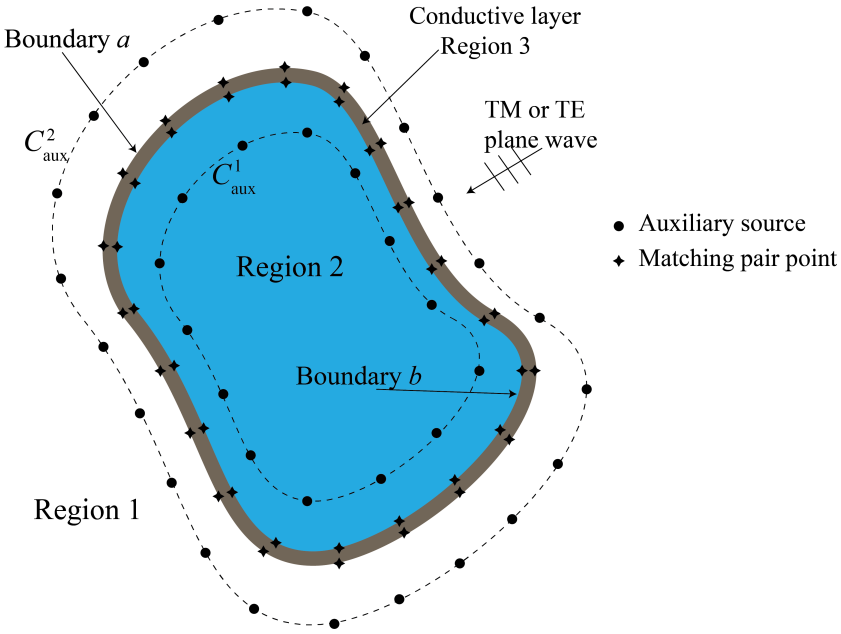

FIGURE 6.2: Multilayered cylindrical medium containing a conductive layer and the application of MAS with a 2-D IMBC.

6.3.1 Multilayered cylindrical medium with two regions

An infinite along z multilayered cylindrical medium is considered in which an arbitrarily-shaped and highly-conductive material of thickness Δ (region 3) separates regions 1 and 2, which are, respectively, occupied by dielectric materials with parameters ε_1, μ_1, and ε_2, μ_2, as illustrated in Fig. 6.2. The medium is excited by an incident plane electromagnetic field propagating in region 1 and given by

$$E_{\text{inc}}(x,y) = E_0 \exp\left[\mathrm{i}k_1\left(x\cos\varphi_{\text{inc}} + y\sin\varphi_{\text{inc}}\right)\right] \tag{6.8}$$

for TM_z polarization, and

$$H_{\text{inc}}(x,y) = H_0 \exp\left[\mathrm{i}k_1\left(x\cos\varphi_{\text{inc}} + y\sin\varphi_{\text{inc}}\right)\right] \tag{6.9}$$

for TE_z polarization, where ϕ_{inc} is the incident angle. The conductive layer is intended to act as an electromagnetic shield, shielding region 2 from the fields in region 1. Our purpose is to calculate the shielding effectiveness of this conductive layer. This problem can be solved analytically only for circular and elliptical shapes, while for any other shape numerical methods such as MAS can be applied.

The standard MAS implementation requires four sets of auxiliary sources, two in region 3 and one in regions 1 and 2 [123]. Each of these sets are distributed on auxiliary surfaces similar to the corresponding boundaries. The fields' determination in every region relies on the computation of the unknown auxiliary currents on each set, which is performed by applying the transmission boundary conditions of the problem.

In [106], it was shown that the vanishingly small MAS fields in the conductive region are difficult to converge to the true fields without a reasonable number of filaments, which may in turn lead to an ill-conditioned matrix. Hence, a modification in the standard MAS approach is necessary to avoid the calculation of the fields in region 3, which after all is an intermediate result when dealing with electromagnetic

shielding. This can be achieved by using a properly defined transfer function relating the fields on every point of boundary a with the fields on the opposite points of boundary b. Such a function was already proposed in [54] for planar conductive layers in the form of an equivalent impedance matrix. Essentially this means that the conductive layer is replaced by an Impedance Matrix Boundary Condition (IMBC).

Referring to Fig. 6.2, by applying the modified MAS with a 2-D IMBC, we only need two (instead of four) sets of auxiliary sources. Specifically, the scattered field in region 1 and the internal field in region 2 are simulated by the superpositions of the fields radiated by N_1 and N_2 filaments placed on the auxiliary surfaces C^1_{aux} and C^2_{aux}, carrying unknown currents I_{1j} (K_{1j}), $j = 0, \ldots, N_1 - 1$ and I_{2j} (K_{2j}), $j = 0, \ldots, N_2 - 1$, and radiating in an unbounded space filled by the medium of regions 1 and 2, respectively. The EM fields of the j-th source radiating in region m ($m = 1, 2$) are given by

$$E_{mj}(x,y) = -\hat{\mathbf{z}}\frac{k_m Z_m}{4} I_{mj} H_0^{(2)}\left(k_m \rho_{mj}\right) \tag{6.10}$$

$$H_{mj}\left(x,y\right) = \frac{k_m}{4\mathrm{i}} I_{mj} \frac{\hat{\mathbf{x}}\left(y_{mj}-y\right) + \hat{\mathbf{y}}\left(x-x_{mj}\right)}{\rho_{mj}} \times H_1^{(2)}\left(k_m \rho_{mj}\right) \tag{6.11}$$

for the TM_z case, and

$$H_{mj}(x,y) = -\hat{\mathbf{z}}\frac{k_m}{4Z_m} K_{mj} H_0^{(2)}\left(k_m \rho_{mj}\right) \tag{6.12}$$

$$E_{mj}\left(x,y\right) = \frac{k_m}{4\mathrm{i}} K_{mj} \frac{\hat{\mathbf{x}}\left(y_{mj}-y\right) + \hat{\mathbf{y}}\left(x-x_{mj}\right)}{\rho_{mj}} \times H_1^{(2)}\left(k_m \rho_{mj}\right) \tag{6.13}$$

for the TE_z case. Here, $\left(x_{mj},\, y_{mj}\right)$ are the coordinates of the filaments in region m, ρ_{mj} is the distance between the j-th filament in region m and the observation point (x,y), I_{mj} and K_{mj} are the amplitudes of the electric and magnetic currents of the j-th filament, $Z_m = \sqrt{\mu_m/\varepsilon_m}$ and $k_m = \omega\sqrt{\mu_m \varepsilon_m}$ are the impedance and wavenumber associated with the medium of region m, with ε_m and μ_m the corresponding dielectric permittivity and magnetic permeability.

Next, we apply the 2D-IMBC at M matching pairs, i.e., relate the fields at discrete points on boundary a, to the field at oppositely placed points on boundary b. This boundary condition is expressed as

$$\begin{bmatrix} \hat{\mathbf{n}}_a \times (\hat{\mathbf{n}}_a \times \mathbf{E}_a) \\ \hat{\mathbf{n}}_b \times (\hat{\mathbf{n}}_b \times \mathbf{E}_b) \end{bmatrix} = \begin{bmatrix} -Z_s & \sqrt{\frac{r_b}{r_a}} Z_{tr} \\ -\sqrt{\frac{r_a}{r_b}} Z_{tr} & Z_s \end{bmatrix} \begin{bmatrix} \hat{\mathbf{n}}_a \times \mathbf{H}_a \\ \hat{\mathbf{n}}_b \times \mathbf{H}_b \end{bmatrix}, \tag{6.14}$$

where

$$Z_s = -\mathrm{i} Z_3 \cot(k_3 \Delta), \quad Z_{tr} = -\mathrm{i} Z_3 \csc(k_3 \Delta). \tag{6.15}$$

In (6.14), $\mathbf{E}_a$, $\mathbf{H}_a$ and $\mathbf{E}_b$, $\mathbf{H}_b$ are the EM fields on the matching points of boundaries a and b, while Z_s, Z_{tr}, and Z_3 are the surface, the transfer, and the characteristic impedance of the conductive layer, k_3 is the wavenumber of the conductive layer,

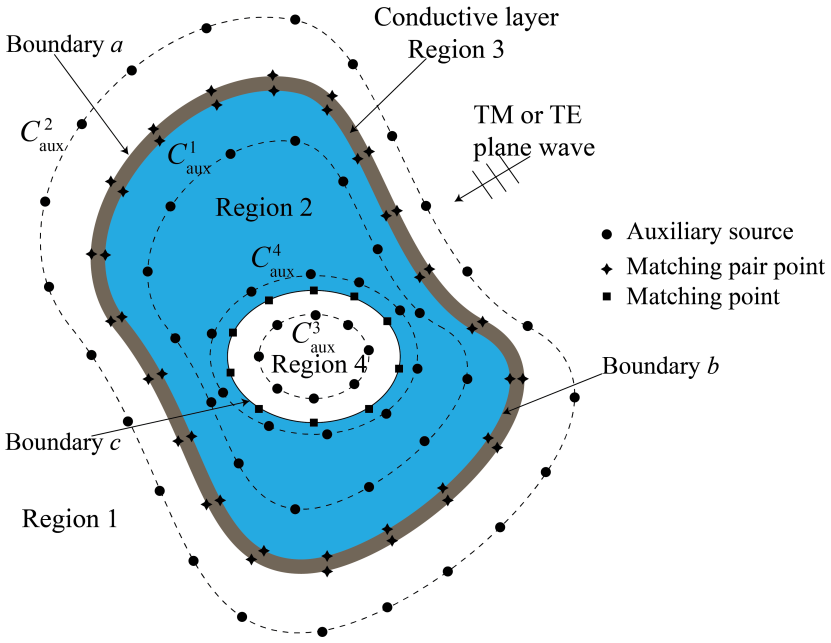

FIGURE 6.3: As in Fig. 6.2 but with an extra dielectric region.

r_a and r_b are the curvature radii corresponding to the matching points on boundaries a and b, and $\hat{\mathbf{n}}_a$ and $\hat{\mathbf{n}}_b$ are the normal unit vectors on boundaries a and b. In the Appendix of [54], it is shown that for a uniformly thick conductive layer holds $\hat{\mathbf{n}}_a = \hat{\mathbf{n}}_b = \hat{\mathbf{n}}$ and $r_a = r_b + \Delta$.

For $N_1 = N_2 = M$, (6.14) is a square linear system with respect to I_{mj} (K_{mj}) of the form

$$\mathbf{A}\mathbf{x} = \mathbf{b}, \tag{6.16}$$

where vector $\mathbf{x}$ contains the unknowns I_{mj} (K_{mj}), vector $\mathbf{b}$ contains samples of the E_{inc} and H_{inc} tangential fields at the matching points, and matrix $\mathbf{A}$ has entries obtained from the filaments' tangential fields at the matching points. Solving (6.14) yields I_{mj} (K_{mj}), which can in turn be used to find the fields in regions 1 and 2 via (6.10)-(6.13). Then, the shielding effectiveness for the TM_z and TE_z case is respectively given by

$$\text{SE}_E = -20\log_{10}\frac{\max|\mathbf{E}_2|}{|\mathbf{E}_{\text{inc}}|}, \tag{6.17}$$

and

$$\text{SE}_H = -20\log_{10}\frac{\max|\mathbf{H}_2|}{|\mathbf{H}_{\text{inc}}|}, \tag{6.18}$$

where $\max|\mathbf{E}_2|$ and $\max|\mathbf{H}_2|$ are the maximum norm values of the EM fields in region 2.

6.3.2 Multilayered cylindrical medium with three regions

When a third dielectric layer is added to the medium, two extra sets of auxiliary sources are needed, which are associated to the third boundary c; see Fig. 6.3. The scattered field by the third layer, that contributes to the field in region 2, is simulated by the fields of the filaments on C^3_{aux} carrying unknown currents I_{3j} (K_{3j}), $j = 0, \ldots, N_3 - 1$ and radiating in an unbounded space filled with the medium of

region 2. The field in region 4 is simulated by the fields of the filaments on C^4_{aux} carrying unknown currents I_{4j} (K_{4j}), $j = 0, \ldots, N_4 - 1$ and radiating in an unbounded space filled with the medium of region 4. To compute I_{3j} (K_{3j}) and I_{4j} (K_{4j}), we apply the boundary conditions

$$\hat{\mathbf{n}}_c \times (\mathbf{E}_2 - \mathbf{E}_4) = \mathbf{0}, \tag{6.19}$$

$$\hat{\mathbf{n}}_c \times (\mathbf{H}_2 - \mathbf{H}_4) = \mathbf{0} \tag{6.20}$$

at M matching points on boundary c. Here, $\mathbf{E}_2$ and $\mathbf{H}_2$ are the fields radiated by the sources of C^2_{aux} and C^3_{aux}, $\mathbf{E}_4$ and $\mathbf{H}_4$ are the fields in region 4 due to the sources on C^4_{aux}, and $\hat{\mathbf{n}}_c$ is the normal unit vector of a matching point on boundary c. Combining (6.14) with (6.19)-(6.20) for $N_1 = N_2 = N_3 = N_4 = M$, yields a square linear system of the form (6.16), the solution of which gives the auxiliary currents and then the fields in each region are determined from (6.10)-(6.13). If the shielded region is region 4 then the shielding effectiveness is defined as in (6.17) and (6.18), but with $\mathbf{E}_4$ and $\mathbf{H}_4$ in place of $\mathbf{E}_2$ and $\mathbf{H}_2$.

6.4 Numerical Results

In this section, we present numerical results to demonstrate the theoretical shielding effectiveness of an ideal graphene monolayer in cylindrical shielding configurations of various cross sections in the frequency range 0.5-12 GHz. In all examined cases, the parameter values related to the graphene's surface conductivity are $\Delta = 0.5$ nm, $T = 300K$, $\tau = 6.582$ps and $E_F = 0.5$eV. For all the cylindrical geometries, four regions are considered: regions 1 and 4 are filled with air, region 2 is a layer of SiO_2 and region 3 is the graphene monolayer; thus, $\varepsilon_1 = \varepsilon_4 = \varepsilon_0$ and $\varepsilon_2 = 3.9\varepsilon_0$. The modified MAS with IMBC results for each case are compared to those obtained by FEM. Besides, we note that we also simulated the standard MAS and found that its results are significantly different (even by orders of magnitude) with respect to the corresponding ones of MAS with IMBC and of FEM.

It is also worth to point out that in the examples that follow, graphene is considered an isotropic material. For the case that graphene exhibits spatial dispersion (anisotropy) a modification of the IMBC is necessary. This modification was presented in [24] in relation to the shielding effectiveness of Carbon Fiber Composites-Based Cylindrical Shells, which are also anisotropic materials. It is in our near future intention to apply this modified IMBC to study the anisotropic behavior of graphene as a shielding material.

6.4.1 Monolayer graphene on a circular cylinder

Consider the multilayered cylindrical medium of Fig. 6.4 with $r_b = 15$ cm, $r_a = r_b + \Delta$, and $r_c = 0.9r_b$, excited by a TM_z or TE_z plane field given by (6.8) or (6.9) with $\phi_{\text{inc}} = 0^{\text{o}}$ and $f = 3$ GHz. The four employed auxiliary surfaces $C^1_{\text{aux}}, C^2_{\text{aux}}, C^3_{\text{aux}}$ and C^4_{aux} of radii $r^1_{\text{aux}} = 0.8r_b, r^2_{\text{aux}} = 2r_b, r^3_{\text{aux}} = 0.8r_c$ and $r^4_{\text{aux}} = 1.2r_c$ host $N_1 = N_2 = N_3 = N_4 = 70$ auxiliary sources. Applying the boundary conditions (6.14), (6.19) and (6.20) on $M = 70$ matching points on each boundary, and following the MAS procedure analyzed in Sec. 6.3.2, we compute the fields in regions 1 and 4 on two circles of radii $r_{o1} = 2r_b$ and $r_{o2} = 0.6r_c$, respectively. The norms of these fields are depicted in Fig. 6.5 and are in excellent agreement with the corresponding results obtained by FEM.

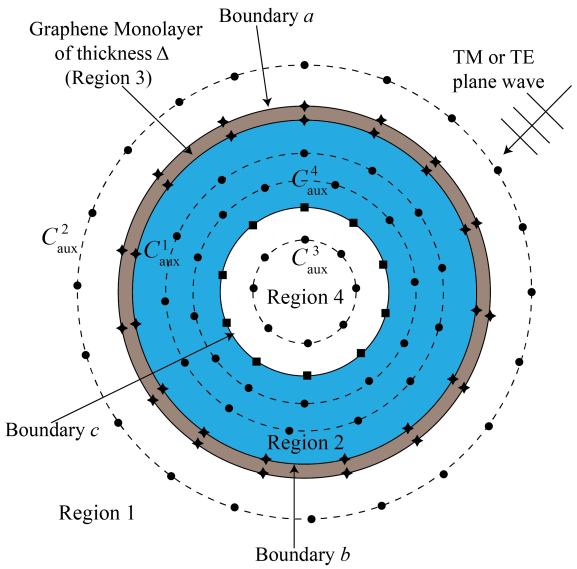

FIGURE 6.4: Application of MAS with 2-D IMBC on a circular multi-layered cylindrical medium including a graphene monolayer.

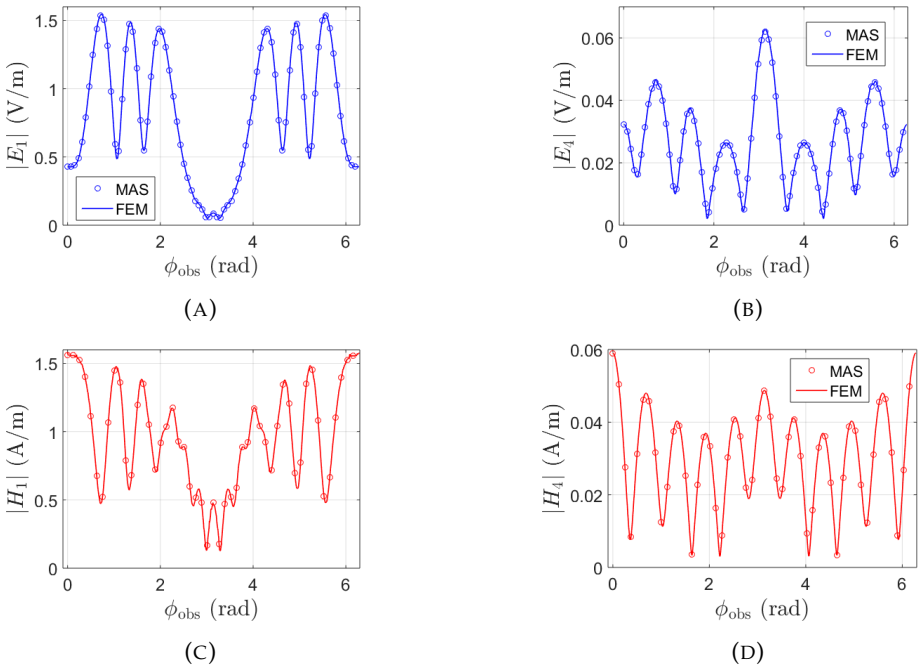

FIGURE 6.5: Norms of the fields in regions 1 and 4 for (a), (b) TM polarization and (c), (d) TE polarization for the geometry of Fig. 6.4.

Then, we calculate the shielding effectiveness of the graphene layer for a number of frequencies and depict the results in Fig. 6.6. In Fig. 6.7, we demonstrate the effect of the chemical potential E_F in the shielding effectiveness of the graphene monolayer for $f = 3$ GHz. Besides, in Fig. 6.8 we depict the norm of the TM-polarized electric field showing clearly the obtained shielding effect.

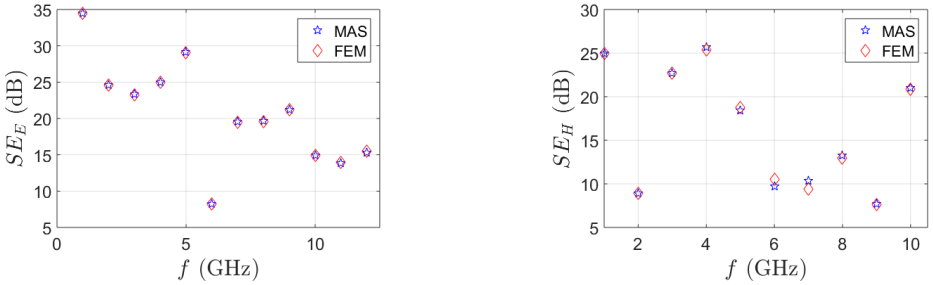

FIGURE 6.6: Shielding effectiveness versus the frequency f for the geometry of Fig. 6.4 for TM (left panel) and TE (right panel) polarization.

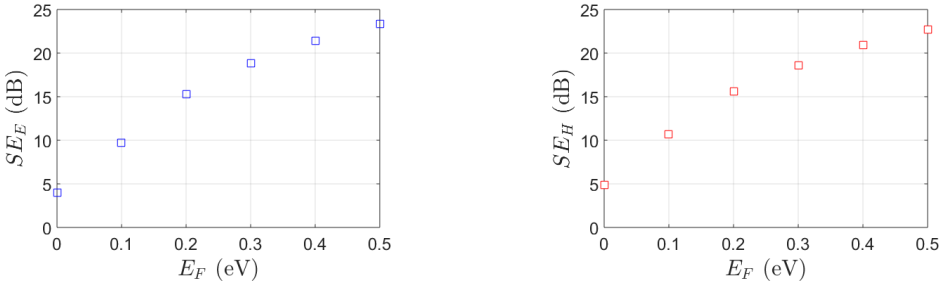

FIGURE 6.7: Shielding effectiveness versus the chemical potential E_F for $f = 3$ GHz for the geometry of Fig. 6.4 for TM (left panel) and TE (right panel) polarization.

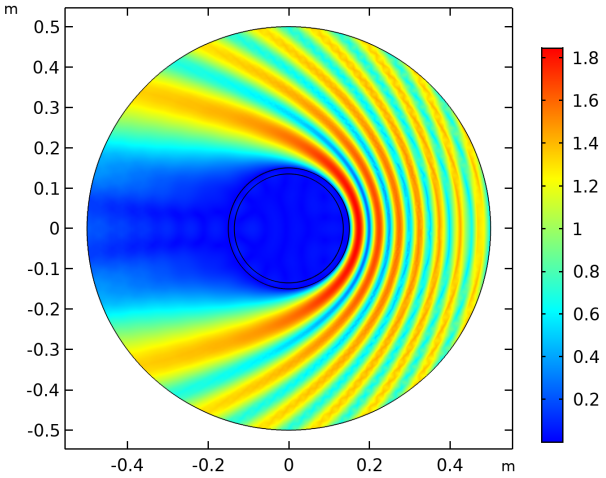

FIGURE 6.8: Norm of the TM-polarized electric field in V/m for the geometry of Fig. 6.4 with $f = 3$ GHz and $E_F = 0.5$ eV.

6.4.2 Monolayer graphene on an elliptical cylinder

The cross section of a three-layered cylindrical medium with elliptical boundaries is depicted in Fig. 6.9. For boundary b, the semi-axes are $\alpha = 15$ cm and $\beta = 12$ cm, the coordinates of the matching points are $(x_b,\ y_b)$, while the corresponding points on boundary a are $(x_a,\ y_a) = (x_b + \mathrm{n}_x\Delta,\ y_b + \mathrm{n}_y\Delta)$, where n_x and n_y are the components of the common normal unit vector $\hat{\mathbf{n}}$ on each point of a and b. The matching points on boundary c are $(x_c,\ y_c) = 0.9\,(x_b,\ y_b)$.

A $\mathrm{TM_z}$ or $\mathrm{TE_z}$ plane wave with $\phi_{\mathrm{inc}} = 0^{\mathrm{o}}$ and $f = 3$ GHz impinges on the

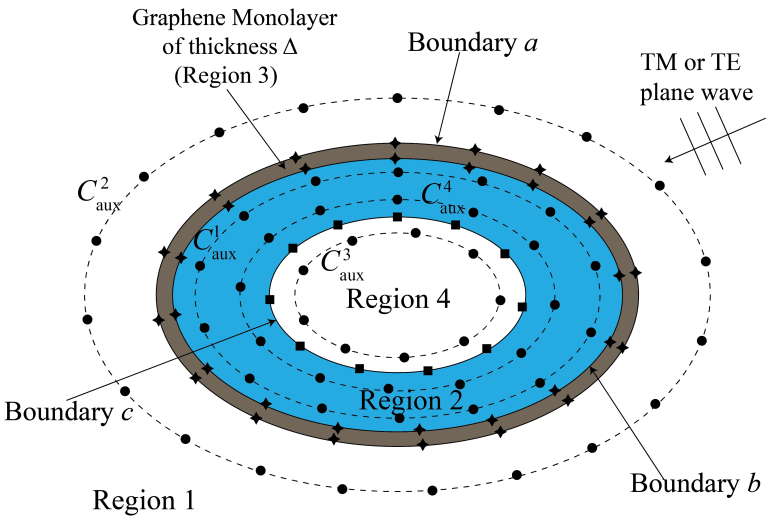

FIGURE 6.9: Application of MAS with 2-D IMBC on an elliptical multilayered cylindrical medium including a graphene monolayer.

medium. Four sets of auxiliary sources with $N_1 = N_2 = N_3 = N_4 = 80$ are placed on the auxiliary surfaces $C^1_{\text{aux}}, C^2_{\text{aux}}, C^3_{\text{aux}}$ and C^4_{aux} with respective coordinates of the sources $(x_{a1}, y_{a1}) = 0.8\,(x_b, y_b)$, $(x_{a2}, y_{a2}) = 2\,(x_b, y_b)$, $(x_{a3}, y_{a3}) = 0.8\,(x_c, y_c)$ and $(x_{a4}, y_{a4}) = 1.2\,(x_c, y_c)$. Applying the boundary conditions (6.14), (6.19) and (6.20) on $M = 80$ matching pairs on a and b, and the same number of points on boundary c, and solving the resulting linear system, we compute the fields in regions 1, 2 and 4. In Fig. 6.10, we depict the norm of the fields in regions 1 and 4 on two ellipses with $(x_{o1}, y_{o1}) = 2(x_b, y_b)$ and $(x_{o2}, y_{o2}) = 0.6\,(x_c, y_c)$. The plots of the shielding effectiveness versus f for $E_F = 0.5$ eV and versus E_F for $f = 3$ GHz are shown in Figs. 6.11 and 6.12, respectively. Fig. 6.13 visualizes the shielding effect.

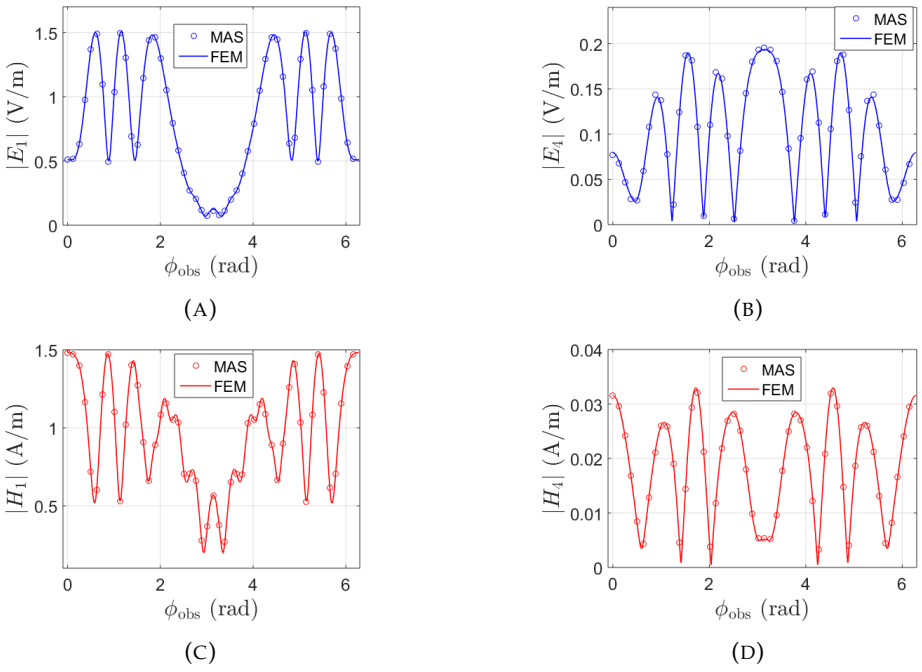

FIGURE 6.10: Norms of the fields in regions 1 and 4 for (a), (b) TM polarization and (c), (d) TE polarization for the geometry of Fig. 6.9.

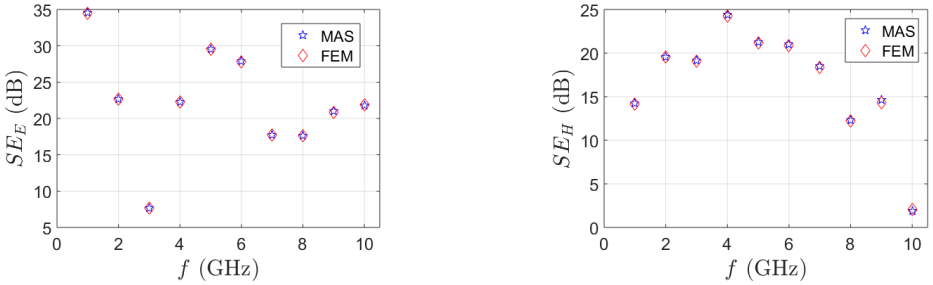

FIGURE 6.11: Shielding effectiveness with respect to the frequency f with $E_F = 0.5$ eV for the geometry of Fig. 6.9 for TM (left panel) and TE (right panel) polarization.

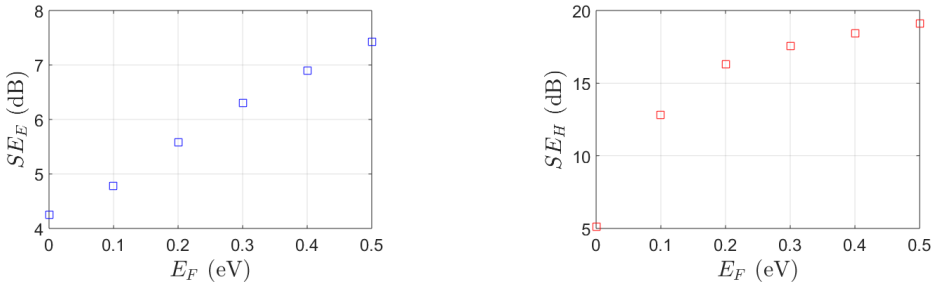

FIGURE 6.12: Shielding effectiveness with respect to E_F with $f = 3$GHz for the geometry of Fig. 6.9 for TM (left panel) and TE (right panel) polarization.

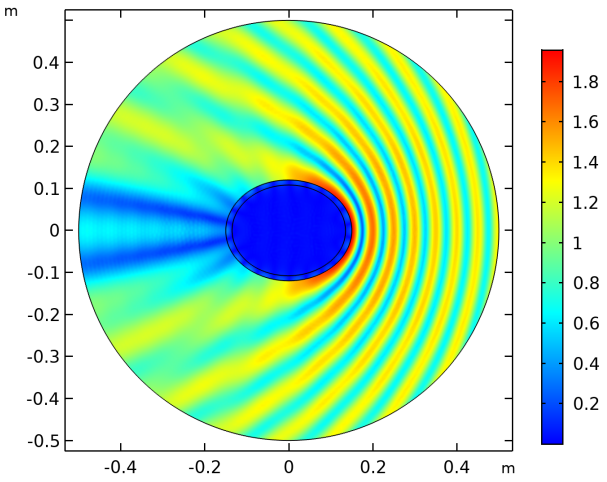

FIGURE 6.13: Norm of the TE-polarized magnetic field in A/m for the geometry of Fig. 6.9 with $f = 3$ GHz and $E_F = 0.5$ eV.

6.4.3 Monolayer graphene on a rounded-triangular cylinder

Next, we investigate a three-layered cylinder with rounded-triangular boundaries, as illustrated in Fig. 6.14. The coordinates of the matching points on boundary b are

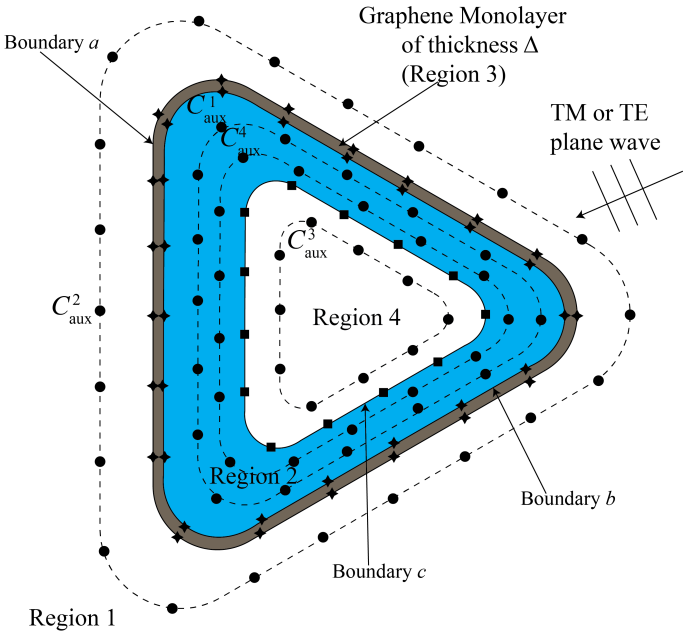

FIGURE 6.14: Application of MAS with 2-D IMBC on a rounded-triangular medium including a graphene monolayer.

given in cm by

$$x_b = 17.5(\cos\varphi + 0.2\cos(2\varphi))$$
$$y_b = 17.5(\sin\varphi - 0.2\sin(2\varphi))$$

where φ is the azimuthal angle. The coordinates of the oppositely placed matching points on boundary a are $(x_a, y_a) = (x_b + n_x\Delta, y_b + n_y\Delta)$, while for those on boundary c the coordinates are $(x_c,\ y_c) = 0.9\,(x_b,\ y_b)$. A TM_z or TE_z plane wave with $f = 3$ GHz and $\phi_{\text{inc}} = 0^o$ impinges on the medium.

We apply the modified MAS with a 2-D IMBC for four sets of auxiliary sources with $N_1 = N_2 = N_3 = N_4 = M = 90$ and coordinates of the sources' points $(x_{a1}, y_{a1}) = 0.9\,(x_b, y_b)$, $(x_{a2}, y_{a2}) = 1.1\,(x_b, y_b)$, $(x_{a3}, y_{a3}) = 0.9\,(x_c, y_c)$ and $(x_{a4}, y_{a4}) = 1.1\,(x_c, y_c)$. In Fig. 6.15, we depict the norms of the fields in regions 1 and 4, on two rounded triangles with $(x_{o1}, y_{o1}) = 2(x_b, y_b)$ and $(x_{o2}, y_{o2}) = 0.6\,(x_c, y_c)$. The respective plots of the shielding effectiveness are given in Figs. 6.16-6.18.

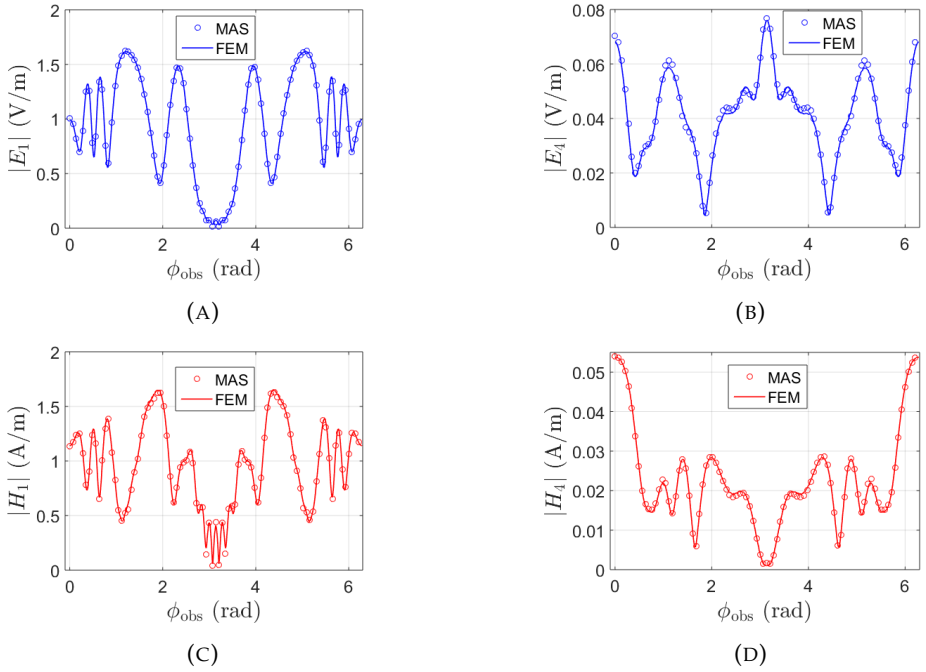

FIGURE 6.15: Norms of the fields in regions 1 and 4 for (a), (b) TM polarization and (c), (d) TE polarization for the geometry of Fig. 6.14.

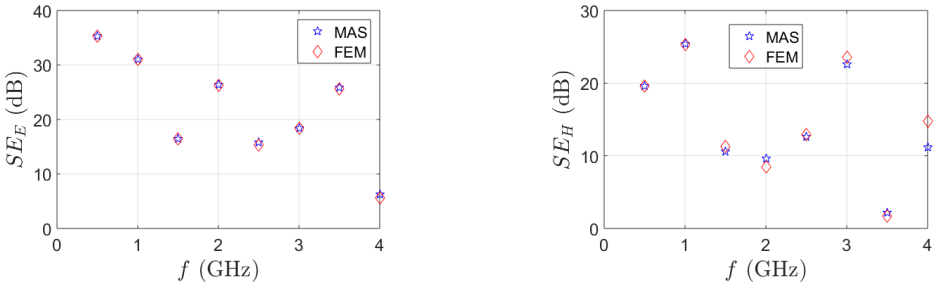

FIGURE 6.16: Shielding effectiveness with respect to the frequency f with $E_F = 0.5$ eV for the geometry of Fig. 6.14 for TM (left panel) and TE (right panel) polarization.

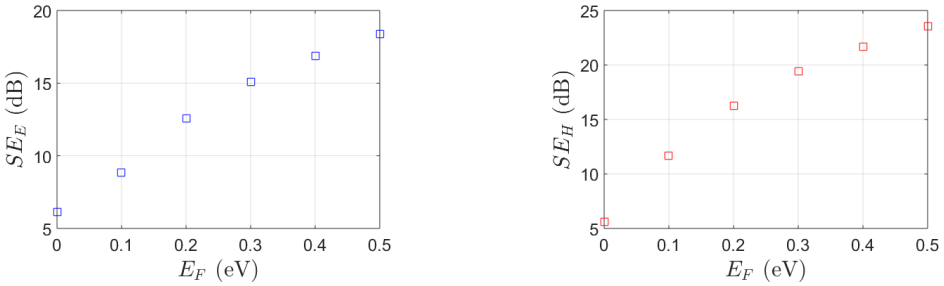

FIGURE 6.17: Shielding effectiveness with respect to E_F with f = 3GHz for the geometry of Fig. 6.14 for TM (rleft panel) and TE (right panel) polarization.

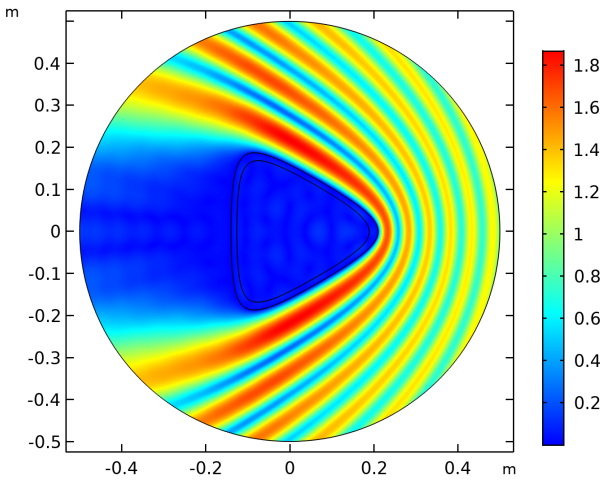

FIGURE 6.18: Norm of the TM-polarized electric field in V/m for the geometry of Fig. 6.14 with $f = 3$ GHz and $E_F = 0.5$ eV.

6.4.4 Monolayer graphene on an inverted-elliptical cylinder

Finally, we examine a three-layered inverted-elliptical cylinder, as shown in Fig. 6.19. The coordinates of the matching points on boundary b are given in cm by

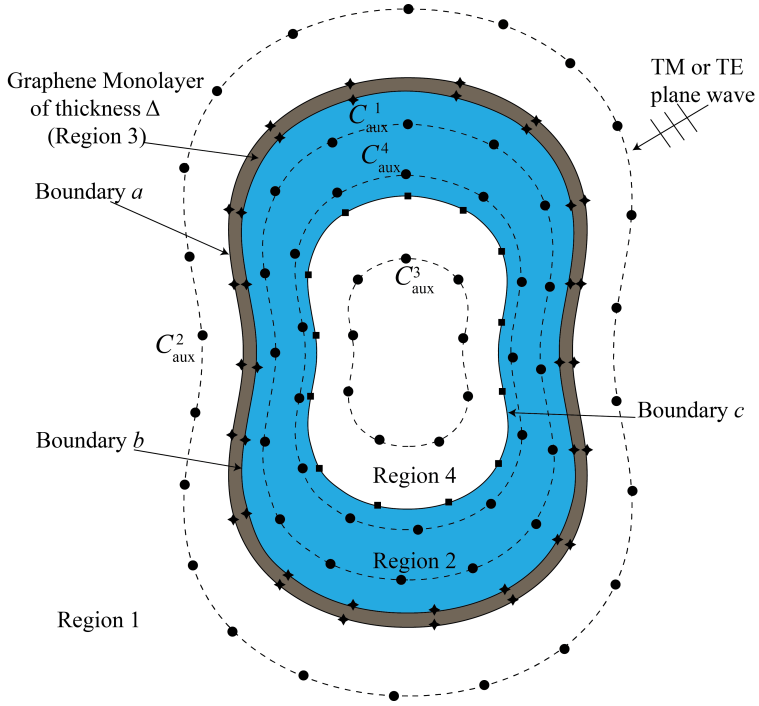

FIGURE 6.19: Application of MAS with 2-D IMBC on an inverted-elliptical medium including a graphene monolayer.

$$x_b = 14.444\frac{(\cos\varphi + 0.3\cos\varphi\cos(2\varphi) + 0.3\sin\varphi\sin(2\varphi))}{\left[(1+0.3\cos(2\varphi))^2 + 0.09\sin^2(2\varphi)\right]},$$

$$y_b = 14.444\frac{(\sin\varphi + 0.3\sin\varphi\cos(2\varphi) - 0.3\cos\varphi\sin(2\varphi))}{\left[(1+0.3\cos(2\varphi))^2 + 0.09\sin^2(2\varphi)\right]},$$

while those on boundaries a and c by $(x_a, y_a) = \left(x_b + n_x\Delta, y_b + n_y\Delta\right)$ and $(x_c,\ y_c) = 0.9\,(x_b,\ y_b)$. The incident plane wave is the same as in the previous geometries.

For the application of MAS, we consider $N_1 = N_2 = N_3 = N_4 = M = 120$ with $(x_{a1}, y_{a1}) = 0.9\,(x_b, y_b)$, $(x_{a2}, y_{a2}) = 1.1\,(x_b, y_b)$, $(x_{a3}, y_{a3}) = 0.9\,(x_c, y_c)$ and $(x_{a4}, y_{a4}) = 1.1\,(x_c, y_c)$. Figure 6.20 shows the norms of the fields in regions 1 and 4 on inverted ellipses with $(x_{o1}, y_{o1}) = 2(x_b, y_b)$ and $(x_{o2}, y_{o2}) = 0.6\,(x_c, y_c)$. The respective plots of the shielding effectiveness are depicted in Figs. 6.21-6.23.

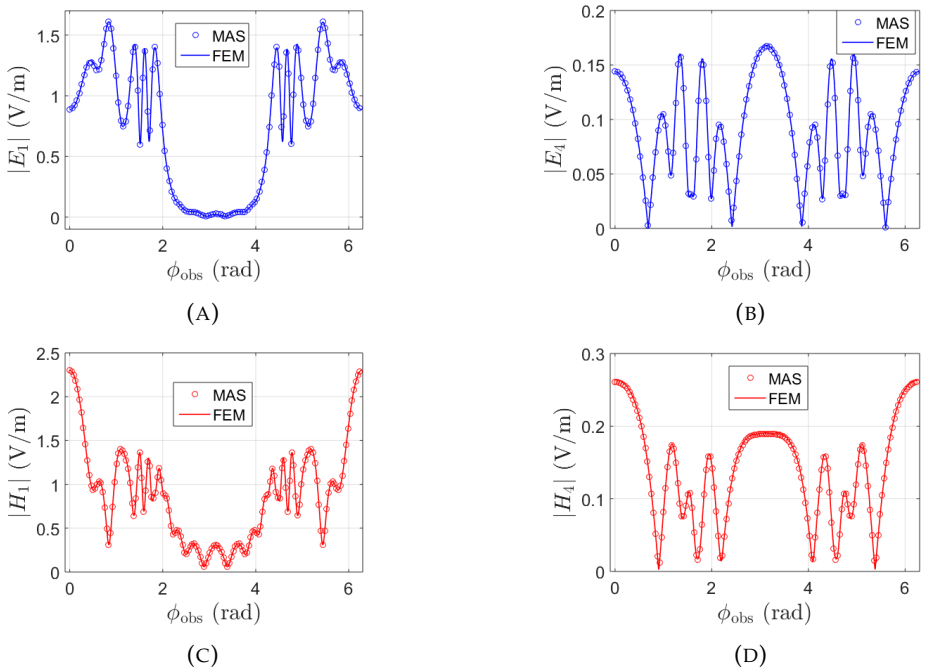

FIGURE 6.20: Norms of the fields in regions 1 and 4 for (a), (b) TM polarization and (c), (d) TE polarization for the geometry of Fig. 6.19.

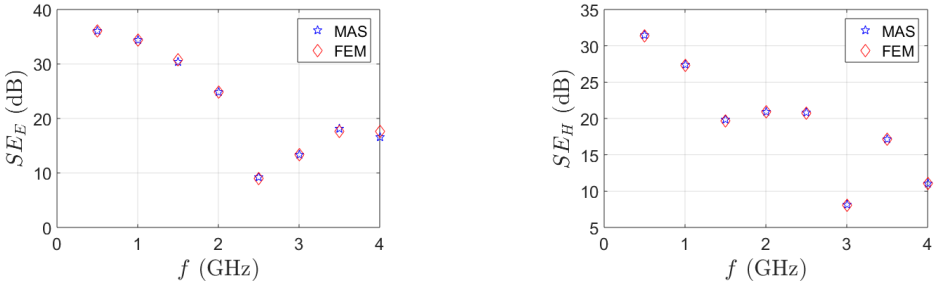

FIGURE 6.21: Shielding effectiveness with respect to the frequency f with $E_F = 0.5$ eV for the geometry of Fig. 6.19 for TM (left panel) and TE (right panel) polarization.

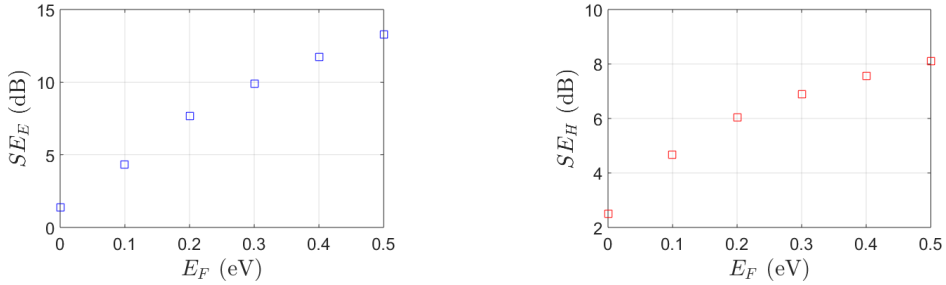

FIGURE 6.22: Shielding effectiveness with respect to E_F with f = 3GHz for the geometry of Fig. 6.19 for TM (left panel) and TE (left panel) polarization.

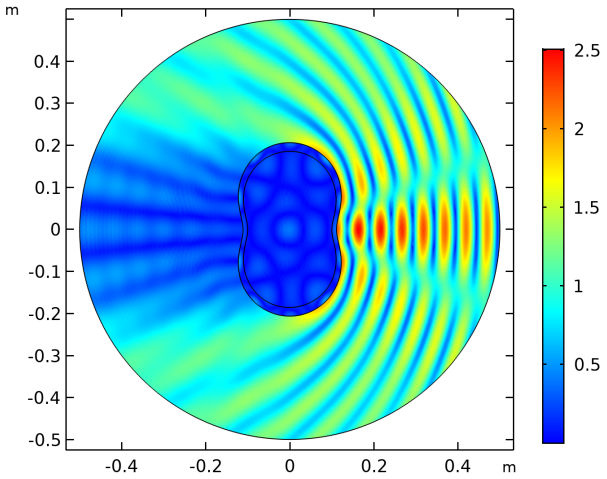

FIGURE 6.23: Norm of the TE-polarized magnetic field in A/m for the geometry of Fig. 6.19 with $f = 3$ GHz and $E_F = 0.5$ eV.

6.4.5 Trilayer graphene on a circular cylinder

To demonstrate the shielding effectiveness of an FLG shield, we investigate the case of a AAA' trilayer graphene placed on the circular multilayered medium of Fig. 6.4. The surface conductivity, of this trilayer is calculated by combining (6.1), (6.6) and (6.7), while the permittivity is given by (6.3). The parameter values chosen are $\Delta_{AAA'} = 1.5$ nm, $T = 300$ K, $\tau = 6.582$ ps, and $E_F = 0.5$ eV. The shielding effectiveness of this trilayer is plotted with respect to frequency (for TM polarization) in Fig. 6.24, and is found to be almost 10 dB's larger than that of monolayer graphene, shown in Fig. 6.6.

6.5 Conclusions

Monolayer Graphene is a very promising EMI shielding material especially in the RF/microwave region. Hence, there is a necessity to develop numerical techniques that will theoretically measure the shielding performance of a graphene-based shield at the initial design stages of an enclosure. For this purpose, we have demonstrated that MAS combined with an IMBC can yield very accurate results. Specifically, cylindrical configurations of various cross sections were investigated and very high values of shiedling effectiveness were obtained for a number of frequencies in the RF/microwave region. The tunability of graphene's shielding effectiveness was also

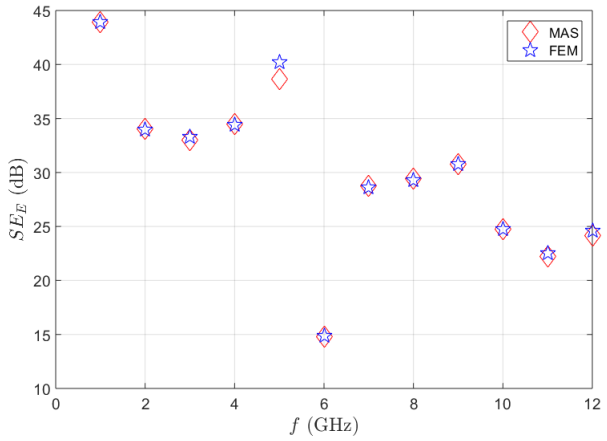

FIGURE 6.24: Shielding effectiveness of a trilayer AAA′ graphene shield, versus the frequency f, for the geometry of Fig. 6.4 for TM polarization.

demonstrated by changing the value of the Fermi energy. Future research will be focused on the effect of graphene's spatial dispersion in its shielding effectiveness as well as on the extension of this work to 3-D shielding geometries, having [124]–[126] as starting points.

Chapter 7

Conclusions and future work

In this Chapter we will present the main contributions of this Phd thesis and outline plans for future work.

7.1 General conclusions

In Chapter 2 TE scattering scenarios from PEC cylinders are studied. The circular geometry is investigated, which is solved analytically and verified numerically along with some complex geometries. The main contributions of Chapter 2 are

- For the circular geometry, it was shown analytically that the MAS magnetic field converges to the true field, even when the MAS currents diverge and oscillate. An asymptotic formula was analytically derived for the case of a large number of auxiliary sources which predicts accurately the nature and characteristics of the currents oscillations. The abovementioned conclusions were demonstrated numerically for more complex geometries.
- We concluded that the oscillations in the current amplitudes should in general be avoided. Since the scattered field is expected to be small, while the intermediate quantities (the currents) are very large, subtractive cancelation is bound to occur. Hence, increasing the auxiliary-source number N will cause a vast increase in both the currents and the matrix condition number, and, in turn, the computed field will deteriorate rapidly with N.
- More importantly, even when the MAS currents diverge and oscillate, the MAS solution is not automatically invalidated. As it has been shown in Chapter 2, the MAS field converges in spite of the divergence and oscillations of the MAS currents.

The scope of Chapter 3 is the application of MAS in mode analysis of simply and multiply connected PEC waveguides. The main contributions of this chpater are:

- It is first shown that standard MAS approach (non-driven problem) yields spurious solutions; thus, a modification is proposed. Specifically, an excitation source is added to the configuration (driven problem) yielding MAS-ES. Excitation sources are either plane waves, or current filaments (electric or magnetic) which can be internal or external to the waveguide domain.
- We prove, that when internal excitation is used no regularization is needed. This is proved analytically for the circular waveguide and verified numerically for all examined geometries. The need for regularization for an external excitation source is also elaborated analytically and numerically.

- It is demonstrated that the divergence of the MAS currents appear as oscillations of their real parts between large values of alternating sign. Importantly, however, this divergence may not affect the computation of the eigenvalues.

Chapter 4 is an extension of Chapter 3 where it is demonstrated that the eigenvalues can be computed via the auxiliary current amplitudes. The main contributions of Chapter 4 are the following

- It is proven analytically for the circular waveguide and numerically for arbitrary cross sections, that waveguide eigenvalues can be found by detecting the peak values of the ACVN plot.
- The ACVN approach, is algorithmically simpler and thus faster than the $F(k)$ approach. For a small number of auxiliary sources the ACVN plots are much smoother than the $F(k)$ response curves, resulting in a more accurate detection of plot peaks.
- It is proven numerically that not-too-rapid oscillations in the auxiliary currents do not affect the eigenvalues' detrmination
- A Hankel-function lookup procedure is proposed which speeds up significantly the filling of the impedance matrix.

The scope of Chapter 5 is to prove that MAS-ES is suitable for dielectric waveguide mode analysis. The main contributions of the chapter are:

- It is proven numerically that two internal excitation sources, a magnetic and electric, are necessary to excite the hybrid modes of the dielectric waveguides resulting to MAS-TES.
- The eigenvalues are detected by measuring the fields inside the core by means of a response function the peaks of which correspond to the eigenvalues.
- A significant number of numerical experiments showed that no spurious eigenvalues are detected, provided that the excitation sources are placed inside an optimum curve. Thus the method is characterized as spurious free.

Our intention in Chapter 6 is to prove that MAS can be a reliable method to study electromagnetic shielding even for extremely thin shielding materials such as monolayer graphene. The contributions are the following:

- Cylindrical electromagnetic shields consisting of monolayer or trilayer graphene deposited on silicon dioxide are proposed. Such shields have the advantage of being optically transparent, non corrosive, and relatively light weighted, thus, they are potentially realizable.
- It is demonstrated that appying MAS with the graphene layer being replaced by an IMBC, achieve highly accurate results regarding the shielding effectivenes of graphene. A significant number of geometries are investigated with the results yielding a shielding effectiveness up to 40 dB in the RF region.
- The tunability of graphene's shielding effectiveness is also demonstrated by changing the value of the Fermi energy.

7.2 Future Work

Regarding Chapter 2, future work concerns the systematic analysis of the corresponding phenomena for noncircular shapes. It is further interesting to investigate in more detail MAS solutions, with not-too-rapidly-oscillating MAS currents, in which some numerical instability due to oscillations is outweighed by advantages such as a rapid speed of convergence of the scattered field.

For Chapters 3 and 4, we plan to extend the application of MAS-ES in 3-D resonant cavities. Initial studies show that the proper excitation sources are plane waves, or elementary dipoles (electric or magnetic). Suitable auxiliary sources are pairs of elementary dipoles, electric and magnetic, perpendicular to each other. Thus, the components of the ACVN are the dipole moments of the auxiliary elementary dipoles.

Our future intention regarding the work of Chapter 5, is to apply the MAS-TES in anisotropic dielectric waveguides. There is a question on whether two excitation sources are necessary in this case, since the anisotropy of the materials might yield hybrid modes with a single electric or magnetic current source. Also, the possibillity that an oblique plane wave can be an excitation source for dielectric waveguides in general will be investigated.

Finally, in relation to our work with graphene, we intend to investigate the shielding effectiveness of magnetostatically biased monolayer graphene, which showcases anisotropy. This requires a modification of MAS-IMBC in order to be suitable for anisotropic shielding materials. We also plan to investigate 3-D shielding configurations.

Bibliography

[1] W. C. Chew, M. S. Tong, and B. Hu, "Integral equation methods for electromagnetic and elastic waves," *Synthesis Lectures on Computational Electromagnetics*, vol. 3, no. 1, pp. 1–241, 2008.

[2] R. F. Harrington, *Time-Harmonic Electromagnetic Fields*. IEEE-Press, 2001. DOI: 10.1109/9780470546710. [Online]. Available: http://dx.doi.org/10.1109/9780470546710.

[3] R. Lee and A. C. Cangellaris, "A study of discretization error in the finite element approximation of wave solutions," *IEEE transactions on antennas and propagation*, vol. 40, no. 5, pp. 542–549, 1992.

[4] S. Velamparambil, W. C. Chew, and J. Song, "10 million unknowns: Is it that big?[computational electromagnetics]," *IEEE Antennas and Propagation Magazine*, vol. 45, no. 2, pp. 43–58, 2003.

[5] R. F. Harrington, *Field computation by moment methods*. Wiley-IEEE Press, 1993.

[6] S. Rao, D. Wilton, and A. Glisson, "Electromagnetic scattering by surfaces of arbitrary shape," *IEEE Transactions on antennas and propagation*, vol. 30, no. 3, pp. 409–418, 1982.

[7] T. Wriedt, *Generalized multipole techniques for electromagnetic and light scattering*. Elsevier, 1999.

[8] T. Wriedt and Y. Eremin, "The generalized multipole technique for light scattering," *Springer Series on Atomic, Optical, and Plasma Physics. Switzerland, Springer Nature*, 2018.

[9] A. Ludwig, "The generalized multipole technique," *Computer Physics Communications*, vol. 68, no. 1-3, pp. 306–314, 1991.

[10] Y. Leviatan, A. Boag, and A. Boag, "Generalized formulations for electromagnetic scattering from perfectly conducting and homogeneous material bodies-theory and numerical solution," *IEEE Transactions on antennas and propagation*, vol. 36, no. 12, pp. 1722–1734, 1988.

[11] Y. Leviatan and A. Boag, "Analysis of electromagnetic scattering from dielectric cylinders using a multifilament current model," *IEEE Transactions on antennas and propagation*, vol. 35, no. 10, pp. 1119–1127, 1987.

[12] Y. Leviatan, A. Boag, and A. Boag, "Analysis of te scattering from dielectric cylinders using a multifilament magnetic current model," *IEEE transactions on antennas and propagation*, vol. 36, no. 7, pp. 1026–1031, 1988.

[13] Y. Leviatan, A. Boag, and A. Boag, "Analysis of electromagnetic scattering using a current model method," *Computer physics communications*, vol. 68, no. 1-3, pp. 331–345, 1991.

[14] D. I. Kaklamani and H. T. Anastassiu, "Aspects of the method of auxiliary sources (mas) in computational electromagnetics," *IEEE Antennas and Propagation Magazine*, vol. 44, no. 3, pp. 48–64, 2002.

[15] A. H. Cheng and Y. Hong, "An overview of the method of fundamental solutions—solvability, uniqueness, convergence, and stability," *Engineering Analysis with Boundary Elements*, vol. 120, pp. 118–152, 2020.

[16] G. K. Avdikos and H. T. Anastassiu, "Computational cost estimations and comparisons for three methods of applied electromagnetics (mom, mas, mmas)," *IEEE Antennas and Propagation Magazine*, vol. 47, no. 1, pp. 121–129, 2005.

[17] N. Tsitsas, G. Palaiopanos, and G. Fikioris, "The method of auxiliary sources applied to three-dimensional acoustic scattering: Convergence issues and inherent oscillations," *Acta Acustica united with Acustica*, vol. 102, no. 2, pp. 322–333, 2016.

[18] G. Fikioris, N. L. Tsitsas, and G. K. Charitos, "Spurious oscillations in a combined method-of-auxiliary-sources/extended-integral-equation solution to a simple scattering problem," *Journal of Quantitative Spectroscopy and Radiative Transfer*, vol. 123, pp. 30–40, 2013.

[19] Y. Leviatan, "Analytic continuation considerations when using generalized formulations for scattering problems," *IEEE transactions on Antennas and Propagation*, vol. 38, no. 8, pp. 1259–1263, 1990.

[20] G. Fikioris, "On two types of convergence in the method of auxiliary sources," *IEEE Transactions on Antennas and Propagation*, vol. 54, no. 7, pp. 2022–2033, 2006. DOI: 10.1109/TAP.2006.877171.

[21] G. Fikioris and I. Psarros, "On the phenomenon of oscillations in the method of auxiliary sources," *IEEE transactions on antennas and propagation*, vol. 55, no. 5, pp. 1293–1304, 2007.

[22] C. A. Valagiannopoulos, N. L. Tsitsas, and G. Fikioris, "Convergence analysis and oscillations in the method of fictitious sources applied to dielectric scattering problems," *JOSA A*, vol. 29, no. 1, pp. 1–10, 2012.

[23] G. Fikioris and N. L. Tsitsas, "On convergence and inherent oscillations within computational methods employing fictitious sources," *Computers & Mathematics with Applications*, vol. 69, no. 7, pp. 636–649, 2015.

[24] K. Wang, J.-J. Laurin, and K. Wu, "Scattering and shielding analyses of carbon fiber composites-based cylindrical shells using a multifilament doublet current method," *IEEE Transactions on Electromagnetic Compatibility*, vol. 61, no. 4, pp. 1015–1024, 2018.

[25] B. Sternin and V. Shatalov, *Differential equations on complex manifolds*. Springer Science & Business Media, 2013, vol. 276.

[26] N. L. Tsitsas, G. P. Zouros, G. Fikioris, and Y. Leviatan, "On methods employing auxiliary sources for 2-d electromagnetic scattering by noncircular shapes," *IEEE Transactions on Antennas and Propagation*, vol. 66, no. 10, pp. 5443–5452, 2018.

[27] G. Fikioris and N. L. Tsitsas, "Convergent fields generated by divergent currents in the method of auxiliary sources," in *The Generalized Multipole Technique for Light Scattering*, Springer, 2018, pp. 93–119.

[28] H. T. Anastassiu, D. G. Lymperopoulos, and D. I. Kaklamani, "Accuracy analysis and optimization of the method of auxiliary sources (mas) for scattering by a circular cylinder," *IEEE Transactions on antennas and Propagation*, vol. 52, no. 6, pp. 1541–1547, 2004.

[29] N. L. Tsitsas, E. G. Alivizatos, and G. H. Kalogeropoulos, "A recursive algorithm for the inversion of matrices with circulant blocks," *Applied mathematics and computation*, vol. 188, no. 1, pp. 877–894, 2007.

[30] N. Tsitsas, E. Alivizatos, H. Anastassiu, and D. Kaklamani, "Optimization of the method of auxiliary sources (mas) for scattering by an infinite cylinder under oblique incidence," *Electromagnetics*, vol. 25, no. 1, pp. 39–54, 2005.

[31] N. Tsitsas, E. Alivizatos, D. Kaklamani, and H. Anastassiu, "Optimization of the method of auxiliary sources (mas) for oblique incidence scattering by an infinite dielectric cylinder," *Electrical Engineering*, vol. 89, no. 5, pp. 353–361, 2007.

[32] N. J. Higham, *Accuracy and stability of numerical algorithms*. SIAM, 2002.

[33] J. Davies, "Review of methods for numerical solution of the hollow-waveguide problem," in *Proceedings of the Institution of Electrical Engineers*, IET, vol. 119, 1972, pp. 33–37.

[34] F. L. Ng, "Tabulation of methods for the numerical solution of the hollow waveguide problem (short papers)," *IEEE Transactions on Microwave Theory and Techniques*, vol. 22, no. 3, pp. 322–329, 1974.

[35] B. A. Rahman, F. A. Fernandez, and J. B. Davies, "Review of finite element methods for microwave and optical waveguides," *Proceedings of the IEEE*, vol. 79, no. 10, pp. 1442–1448, 1991.

[36] J.-M. Guan and C.-C. Su, "Analysis of metallic waveguides with rectangular boundaries by using the finite-difference method and the simultaneous iteration with the chebyshev acceleration," *IEEE transactions on microwave theory and techniques*, vol. 43, no. 2, pp. 374–382, 1995.

[37] J. R. Kuttler, "A new method for calculating te and tm cutoff frequencies of uniform waveguides with lunar or eccentric annular cross section," *IEEE transactions on microwave theory and techniques*, vol. 32, no. 4, pp. 348–354, 1984.

[38] B. E. Spielman and R. F. Harrington, "Waveguides of arbitrary cross section by solution of a nonlinear integral eigenvalue equation," *IEEE Transactions on Microwave Theory and Techniques*, vol. 20, no. 9, pp. 578–585, 1972.

[39] M. Swaminathan, E. Arvas, T. K. Sarkar, and A. R. Djordjevic, "Computation of cutoff wavenumbers of te and tm modes in waveguides of arbitrary cross sections using a surface integral formulation," *IEEE transactions on microwave theory and techniques*, vol. 38, no. 2, pp. 154–159, 1990.

[40] S.-L. Lin, L.-W. Li, T.-S. Yeo, and M.-S. Leong, "Analysis of metallic waveguides of a large class of cross sections using polynomial approximation and superquadric functions," *IEEE Transactions on Microwave Theory and Techniques*, vol. 49, no. 6, pp. 1136–1139, 2001.

[41] P.-L. Jiang, S.-Q. Li, and C. H. Chan, "Analysis of elliptical waveguides by a meshless collocation method with the wendland radial basis functions," *Microwave and Optical Technology Letters*, vol. 32, no. 2, pp. 162–165, 2002.

[42] V. Lombardi, M. Bozzi, and L. Perregrini, "A novel variational meshless method with radial basis functions for waveguide eigenvalue problems," *IEEE Transactions on Microwave Theory and Techniques*, vol. 66, no. 8, pp. 3714–3723, 2018.

[43] T. Bernabeu-Jiménez, A. Valero-Nogueira, F. Vico-Bondia, and A. A. Kishk, "A comparison between natural resonances and characteristic mode resonances of an infinite circular cylinder," *IEEE Transactions on Antennas and Propagation*, vol. 65, no. 5, pp. 2759–2763, 2017.

[44] J. Lappalainen, P. Ylä-Oijala, D. C. Tzarouchis, and A. Sihvola, "Resonances of characteristic modes for perfectly conducting objects," *IEEE Transactions on Antennas and Propagation*, vol. 65, no. 10, pp. 5332–5339, 2017.

[45] W. Li, W. Chen, and G. Pang, "Singular boundary method for acoustic eigenanalysis," *Computers & Mathematics with Applications*, vol. 72, no. 3, pp. 663–674, 2016.

[46] P. Amore and D. Chowell, "Collocation approach to the helmholtz eigenvalue problem on multiply connected domains," *Journal of sound and vibration*, vol. 329, no. 9, pp. 1362–1375, 2010.

[47] A. Hochman and Y. Leviatan, "Efficient and spurious-free integral-equation-based optical waveguide mode solver," *Optics express*, vol. 15, no. 22, pp. 14 431–14 453, 2007.

[48] E. G. Alivizatos, I. D. Chremmos, N. L. Tsitsas, and N. K. Uzunoglu, "Green's-function method for the analysis of propagation in holey fibers," *JOSA A*, vol. 21, no. 5, pp. 847–857, 2004.

[49] S. Y. Reutskiy, "The method of fundamental solutions for helmholtz eigenvalue problems in simply and multiply connected domains," *Engineering Analysis with Boundary Elements*, vol. 30, no. 3, pp. 150–159, 2006.

[50] ——, "The methods of external and internal excitation for problems of free vibrations of non-homogeneous membranes," *Engineering Analysis with Boundary Elements*, vol. 31, no. 11, pp. 906–918, 2007.

[51] S. Reutskiy, "The methods of external excitation for analysis of arbitrarily-shaped hollow conducting waveguides," *Progress In Electromagnetics Research*, vol. 82, pp. 203–226, 2008.

[52] C.-M. Fan, D.-L. Young, and C.-L. Chiu, "Method of fundamental solutions with external source for the eigenfrequencies of waveguides," *Journal of Marine Science and Technology*, vol. 17, no. 3, pp. 164–172, 2009.

[53] T. F. Eibert, Y. Weitsch, H. Chen, and M. E. Gruber, "Solving periodic eigenproblems by solving corresponding excitation problems in the domain of the eigenvalue," *Progress In Electromagnetics Research*, vol. 126, pp. 65–84, 2012.

[54] P.-R. Renaud and J.-J. Laurin, "Shielding and scattering analysis of lossy cylindrical shells using an extended multifilament current approach," *IEEE transactions on electromagnetic compatibility*, vol. 41, no. 4, pp. 320–334, 1999.

[55] K. Wang, J.-J. Laurin, and K. Wu, "Scattering and shielding analyses of carbon fiber composites-based cylindrical shells using a multifilament doublet current method," *IEEE Transactions on Electromagnetic Compatibility*, vol. 61, no. 4, pp. 1015–1024, 2018.

[56] G. Fikioris, O. N. Bakas, and G. P. Zouros, "Study of convergence, divergence, and oscillations in method-of-auxiliary-sources (mas) and extended-integral-equation (eie) solutions to a simple cavity problem," *IEEE transactions on microwave theory and techniques*, vol. 61, no. 8, pp. 2773–2782, 2013.

[57] S. Huang, J. Pan, and Y. Luo, "Study on the relationships between eigenmodes, natural modes, and characteristic modes of perfectly electric conducting bodies," *International Journal of Antennas and Propagation*, vol. 2018, 2018.

[58] C. A. Balanis, *Advanced engineering electromagnetics*. John Wiley & Sons, 2012.

[59] C. R. Pollock, *Fundamentals of optoelectronics*. Irwin, 1995.

[60] E. Snitzer, "Cylindrical dielectric waveguide modes," *JOSA*, vol. 51, no. 5, pp. 491–498, 1961.

[61] A. W. Snyder, "Asymptotic expressions for eigenfunctions and eigenvalues of a dielectric or optical waveguide," *IEEE Transactions on microwave theory and techniques*, vol. 17, no. 12, pp. 1130–1138, 1969.

[62] C. Yeh, "Guided-wave modes in cylindrical optical fibers," *IEEE Transactions on Education*, no. 1, pp. 43–51, 1987.

[63] C. Yeh, "Elliptical dielectric waveguides," *Journal of Applied Physics*, vol. 33, no. 11, pp. 3235–3243, 1962.

[64] ——, "Modes in weakly guiding elliptical optical fibres," *Optical and Quantum Electronics*, vol. 8, no. 1, pp. 43–47, 1976.

[65] G. P. Zouros and J. A. Roumeliotis, "Exact and closed-form cutoff wavenumbers of elliptical dielectric waveguides," *IEEE transactions on microwave theory and techniques*, vol. 60, no. 9, pp. 2741–2751, 2012.

[66] S. M. Saad, "Review of numerical methods for the analysis of arbitrarily-shaped microwave and optical dielectric waveguides," *IEEE Transactions on Microwave Theory and Techniques*, vol. 33, no. 10, pp. 894–899, 1985.

[67] K. Chiang, "Review of numerical and approximate methods for the modal analysis of general optical dielectric waveguides," *Optical and Quantum Electronics*, vol. 26, no. 3, S113–S134, 1994.

[68] B. A. Rahman and J. B. Davies, "Finite-element analysis of optical and microwave waveguide problems," *IEEE Transactions on Microwave Theory and Techniques*, vol. 32, no. 1, pp. 20–28, 1984.

[69] M. Koshiba, K. Hayata, and M. Suzuki, "Improved finite-element formulation in terms of the magnetic field vector for dielectric waveguides," *IEEE transactions on microwave theory and techniques*, vol. 33, no. 3, pp. 227–233, 1985.

[70] J.-F. Lee, D.-K. Sun, and Z. J. Cendes, "Full-wave analysis of dielectric waveguides using tangential vector finite elements," *IEEE Transactions on Microwave Theory and Techniques*, vol. 39, no. 8, pp. 1262–1271, 1991.

[71] J.-F. Lee, "Finite element analysis of lossy dielectric waveguides," *IEEE Transactions on Microwave Theory and Techniques*, vol. 42, no. 6, pp. 1025–1031, 1994.

[72] K. Bierwirth, N. Schulz, and F. Arndt, "Finite-difference analysis of rectangular dielectric waveguide structures," *IEEE Transactions on Microwave Theory and Techniques*, vol. 34, no. 11, pp. 1104–1114, 1986.

[73] S. Patrick and K. Webb, "A variational vector finite difference analysis for dielectric waveguides," *IEEE transactions on microwave theory and techniques*, vol. 40, no. 4, pp. 692–698, 1992.

[74] P. Lusse, P. Stuwe, J. Schule, and H.-G. Unger, "Analysis of vectorial mode fields in optical waveguides by a new finite difference method," *Journal of Lightwave Technology*, vol. 12, no. 3, pp. 487–494, 1994.

[75] A. B. Fallahkhair, K. S. Li, and T. E. Murphy, "Vector finite difference modesolver for anisotropic dielectric waveguides," *Journal of lightwave technology*, vol. 26, no. 11, pp. 1423–1431, 2008.

[76] L. Eyges, P. Gianino, and P. Wintersteiner, "Modes of dielectric waveguides of arbitrary cross sectional shape," *JOSA*, vol. 69, no. 9, pp. 1226–1235, 1979.

[77] C.-C. Su, "A surface integral equations method for homogeneous optical fibers and coupled image lines of arbitrary cross sections," *IEEE transactions on microwave theory and techniques*, vol. 33, no. 11, pp. 1114–1119, 1985.

[78] N. Kishi and T. Okoshi, "Vectorial wave analysis of uniform-core optical fibers using a novel boundary integral method," *IEEE transactions on microwave theory and techniques*, vol. 37, no. 3, pp. 526–533, 1989.

[79] J. Charles, H. Baudrand, and D. Bajon, "A full-wave analysis of an arbitrarily shaped dielectric waveguide using green's scalar identity," *IEEE transactions on microwave theory and techniques*, vol. 39, no. 6, pp. 1029–1034, 1991.

[80] H. Cory, Z. Altman, and Y. Leviatan, "Determination of a dielectric waveguide propagation constant using a multifilament-current model," *Optics letters*, vol. 14, no. 18, pp. 1026–1028, 1989.

[81] A. Hochman and Y. Leviatan, "Analysis of strictly bound modes in photonic crystal fibers by use of a source-model technique," *JOSA A*, vol. 21, no. 6, pp. 1073–1081, 2004.

[82] W. Chew, *Waves and fields in inhomogeneous media*. Springer, 1990.

[83] A. Kapoor and G. Singh, "Mode classification in cylindrical dielectric waveguides," *Journal of lightwave technology*, vol. 18, no. 6, pp. 849–852, 2000.

[84] M. Kaur, S. Kakar, and D. Mandal, "Electromagnetic interference," in *2011 3rd International Conference on Electronics Computer Technology*, IEEE, vol. 4, 2011, pp. 1–5.

[85] E. R. Adair and R. C. Petersen, "Biological effects of radiofrequency/microwave radiation," *IEEE Transactions on Microwave Theory and Techniques*, vol. 50, no. 3, pp. 953–962, 2002.

[86] W.-J. Zhi, L.-F. Wang, and X.-J. Hu, "Recent advances in the effects of microwave radiation on brains," *Military Medical Research*, vol. 4, no. 1, pp. 1–14, 2017.

[87] R. Pandey, S. Tekumalla, and M. Gupta, "Emi shielding of metals, alloys, and composites," in *Materials for Potential EMI Shielding Applications*, Elsevier, 2020, pp. 341–355.

[88] H. Chen, W. Ma, Z. Huang, Y. Zhang, Y. Huang, and Y. Chen, "Graphene-based materials toward microwave and terahertz absorbing stealth technologies," *Advanced Optical Materials*, vol. 7, no. 8, p. 1 801 318, 2019.

[89] S. Bae *et al.*, "Roll-to-roll production of 30-inch graphene films for transparent electrodes," *Nature nanotechnology*, vol. 5, no. 8, pp. 574–578, 2010.

[90] M. Coroş, F. Pogăcean, L. Măgeruşan, C. Socaci, and S. Pruneanu, "A brief overview on synthesis and applications of graphene and graphene-based nanomaterials," *Frontiers of Materials Science*, vol. 13, no. 1, pp. 23–32, 2019.

[91] W.-S. Zhao, D.-W. Wang, A. G. D'aloia, W. Chen, G. Wang, and W.-Y. Yin, "Recent progress of nano-electromagnetic compatibility (nano-emc) in the emerging carbon nanoelectronics," *IEEE Electromagnetic Compatibility Magazine*, vol. 7, no. 2, pp. 71–81, 2018.

[92] S. K. Hong *et al.*, "Electromagnetic interference shielding effectiveness of monolayer graphene," *Nanotechnology*, vol. 23, no. 45, p. 455 704, 2012.

[93] J. Liang *et al.*, "Electromagnetic interference shielding of graphene/epoxy composites," *Carbon*, vol. 47, no. 3, pp. 922–925, 2009.

[94] D.-X. Yan, P.-G. Ren, H. Pang, Q. Fu, M.-B. Yang, and Z.-M. Li, "Efficient electromagnetic interference shielding of lightweight graphene/polystyrene composite," *J. Mater. Chem.*, vol. 22, pp. 18 772–18 774, 36 2012. DOI: 10.1039/C2JM32692B. [Online]. Available: http://dx.doi.org/10.1039/C2JM32692B.

[95] Y.-J. Wan, P.-L. Zhu, S.-H. Yu, R. Sun, C.-P. Wong, and W.-H. Liao, "Graphene paper for exceptional emi shielding performance using large-sized graphene oxide sheets and doping strategy," *Carbon*, vol. 122, pp. 74–81, 2017.

[96] A. Joshi, A. Bajaj, R. Singh, P. Alegaonkar, K. Balasubramanian, and S. Datar, "Graphene nanoribbon–pva composite as emi shielding material in the x band," *Nanotechnology*, vol. 24, no. 45, p. 455 705, 2013.

[97] K. Niu, P. Li, Z. Huang, L. J. Jiang, and H. Bagci, "Numerical methods for electromagnetic modeling of graphene: A review," *IEEE Journal on Multiscale and Multiphysics Computational Techniques*, vol. 5, pp. 44–58, 2020.

[98] J. Chen, J. Guo, and C. Tian, "Analyzing the shielding effectiveness of a graphene-coated shielding sheet by using the hie-fdtd method," *IEEE transactions on electromagnetic compatibility*, vol. 60, no. 2, pp. 362–367, 2017.

[99] V. Nayyeri, M. Soleimani, and O. M. Ramahi, "Modeling graphene in the finite-difference time-domain method using a surface boundary condition," *IEEE transactions on antennas and propagation*, vol. 61, no. 8, pp. 4176–4182, 2013.

[100] N. Liu, G. Cai, L. Ye, and Q. H. Liu, "The efficient mixed fem with the impedance transmission boundary condition for graphene plasmonic waveguides," *Journal of Lightwave Technology*, vol. 34, no. 23, pp. 5363–5370, 2016.

[101] M. Feliziani, S. Cruciani, and F. Maradei, "Circuit-oriented fem modeling of finite extension graphene sheet by impedance network boundary conditions (inbcs)," *IEEE Transactions on Terahertz Science and Technology*, vol. 4, no. 6, pp. 734–740, 2014.

[102] O. V. Shapoval, J. S. Gomez-Diaz, J. Perruisseau-Carrier, J. R. Mosig, and A. I. Nosich, "Integral equation analysis of plane wave scattering by coplanar graphene-strip gratings in the thz range," *IEEE Transactions on Terahertz Science and Technology*, vol. 3, no. 5, pp. 666–674, 2013.

[103] G. Lovat, "Equivalent circuit for electromagnetic interaction and transmission through graphene sheets," *IEEE Transactions on Electromagnetic Compatibility*, vol. 54, no. 1, pp. 101–109, 2011.

[104] G. Lovat, P. Burghignoli, and R. Araneo, "Low-frequency dominant-mode propagation in spatially dispersive graphene nanowaveguides," *IEEE transactions on electromagnetic compatibility*, vol. 55, no. 2, pp. 328–333, 2012.

[105] G. W. Hanson, "Dyadic green's functions for an anisotropic, non-local model of biased graphene," *IEEE Transactions on antennas and propagation*, vol. 56, no. 3, pp. 747–757, 2008.

[106] R. J. Paknys, "The near field of a wire grid model," *IEEE transactions on antennas and propagation*, vol. 39, no. 7, pp. 994–999, 1991.

[107] A. Nishikata and S. Kiener, "Shielding effectiveness of non-perfect conducting enclosures: Characterization of walls and numerical applications," in *Proc. 10th Int. Zurich Symp. EMC*, 1993, pp. 617–622.

[108] A. Nishikata and S. Kiener, "Modeling and analysis of the electromagnetic shielding behavior of superconductors, conductors and magnetic materials," *IEEE transactions on magnetics*, vol. 30, no. 5, pp. 3359–3362, 1994.

[109] P. Li, C. Chen, J. Zhang, S. Li, B. Sun, and Q. Bao, "Graphene-based transparent electrodes for hybrid solar cells," *Frontiers in materials*, vol. 1, p. 26, 2014.

[110] K. Choi and H. G. Park, "Smart reinvention of the contact lens with graphene," *ACS nano*, vol. 11, no. 6, pp. 5223–5226, 2017.

[111] K. S. Novoselov *et al.*, "Electric field effect in atomically thin carbon films," *science*, vol. 306, no. 5696, pp. 666–669, 2004.

[112] A. K. Geim and K. S. Novoselov, "The rise of graphene," in *Nanoscience and technology: a collection of reviews from nature journals*, World Scientific, 2010, pp. 11–19.

[113] L. Falkovsky, "Optical properties of graphene," in *Journal of Physics: conference series*, IOP Publishing, vol. 129, 2008, p. 012 004.

[114] S. M. Raeis-Zadeh and S. Safavi-Naeini, "Analysis of electromagnetic wave scattering by graphene flakes using the generalized multipole technique," *IEEE Transactions on Antennas and Propagation*, vol. 64, no. 3, pp. 1032–1038, 2016.

[115] M. Naserpour, C. J. Zapata-Rodrıguez, S. M. Vuković, H. Pashaeiadl, and M. R. Belić, "Tunable invisibility cloaking by using isolated graphene-coated nanowires and dimers," *Scientific reports*, vol. 7, no. 1, pp. 1–14, 2017.

[116] W. Liu and Y. Xu, *Spintronic 2D materials: fundamentals and applications*. Woodhead Publishing, 2019.

[117] A. Vakil, *Transformation optics using graphene: One-atom-thick optical devices based on graphene*. University of Pennsylvania, 2012.

[118] T. Christensen, A.-P. Jauho, M. Wubs, and N. A. Mortensen, "Localized plasmons in graphene-coated nanospheres," *Physical Review B*, vol. 91, no. 12, p. 125 414, 2015.

[119] A. J. Pollard and C. A. Clifford, "Terminology: The first step towards international standardisation of graphene and related 2d materials," *Journal of Materials Science*, vol. 52, no. 24, pp. 13 685–13 688, 2017.

[120] I.-T. Lin, *Optical properties of graphene from the THz to the visible spectral region*. University of California, Los Angeles, 2012.

[121] I.-T. Lin *et al.*, "Terahertz optical properties of multilayer graphene: Experimental observation of strong dependence on stacking arrangements and misorientation angles," *Physical Review B*, vol. 86, no. 23, p. 235 446, 2012.

[122] I.-T. Lin and J.-M. Liu, "Terahertz frequency-dependent carrier scattering rate and mobility of monolayer and aa-stacked multilayer graphene," *IEEE Journal of Selected Topics in Quantum Electronics*, vol. 20, no. 1, pp. 122–129, 2013.

[123] N. Tsitsas, E. Alivizatos, H. Anastassiu, and D. Kaklamani, "Accuracy analysis of the method of auxiliary sources (mas) for scattering from a two-layer dielectric circular cylinder," in *2005 IEEE Antennas and Propagation Society International Symposium*, IEEE, vol. 3, 2005, pp. 356–359.

[124] N. Feng *et al.*, "Near-unity anisotropic infrared absorption in monolayer black phosphorus with/without subwavelength patterning design," *IEEE Journal of Selected Topics in Quantum Electronics*, vol. 25, no. 3, pp. 1–7, 2018.

[125] J. Zhu, S. Yan, N. Feng, L. Ye, J.-Y. Ou, and Q. H. Liu, "Near unity ultraviolet absorption in graphene without patterning," *Applied Physics Letters*, vol. 112, no. 15, p. 153 106, 2018.

[126] X.-S. Li, N. Feng, and Y. Zhang, "Well-organized mzt-me-pml approach for thz bp metasurface implementations," *Commun. Comput. Phys.*, vol. 29, no. 2, pp. 588–605, 2021.